CRANFIELD UNIVERSITY

DENNY LESMANA

An investigation into the effect of the gilding jacket on 12.7 mm armour-piercing projectile penetration of armour materials

CRANFIELD DEFENCE AND SECURITY
Master by Research

MSc
Academic Year: 2017 - 2018

Supervisors: Prof Amer Hameed and Dr Gareth Applebly-Thomas
March 2018

CRANFIELD UNIVERSITY

Cranfield Defence and Security
Master by Research

MSc

Academic Year 2017 - 2018

DENNY LESMANA

An investigation into the effect of the gilding jacket on 12.7 mm armour-piercing projectile penetration of armour materials

Supervisors: Prof Amer Hameed and Dr Gareth Applebly-Thomas
March 2018

This thesis is submitted in partial fulfilment of the requirements for the degree of MSc

ABSTRACT

The influence of both the bullet jacket and projectile core hardness for 12.7-mm armour piercing (AP) rounds has been investigated using a variety of different experiments with the aim of optimising projectile performance. The research was designed to elucidate the role of these two elements in the penetration process, building on work elsewhere in the literature. A combination of forwards and reverse (target impacting stationary projectile) investigations provided insight into both penetration efficiency and resultant target failure modes. The results of these experiments, backed by a pressure-gauge based impact technique, were validated via numerical modelling.

It was observed that the jacket appears to serve three inter-linked functions: pre-damage of the target; cushioning of the AP core and confinement of the core. Modifying the core hardness showed that penetration efficiency was maximised when this hardness was greater than / overmatched that of the target (Armox Advance) plate. This behaviour was more pronounced when a thicker (9 rather than 5-mm thick) target plate was employed, suggesting that projectile / target interaction time was of particular importance (a potential confinement effect). However, for the 9-mm target plates where overmatch did not occur, reduced penetration / a 'ceramic-like' response was observed. In a similar manner, the presence of a jacket had the greatest effect for thicker plates. However, this confinement effect was complemented by pressure gauge results which suggested that the presence of the jacket enhanced energy coupling into the target (and, in corollary, that the jacket prevented premature and excessive loading of the core). In turn, numerical simulations provided further evidence that the jacket appeared to be protecting (cushioning) the core on impact. However, these also highlighted the extent of pre-damage caused by the jacket.

Keywords:

Forward ballistic, reverse ballistic, 12.7 mm armour piercing, gas guns, copper jacket, Armox Advance, pressure gauge experiment, numerical simulation.

ACKNOWLEDGEMENTS

Firstly, I would like to take opportunity to thank my supervisors, Professor Amer Hameed and Dr Gareth Appleby-Thomas for the continuous support of my MSc study and related research, for their patience, motivation, and immense knowledge. Their guidance helped me through all the stages of research and writing of this thesis. I could not have imagined having better advisor and mentors for my MSc. I would also like to offer my special thanks to Andrew Roberts and David Wood for help in supporting the ballistic testing in the Dynamic Response / Survivability of Advanced Materials Group at Cranfield University's Shrivenham Campus. I would also like to say thank you to Karl Norris and Adrian Mustey for help in preparing the projectiles and the targets employed as well as for undertaking material testing at the busiest time of year. Further, I would like to thank Dr Michael Gibson who was greatly knowledgeable, tolerant and supportive in the computational modelling. Advice and comments given by Henry Agu and Brianna Fitzmaurice as well as other staff / students in Building 18 have been a great help in finishing this study.

I would also like to express my gratitude to PT. Pindad (Persero) for their support in this MSc programme. I received generous support from Dr Ade Badgja and Dr Yayat Ruyat during my studies. I also thank my colleagues, Prima Kharisma IY; Yudistira Sanjiwani and other RnD staff in Turen, for the stimulating discussions and project preparation. We also acknowledge the Indonesia Endowment Fund for Education (LPDP) for funding the experiments and the MSc by Research programme within which they were undertaken.

Finally, I would like to thank my wife, Baiq Octaviana Dwi Anggraeny and my son Ahmad Athar Al-Fatih Guinandra who have accompanied me in running my simulations and thesis writing – many times – overnight supporting me with a fill of joy and delicious foods. I owe my deepest gratitude to my parents, Ir. Welly Sudiono, Endang Widati, Dr Lalu Mulyadi and Siti Nasfiyah, and my family in Malang and Makassar for their full support during my study.

TABLE OF CONTENTS

LIST OF FIGURES

LIST OF TABLES

LIST OF EQUATIONS

LIST OF ABBREVIATIONS

AA	Aluminium Alloy
AP	Armour Piercing
CFRP	Carbon Fibre Reinforced Polymer
DoP	Depth of Penetration
FFV	Forenade Fabriksverken (Ammunition Manufacturers)
GFRP	Glass Fibre Reinforced Plastic
HESH	High-Explosive Squash-Head
HRC	Hardness Rockwell C
HSS	High Speed Steel
HSV	High Speed Video
mm	Millimetres
μs	Microseconds
RHA	Rolled Homogenous Armour
PMMA	Polymethyl methacrylate
KE	Kinetic Energy

1 Introduction and literature review

PT. Pindad has developed 12.7 x 99 mm armour-piercing ammunition for anti-material sniper weapon. It has an arrow shape core to increase volume and diameter of the core to enhance projectile stability. However, direct contact of this projectile with hard target lead core to be eroded or shattered during the impact. To enhance the projectile's penetration performance, it is essential that the projectile's construction should be redesigned. Moreover, proper material analysis and selection will provide better understanding about material performance in impact response and penetration mechanism based on material characteristics.

1.1 Small arms ammunition

Ammunition comprises four main components; these are the cartridge case, projectile, propellant powder, and primer. The primer is a small component that contains an impact or electric-sensitive chemical powder mixture to initiate the explosive train. The primer generates a spark or heat or both which ignites propellant powder and as the propellant powder burns, it produces a high-pressure gas very quickly which accelerates the projectile down the gun barrel to a high velocity. After leaving barrel, the projectile travels through the air and impacts the target at an energy level which – if it is to be effective – must overmatch the target. Essentially, this energy level should be higher than the energy required to break the target.

1.1.1 Projectile types

There are several types of bullets used in both military and sporting activities; example of such ammunition are lead (ball), armour piercing, hollow point boat tail, and frangible rounds. The construction of the ammunition is dependent upon its designed effect (1).

The ball projectiles are simply projectiles constructed of a solid material that have been formed into particular shape and calibre. The ball projectiles may or may not be jacketed or coated with gilding materials (such as copper). This rounds is designed to defeat soft skins.

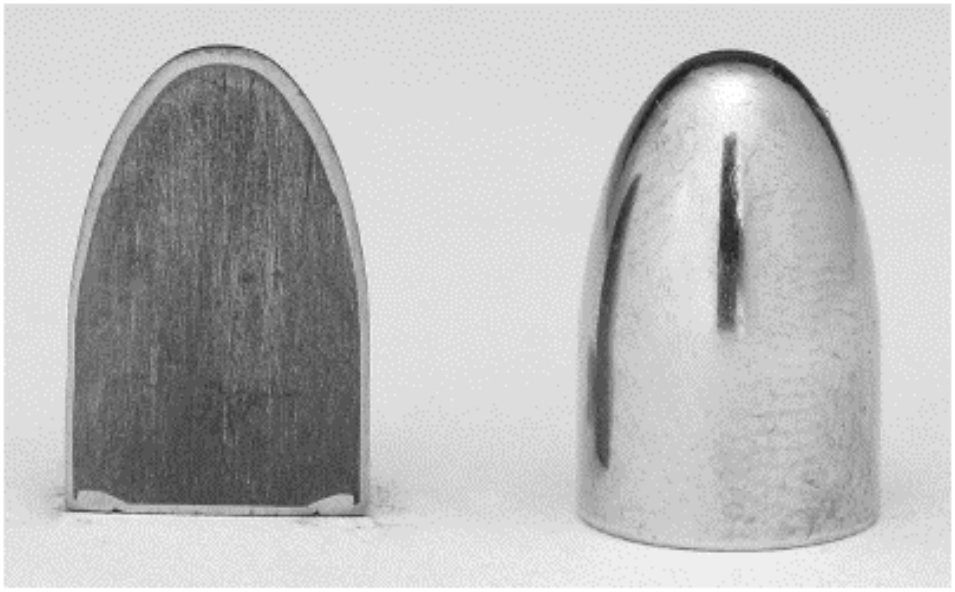

Figure 1.1 A 9-mm 115-grain copper-jacketed projectile (1).

Figure 1.1 shows a cross-sectional view of 9-mm jacketed projectile which comprises lead core and copper jacketed. The projectile performance may be affected by impact velocity, material characteristics, and the projectile shape. The ball ammunition is designed to be non-expansive in term of terminal ballistics.

In contrast with the ball projectiles which is designed to penetrate soft target, armour-piercing rounds are designed to overcome armour of a given specification. Hardened steels or high strength materials such as tungsten carbide and even depleted uranium have been or are currently used to construct armor-piercing projectiles. This projectile is designed to defeat well protected targets by piercing through armour protection and applying sufficient energy to damage the target behind.

Hollow point ammunitions receive their name from their typical characteristic that is a cavity in projectile nose. This special class of projectile is designed to expand from its original diameter to twice or even three times larger than the initial diameter. When the hollow point projectile expands, it increase the size of wound cavities in the target, thus increasing the incapacitating or the lethal potential of the projectile. Moreover, because the impact surface of the hollow point projectile has been increased, there is a greater surface area of projectile to fully transmit the kinetic energy from the projectile into the target. As a result, it will reduce the probability of over-penetration and stop the projectile within the target. This projectile are usually used by law enforcement officers, security staffs and hunters. Figure 1.2 below shows the hollow point ammunition appearance and the recovered projectiles after impacting the target which has a larger diameter compared to its original diameter.

Figure 1.2 Hollow point ammunitions and expanded projectiles (1).

Lastly, a frangible projectile is designed to shatter or disintegrate into debris or dust upon impacting targets. In general, the frangible projectiles are produced from a mixture of copper, bismuth, tin or tungsten. These projectiles are formed by pressing machine inside a typical mould and held together through a bonding agent such as epoxy, nylon or another matrix-type bonding additive. A sintering process is also applied to adhere the projectile. Frangible projectiles may or may not be protected by gilding jacket. Frangible projectiles have been known as an alternative to traditional lead-based projectile for training and anti-aircraft

ammunitions. Frangible ammunition has been widely introduced as the “green ammunition” as it use powder compounds devoid of the heavy elements, particularly lead.

Metallic and ceramic armours are the most common targets for small calibre armour piercing projectiles, as well as for medium and large calibre projectiles. As discussed by Carluccci and Jacobson (2), projectiles may impact metallic targets under a wide range of velocities. At very low velocities (<250 m/s), penetration is primarily affected by the dynamic behaviour of the target. While when the impact velocity is higher at between 500 and 2,000 m/s, they showed that the behaviour of the target and penetrator material are both important. With further increase in velocity (2,000–3,000 m/s), the high pressures provided upon impact were observed to allow material to behave like a fluid in the early stages of impact (hydrodynamic behaviour); while at impact velocities beyond 12,000 m/s, the colliding material vaporized.

1.1.2 Projectile penetration mechanism

Further observations were conducted by the authors to investigate material (both target and penetrator) property and shape effects on penetration mechanisms as well as to interrogate the effect of impact velocity. Figure 1.1 illustrates that penetrator impact with a target can result in numerous different types of material failure behaviour in differing impact (velocity) regimes. In particular, to give a feel for the extent and variable nature of such failure modes key ones touched on by these authors are described below (2-3):

a) Plugging arises in materials which are not very ductile and usually occurs when the projectile impact velocity is very close to the ballistic limit. It is common in materials susceptible to adiabatic shear (for example, Ti64) and also more common when an impactor has a blunt impact face.
b) Piercing (ductile hole formation) usually occurs in thick plate penetration. The plate are defeated by a radial displacement and followed by plastic flow and yielding of the target.

c) Petaling occurs when the projectile impact velocity is close to the ballistic limit and the resultant radial and circumferential stresses are high.

d) Scabbing is a failure mode with similar characteristics to that of spalling, but it is initiated by a crack at a material inhomogeneity point. Moreover, the crack continues to generate further damage within material. Essentially it is the limiting case of spallation – with dynamic tensile failure leading to material separation in the form of a scab at the rear-most surface of the targeted armour plate.

e) Spalling is caused by the shock waves generated on projectile impact being reflected back from an un-confined face (typically the rear-most face) of a target plate as tensile waves. It is common for materials to have a much higher compressive than tensile strength – hence the tendency to fail in tension.

f) Radial cracking (e.g. cracks radiating from the point of impact) is common for such armour materials – occurring, for example, in both ceramics and several steel armours.

g) Finally, brittle fracture is sudden and catastrophic and often occurs in either low density materials or those without sufficient toughness.

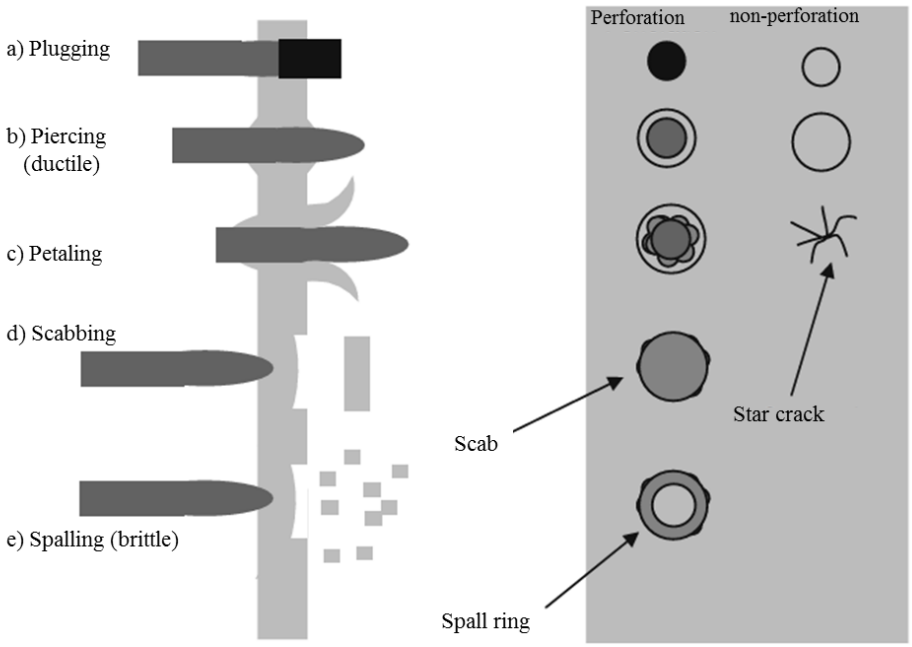

Figure 1.3 Target failure modes (2).

Numerous studies have been conducted to observe armour piercing projectile's impact against hard targets such as ceramics and high-strength steel. However, only a small number of experiments have been employed to study the effect of the bullet jacket on an armour piercing projectile's penetration with different hardness of projectile core. In a useful study in this area, Hazell et al. (4) examined the effect of a gilding jacket on 7.62 mm FFV armour piercing projectiles against Alumina and Silicon-carbide ceramics. It was observed that the presence of the jacket resulted in initial damage to the ceramic surface before core penetration. Hence, in the depth-of-penetration (DoP) tests employed, removing the jacket before firing the projectile was shown to result in a reduction in depth of penetration into the aluminium backing layer employed to assess ballistic efficiency. Further study was employed by Roberts (5) to examine the role of the 7.62 mm bullet jacket during penetration. In this study, it was clearly observed that the jacket played a key role in penetrating the target material. The bullet with jacket penetrated the target deeper than the modified (removed jacket) bullet. Essentially, jacket removal was shown to enhance ballistic efficiency.

In a similar study, 7.62 mm armour piercing ammunition impact on to high hardness armour steel was studied by Kilic and Ekici (6). Residual velocity measurement was used to validate (via simulation) results. The experiment employed two types of projectile; full bullet and a single core model. The full bullet model comprised of a steel core, lead-antimony cap and copper jacket, while the single core model was simulated as a steel core only projectile. These numerical simulations (Figure 1.2) showed that the higher the bullet speed, the deeper the resultant projectile penetration, and that a full bullet model led to a higher DoP than a single core (only) model. Moreover, thicker armour steel targets resulted in a decrease in DoP.

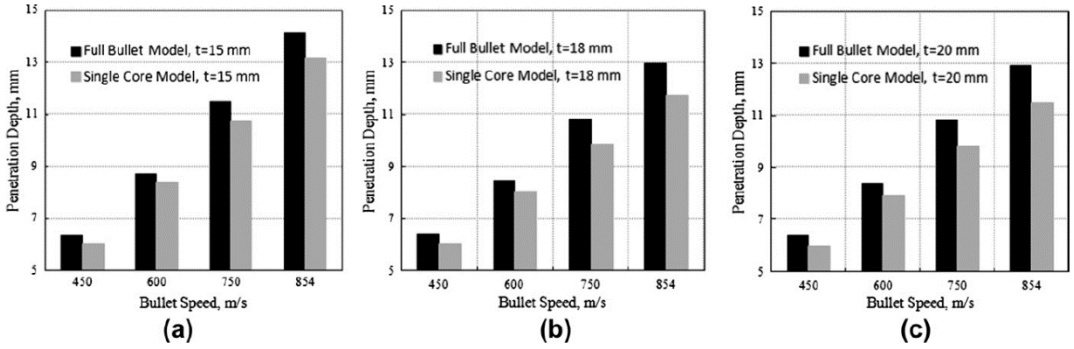

Figure 1.4 Full bullet and single core model's DoP for various steel target thicknesses: (a) 15mm, (b) 18mm, and (c) 20mm (6)**.**

Figure 1.3 shows a typical set of results from the simulations run by Kilic and Ekici (6)**.** In the first step (t=0.006 ms) the bullet's jacket indents the target and the lead-antimony filler is eroded because of its low hardness. The armour steel target continues to be damaged due to further interaction with the intact projectile core as penetration continues. It is this overmatch of the projectile core (e.g. its greater hardness / strength compared to the target) that allows the bullet to act as an 'armour piercing' round.

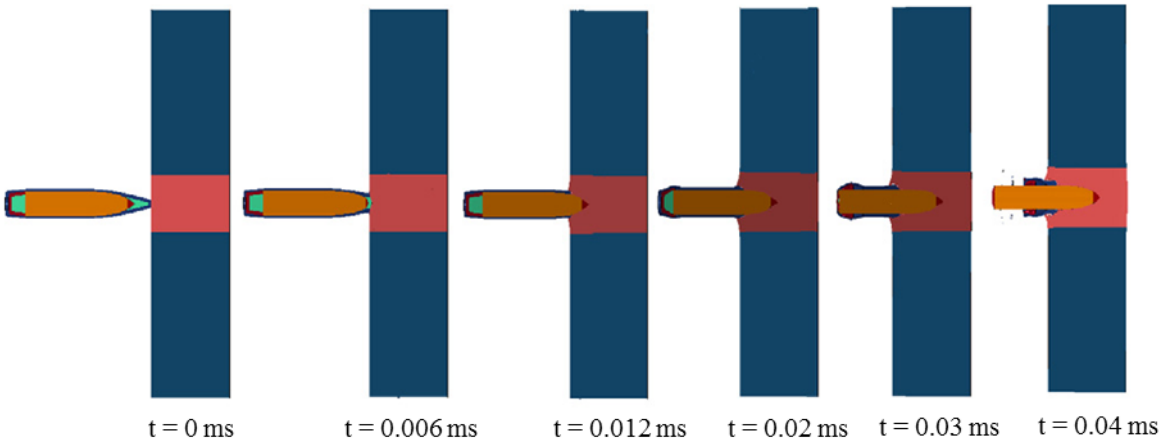

Figure 1.5 Projectile and target steel deformation at various time steps (18).

Further studies were employed to examine the ballistic performance of ultra-high hardness armour steel and boron carbide at various thicknesses under 7.62 mm and 12.7 mm AP projectile attack by measuring the ballistic limit V_{50} and DoP (7-8). These studies that both increasing hardness and thickness of plates reduced both the V_{50} and subsequent DoP – e.g. that they improved armour performance.

1.2 Armour systems

The middle of a war zone can be a very dangerous environment for military personnel. Significant threats include random explosions and high-velocity impact of projectiles or fragments from munitions – potentially with high explosive material. Because of these conditions, many countries have developed several armour materials which are applied to their military equipment. These materials have increased survivability of soldiers during military operations. Lightweight aluminium alloys, hardened steels, high strength steels, composite materials / systems and even polymeric materials are used in military vehicles, helicopters, aircrafts, body-armours, and buildings / structures. For example, by using proper materials – in appropriate combinations – helicopters are able to cope with small ammunition attack, while mobility vehicles can be protected from un-anticipated / random explosions coming from improvised explosive devices (IEDs), land mines or high explosive ammunition. Figure 1.4 shows an example of an armoured personnel carrier which is protected with hard armour plates (HPA).

Figure 1.6 An armoured personnel carrier, Anoa 6×6 Pindad, 2017 (9).

Armour design often needs to capture the performance of both hard (but potentially brittle) disrupters and tougher absorbers. To this end, multi-material (composite) solutions are often employed. It should be noted that the term ‘composite’ is largely used in this thesis to refer to materials such as CFRP. However, more generally, it can refer to any system with multiple interacting elements. As an example of a composite / complex solution, a complex design of a body armour system is shown in Figure 1.5. This comprises of polymer and composite materials that have a good capability to protect the human body from small fragments and high-velocity projectiles of small arm ammunitions, as well as harder outer layers (e.g. alumina / Al_2O_3).

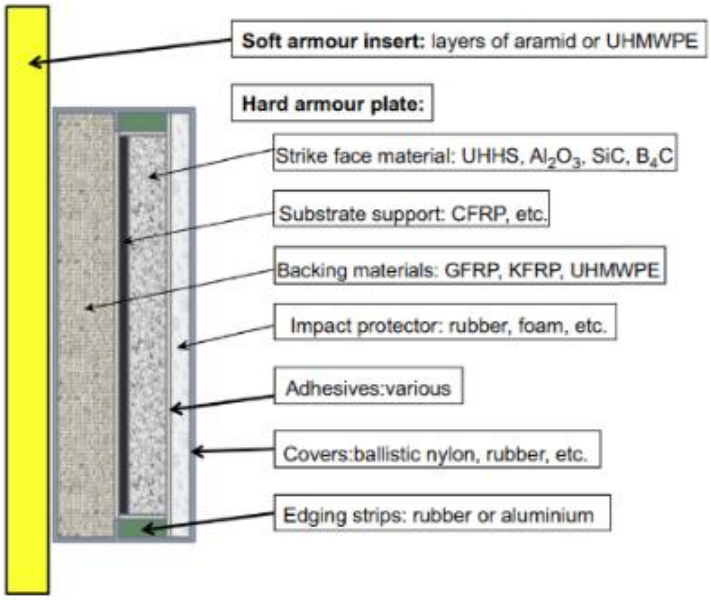

Figure 1.7 Cross-sectional view of a body armour system (10).

1.2.1 Armour classification

1.2.1.1 Metallic armour

Metals are the most commonly used materials in armour protection systems. The main reason for using metals in armour design is that they have a good capability in carrying heavy loads while providing an effective protection as well as being less expensive compared to other developed armour materials. This set of advantageous properties is linked to a variety of factors including secure / ready supply of raw materials, knowledge of processing routes, ability to tailor material properties (e.g. via heat treatments), ready availability of fixing / joining solutions, amongst others. Steel is the most commonly applied metallic material in armour systems. It has good material properties as required in protection system such as good toughness, fatigue and hardness as well as ease of production and joining.

The steels commonly employed in such applications consist of Fe-C alloys which can be developed to be various steels with a different properties. Heat treatment and cooling rates plays an important role in the steel microstructure formation

and the resultant mechanical properties. A different temperature during hardening and variation in subsequent cooling rate results in variation in steel properties. E.g. cooling a steel quickly (a quench) will have a different effect than cooling it slowly, although this depends on the carbon content. High hardness steels contain a high percentage of martensite – a strained body centred tetragonal structure. Martensite is the hardest constituent obtained in a given steel, and the hardness of this phase increases with carbon content. These steels are very hard but brittle, and following heat treatment (tempering) allows an improvement in ductility. There are several types of steels which are usually applied for armour protection system: low-carbon steels, high-strength low-alloy steels, quenched and tempered steels, high carbon steels, and high alloy steels (3). AS an example, Figure 1.6 shows the extent of steel armour application in the UK FV432 vehicle, along with details of other armour constituents. Various compositions and hardness's of steel are employed in different areas according to the required function / vulnerability of the area in question.

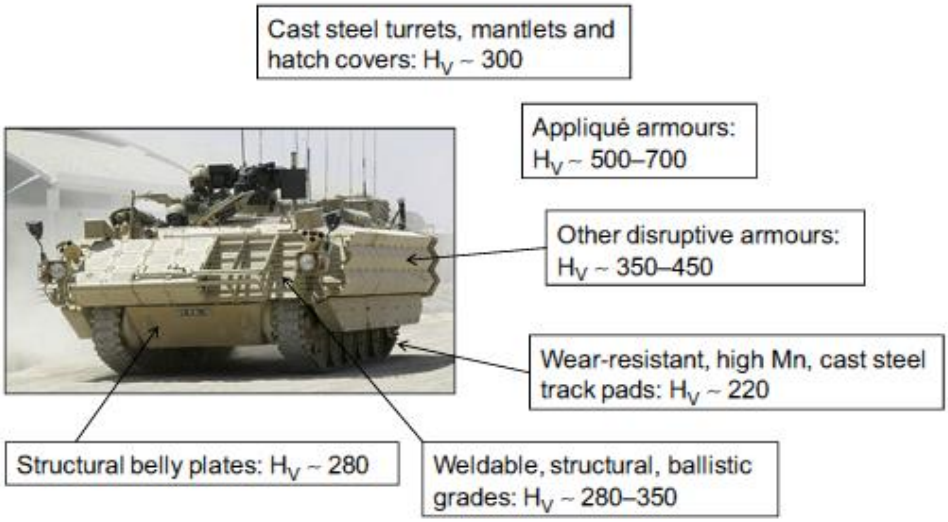

Figure 1.8 Application of armour steels in the UK FV432 armour vehicle with various hardness condition (Hv = Vickers Hardness) (10).

Usefully steel armour can be studied in four main groups, namely (3):

a. Rolled homogenous armour (RHA)

Rolled homogenous armour (RHA) has been developed and applied in most military vehicles. It is also used as a comparison of other armour systems, with a developed material's performance typically quoted in terms of RHA equivalents. RHA comprises of carbon (0.18–0.32%), manganese (0.60–1.50%), nickel (0.05-0.95%), chromium (0.00-0.90%), molybdenum (0.30-0.60%), sulphur (0.015% max) and phosphorous (0.015% max). It is produced by hot-rolling of steel ingots which have a small percentage of alloying elements followed by both a quenching and tempering process to allow martensitic microstructure formation. Table 1.1 provides further details of the different forms of RHA that are typically employed.

Table 1.1 Classification of RHA (11).

Classification	Description	Hardness (BHN)	UTS (MPa)	Elongation (%) Min
Class 1	Readily weld-able steel subjected to structural loads	262-311	895-1,050	15
Class 2	Readily weld-able steel to protect against AP Ammunition	255-341	895-955	14-16
Class 3	Readily weld-able higher hardness steel manufactured in thin sections	470-540	1,450-1,850	8
Class 3A	Readily weld-able higher hardness steel manufactured in thin sections	420-480	1,200-1,600	9
Class 4	Higher carbon and alloy content higher hardness armour for thick section	475-605	1,450-2,000	7
Class 5	High alloy content armour with very high hardness used for special applications such as perforated armour	560-655	1,800-2,400	6

b. High-hardness armour (HHA)

High-hardness armour (HHA) is a homogenous armour which has a hardness value over 430 BHN. This armour is manufactured by a similar method to that of RHA heat treatment but with a lower tempering temperature (~200^{o}C).

c. Variable hardness steel armour

Steel armour can be manufactured such that it possesses a dual or gradient hardness in a single plate. There are a number of advantages associated with applying a steel plate with varying strength properties as an armour material. In order to get a combination of a high strength front surface and a ductile layer behind, surface-hardening is applied to a low carbon steel. The ductile, tougher, backing layer is able to absorb more energy and reduce any crack propagation from the front layer failure. Carburising is one of the common face-hardening processes applied to produce such armour. As an example, dual hardness armour (DHA) can be manufactured effectively by roll-bonding of 601-712 BHN front plate to a 461-534 BHN back plate together (12). The ballistic performance of DHA outperforms RHA and HHA in terms of small arms ammunition attack.

d. Perforated armour

In such armour systems, perforated steel plates are manufactured to improve ballistic performance in many various configurations. The holes or slits in perforated plate armour are provided to interact with incident projectiles. When a bullet impacts a hole side of the perforated steel plate armor, it is diverted or damaged by bending stresses generated during the collision and this thus reduces its penetration capability before impacting the main armour (13). One study in this area by Fras et al. (14) observed the behaviour of projectile penetration on thin perforated steel plates (illustrated in Figure 1.7). These were shown to be useful as passive additional protection for armoured systems against small-calibre bullets.

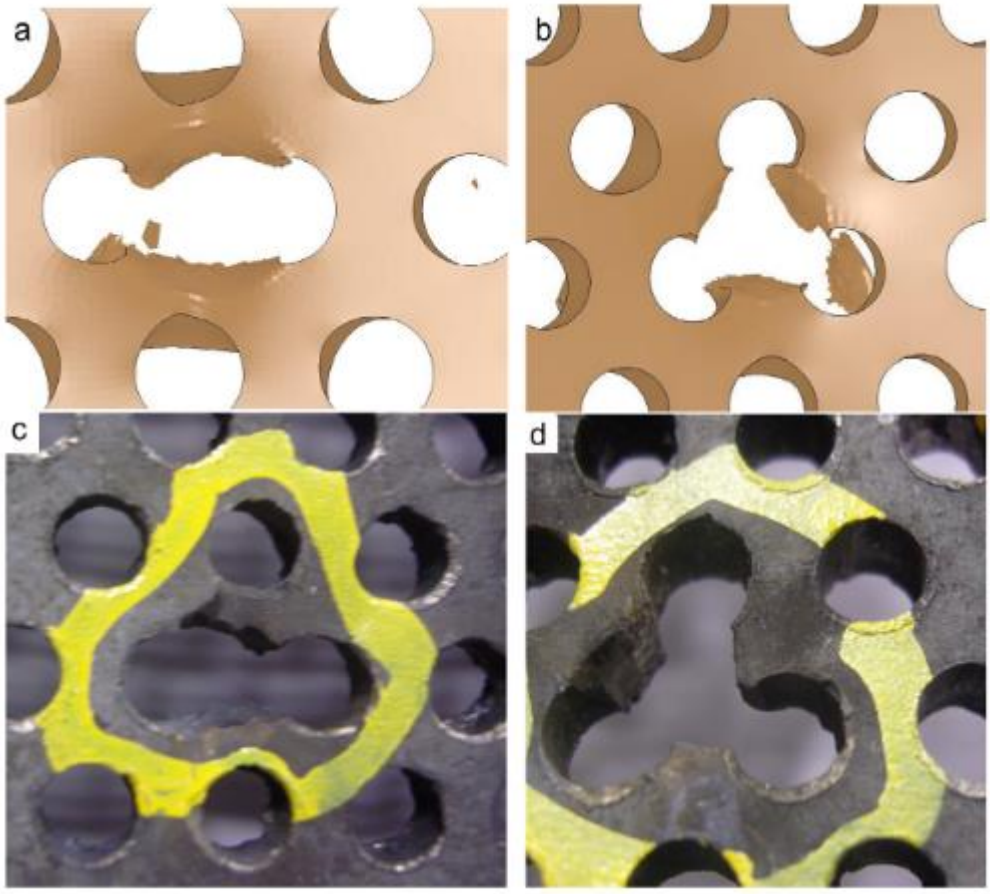

Figure 1.9 Numerical simulation (a) and (b), and experimental (c) and (d) results of perforated steel response after ballistic testing (14).

Other metallic materials such as aluminium, magnesium and titanium alloys have been developed to be applied in armour system application. For example, several studies have investigated aluminium alloy (AA) armour performance, including AA-2024, AA-6061, AA-7017 and AA-7075 armour against small-calibre ammunition (15-17). The potential advantages of aluminium alloys as armour materials are their low-density, the potential for mechanical properties improvements (for example with precipitation-hardenable alloys) and less susceptibility to stress corrosion cracking. By comparison, there have been only a relatively small number of magnesium and titanium alloy armour studies in recent decades. For example, Hazell and co-authors (18) have studied a spall and shock behaviour of an armour-grade wrought magnesium alloy (Elektron 675) under one-dimensional shock loading. Some titanium base armours also

have been assessed by ballistic test using both small and medium-calibre ammunitions (19-20). However, overall / as detailed, there is a relative paucity of data in the literature on these materials.

1.2.1.2 Ceramic armour

Ceramics are one of the most important materials in armour system development in recent years. They have been a very effective and applicable material in protection technology, because they are very good disruptor materials compared to metallic and composite armours (primarily due to their very high compressive strengths). As an example of a ceramic-based application, Figure 1.10 illustrates a lightweight ceramic composite armour solution. This comprises of a ceramic front layer combined with a ductile backing layer. The ceramic's function is to erode and damage an incoming bullet, whereas the backing plate delays the tensile fracture of the ceramic and absorbs some of kinetic energy of the (disrupted) projectile by deformation (10).

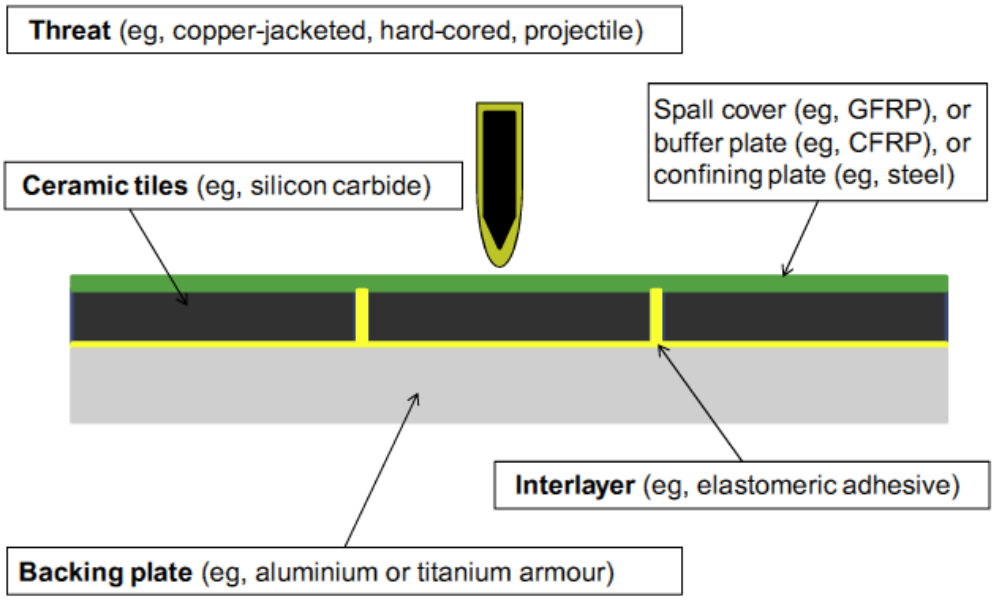

Figure 1.10 Schematic arrangement of ceramic composite armour (10).

Several research activities have centred on ceramic armour performance testing against small and medium calibre ammunitions (21-24). For example, Horsfall

and colleagues have tested various types of 7.62 mm armour piercing ammunition against ceramic faced composite (alumina-aramid) by measuring ballistic limit velocity (21). While Petterson et al. (22) have studied titanium-titanium diboride composites as part of a gradient armour material, which comprises several materials in different hardness. More recently, development of ceramic base armour has been focused on highlighting the failure mechanisms of ceramic during ballistic attack with different projectile configurations. In particular, focus has been on alumina and boron carbide tiles which are already widely employed as body-armour for personnel protection (23-24).

1.2.1.3 Fabric and composite armours

Fabric and composite materials possess high specific strength and stiffness as well as being able to absorb some of the kinetic energy of impacting projectiles via deformation (e.g. due to their – typically – woven structure with fibres propagating energy away from the point of impact). These materials also have relatively low densities (e.g. compared to metallic materials). Moreover, some of the woven fabric systems have a high tensile strength (~2-3 GPa) and reasonable strains to failure (~3-6%) (3).

Table 1.2 shows mechanical properties of some fibres with military equipment applications.

Table 1.2 Mechanical properties of some fibres in military environment (3)

Fibre	Density (kg/m^3)	Tensile Strength (MPa)	Specific Strength (m^2/s^2)	Elastic Modulus (GPa)	Specific Stiffness (m^2/s^2)	Failure Strain (%)
Aramid (low modulus)	1440	2900	2.01×10^6	60	4.17×10^7	3.6
Aramid (high modulus)	1450	2900	2.00×10^6	120	8.28×10^7	1.9
Polyethylene (low modulus)	970	2700	2.78×10^6	89	9.18×10^7	3.5
Polyethylene (high modulus)	970	3200	3.30×10^6	99	1.02×10^8	3.7
E-glass	2600	3500	1.35×10^6	72	2.77×10^7	4.8
S-glass	2500	4600	1.84×10^6	86	3.44×10^7	5.2
Carbon (high strength)	1780	3400	1.91×10^6	240	1.35×10^8	1.4
Carbon (high modulus)	1850	2300	1.24×10^6	390	2.11×10^8	0.5

Most of the fibres detailed above are used as elements of the backing layers in composite laminate armour. High failure strain fibres (apart from carbon fibres) are applied in blast or ballistic protective solutions. Whereas carbon-based fibres are very brittle materials so they are usually manufactured to give additional stiffness to armour systems, preventing them from bending during loading (3). In recent studies, both failure mode and fibre backing layer performance have been discussed to compare some of the different fibres available and other composite

materials used in ceramic or high hardness steel-based armour reinforcement (25-28).

1.2.2 Armour configurations

Armour systems can be classified in two main groups based on how their protection mechanism operates. These groups are passive and reactive armour (3, 10, 29).

1.2.2.1 Passive armours

Passive armours have a capability to absorb kinetic energy from incoming projectiles or shaped charge jets during impact. Some passive armours are designed with different geometrical designs and high strength armour plates to achieve a good performance against incoming threats. Deniz (29) has listed the passive armour types as follows:

a. Sloped armours

In this armour configuration, armours are installed obliquely rather than in a vertical position. Such oblique armour can deflect the projectile (ricochet).

b. Spaced armours

Spaced armours are usually applied to defeat shaped charge jets by providing a distance which results in the jets particulation, thus reducing their penetration capability. In RPG attack, recommended space distance is around 300 mm. These armours are also effective against HESH ammunition (with the resultant scab forming in the outer layer / being unable to penetrate the inner layer). Moreover, these armours can be used to tumble and deflect projectiles.

c. Slat armours

These systems protect main armour plates by catching RPG shaped charge ammunition and preventing initiation via shorting of the fusing system. A typical configuration is shown in Figure 1.11.

Figure 1.11 Slat armours installed to protect main armour plates (30).

d. Composite / layered armours

These armours comprise steels, ceramics, fabrics and other composite materials layers to give an effective protection from a multitude of threats.

1.2.2.2 Reactive armours

Reactive armours are manufactured by using elements that are sandwiched between two (typically) steel plates. The reaction of these armours to ballistic attacks depends on the elements characteristics. These armours can be classified as explosive reactive armour (ERA), bulging armour (Non-ERA) and electric armour (3) (while other systems such as active armours exist, such as Israel's Rafael Advanced Defence Systems (31), they are not considered here).

ERA armour comprises a cassette typically constructed by two thin metal plates (of a few millimetres thickness) and an insensitive (to present initiation by small arms ammunition) explosive layer in between. In use the sandwiched explosive material is detonated by the pressure generated / temperature evolved when a9a shaped-charge jet or other very high KE density threats penetrates the ERA and the front and rear plates are then propelled away from their initial position (32). As the plates fly apart this alters the impact point of the jets as the front and rear plates move parallel along the direction of the jet's path as shown in Figure 1.10 (a) (33). This process imparts significant off-axis momentum to the incident jet, shearing it – and thereby reducing subsequent penetration.

Non-ERA or inert reactive armour (see Figure 1.10 (b) armours usually consist of two metal layers (steel, aluminium or titanium) with a compressed elastic material, for example rubber, sandwiched in between. Upon threat impact, the elastic material will expand and the armour will bulge. This is also effective against shaped charge jets, which are used on rocket-propelled grenades (RPGs) and anti-tank guided missiles (ATGMs) (33). The bulging moves more material into the path of penetration and has a disruptive effect, imparting lateral momentum and weakening the shaped charge jet. Non-ERA or bulging armours have a similar (but less efficient) effect to ERA but importantly (in terms of safety, maintenance, logistics, etc) are without an explosive layer. These armours rely on the use of a dense elastomer or other inert materials. It is also worth noting that non-ERA panels do not stop anti-tank projectiles directly but instead disrupt the projectile's flight path so the main armour behind the Non-ERA layer can deflect or break up the residual projectiles material.

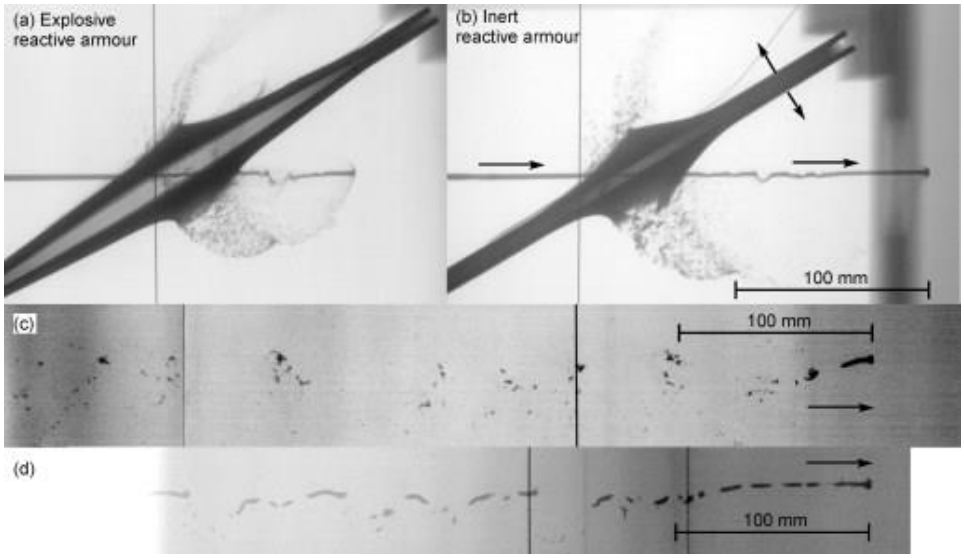

Figure 1.12 X-Ray result images of jet penetration on ERA and non-ERA (33).

Lastly, electric armour studies have been done to observe the effect of an electric on a shaped charge jet. The system works by transferring a large electrical current (~102 kA) to the jet when it hits the 'hot' plate, as described in Figure 1.11. During the contact, the jet between ground and 'hot' plates performs as a switch connecting those two plates simultaneously. This mechanism generates a powerful electromagnetic forces which shears / disrupts the jet and lead it to break up into discrete toroidal rings through a process called Active armour magneto-hydrodynamic pinch (3, 34-36).

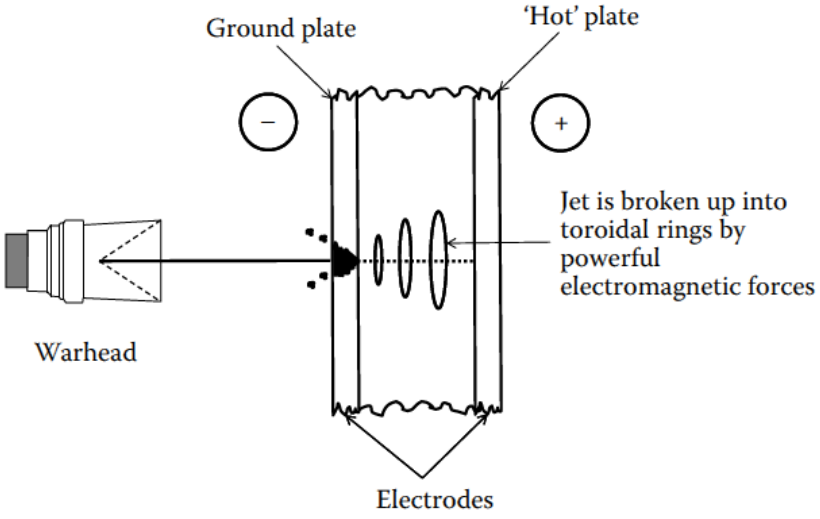

Figure 1.13 The electric armour concept (3).

1.3 Material characteristics

In order to optimise systems (including both projectiles and armour) it is important to fully understand materials properties and their influence on likely ballistic response. For example, electronics components, industrial products, textile and even military equipment, all benefit from an in-depth understanding of the material properties of their components. Moreover, in term of material engineering, an elaborate analysis is needed to provide a detailed explanation about the effect of material characteristics on weapon, ammunition or armour function. In particular, the majority of metallic materials used in military equipment products have well defined behaviour when they are employed, something which allows failure to be controlled. Moreover, they can be designed (or appropriate materials selected) to survive harsh environments to prevent fatigue – something of particular importance for military systems were in-service conditions can be highly variable.

There are numerous properties which need to be considered when product material selection is made, including physical, mechanical, manufacturing, chemical, thermal and magnetic properties. However, for the purposes of this project the key material properties studied to aid in analysis of the penetration mechanism for 12.7 mm armour-piercing projectile in terms of potential defeat of armour are strain, stress, Young's modulus, density, acoustic impedance, shear strength, yield strength, hardness and fracture toughness. In the following sections key definitions are introduced which are employed subsequently throughout this thesis as-required.

1.3.1 Elastic behaviour

When a force is employed on a material surface, a specific force started within the material is termed a *stress*. Stress is calculated as force (F, Newtons) divided by the cross-sectional area over which it is applied (A, m^2). Generally, three types

of stresses are usually set up within a loaded material: tensile, compressive and shear. Application of a tensile stress results in an extension in material length, whereas compressive stress will lead to a reduction in material length. On the other hand, shear stress provides a twist to a material. All of those types of stress will cause a dimensional change of material; this change is termed a *strain*. Under a given stress, a stiff material such as steel and ceramic strains only slightly; whereas a less stiff material such as a polymer (e.g. polyethylene and polypropylene) strains more (37).

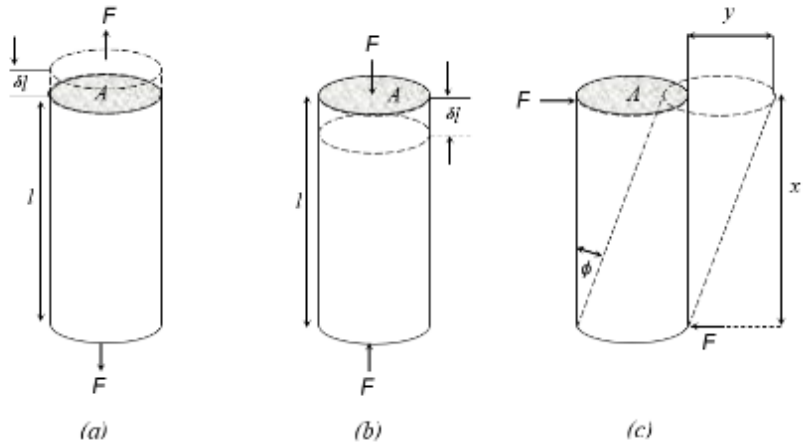

Figure 1.14 (a) tensile stress, (b) compressive stress, (c) shear stress (37).

Figure 1.12 shows stresses set up within a cylindrical section of material – each stress will result in a different change to material dimensions. If a cylindrical bar of length *l* with area *A* is loaded by a tensile force *F,* its length will increase by *δl*. Where tensile stress (σ) is given by σ = F/A and tensile strain is given by ε = *δl/l.* Equivalently, a compressive force (*F*) will decrease the bar length by *δl*, thus a compressive stress (σ) will result in a strain which is describe by ε = - *δl/l*. This minus value shows an opposite direction of dimensional change. On the other hand, a shear force will develop a twist within the material described by an angle ϕ, so the shear stress is given by τ = F/A and a shear strain (γ) will be described by $\gamma = y/x = \tan \phi$ (3, 37).

Generally, all materials exhibit specific behaviour based on their properties. One key material engineering property is the elastic modulus (Young's modulus). This

parameter allows quantification of a material's resistance to elastic deformation (e.g. its stiffness). Lower values correspond to a greater propensity for deformation (e.g. lower stiffness materials such as polymers), whereas higher values are correlated with materials who exhibit a greater resistance (e.g. stiffer materials such as metals). There are several constants to describe a relationship between strain and stress related to Hooke's Law; E, G, K and υ (37, 38).

$$E = \frac{\text{direct stress } (\sigma)}{\text{direct strain } (\varepsilon)} \quad \textbf{(1.1)}$$

$$G = \frac{\text{shear stress } (\tau)}{\text{shear strain } (\gamma)} \quad \textbf{(1.2)}$$

E, *modulus of elasticity* or *Young's modulus*, is a ratio between direct stress and direct strain employed to the material with dimension Pascals (Pa). Similarly, G, the *modulus of rigidity* or *shear modulus*, may be calculated by stress and strain values affected by compressive forces. Its dimensions are also Pascals (Pa) (37, 38).

$$K = \frac{\text{stress (equilateral)}}{\text{volume strain}} \quad \textbf{(1.3)}$$

K is termed the material bulk modulus of elasticity which describes the relationship between stress and strain when equilateral forces are applied to a material. It will result in a material shrinkage (37, 38).

$$\upsilon = \frac{\text{lateral strain}}{\text{tensile strain}} \quad \textbf{(1.4)}$$

The last, υ, *Passion's ratio*, shows a ratio between lateral and tensile strain relating to other elastic constants (37, 38). It essentially describes the effects in terms of lateral flow of compressing an object.

1.3.2 Stress-strain relationship

Shape alternation of materials is caused by a sufficient loading employed to the material. This alternation is termed as deformation. There are two types of deformation, namely elastic and plastic (39). Elastic deformation is a phenomenon which shows a temporary shape change of material self-reversing after the applied force is removed. This deformation is recoverable because the atoms do not slip past other atoms. Whereas plastic deformation occurs when an adequate force is applied to the material surface to alter the material shape permanently. In plastic deformation, dislocation movement of atoms results in breakage of inter-atomic bonds / slip of crystallographic planes past each another.

Figure 1.13 shows how an applied force leads a material to both the elastic and plastic deformation. From this curve, it is important to understand that the linear area describes a relationship between stress and strain in elastic deformation condition. A, is a proportionally limit, while B, shows a yield stress or an elastic limit that is the lowest stress value imparted to the material deforming permanently. Beyond the yield stress, plastic deformation occurs and material shape alterations are not fully recovered. Points C and D are termed as upper and a lower yield points. A further force increase will result in more deformation within the material which leads the specimen to strain hardening. Such strain hardening is primarily an effect of plastic deformation especially in metal because of dislocation movement of crystal structure within material. The maximum stress which the material can withstand without fracture is termed as the maximum engineering stress or ultimate tensile stress (UTS), point E. At this point, the material is susceptible to experiencing necking until the rupture stress where the stress causes material failure (3, 39).

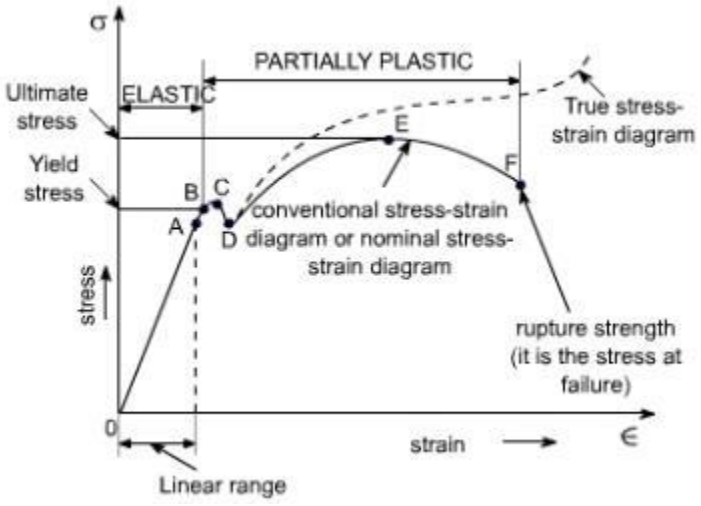

Figure 1.15 A typical tensile test curve for the mild steel

Therefore, the area below the curve in Figure 1.15 is a value of strain energy which is absorbed per unit volume (V). Up to the point of failure, this is a measure of the material's toughness. Further, if the material is impacted to another specimen in elastic deformation condition, the material have a capacity to absorb the collision energy per unit volume without creating a permanent distortion which is named *resilience* (U_r) (3). It can be calculated by integrating the stress–strain curve from zero to the elastic limit.

$$U_r = \frac{1}{2} Y \varepsilon_y \tag{1.5}$$

$$U_r = \frac{\gamma^2}{2E} \tag{1.6}$$

Where ε_y is strain at the yield point, Y is the yield strength and E is Young's modulus and U_r has dimensions of Joule m^{-3}.

1.3.3 Toughness of material

In general, fracture is primarily initiated by a crack within a material. . Difference measures of toughness (essentially a measure of a materials ability to absorb energy up to the point of failure) exist; e.g. Charpy impact toughness, Fracture toughness, etc. Absolute values of these parameters will differ as they are measured using particular geometries. As an example, there are two major parameters which can be applied to material fracture toughness, namely: G_{Ic} (critical strain energy release rate) and K_{Ic} (critical stress intensity factor). The global crack growth criterion is formulated in terms of the energy release rate G and derived from an energy balance. The local stress growth criterion is defined in terms of the stress intensity factor K and derived from crack tip stresses. The subscript I refers to mode I loading (uniaxial) while the subscript c stands for critical. According to Vernon (37) G_{Ic} is known as the *critical strain energy release rate*, and its dimension are J/m^2.

$$\sigma_c = \left(\frac{G_{Ic}E}{\pi a}\right) \quad \textbf{(1.7)}$$

Where σ_c is the critical stress for fracture, E is Young's modulus and a stands for the half crack length.

Furthermore, K_{Ic} is the critical value of the stress intensity at a crack tip required to initiate a failure within a specimen under uniaxial loading (mode I loading). By using the K_{Ic} value, it is possible to calculate the crack dimension required to initiate a fast fracture failure under a specific stress applied as well as the value of stress required to result in failure in a given material specimen. If the material has a high K_{Ic} value, it shows that material has a reliable strength towards applied forces.

$$K_{Ic} = Y\sigma_c\sqrt{\pi a} \quad \textbf{(1.8)}$$

Where *Y* is a dimensionless geometry factor of the order of 1. Ashby and Jones (38) explain that if the crack length *a* is small compared to the plate width, *Y* will be equal to 1.

1.3.4 Relation between fracture toughness, strength and energy required to break

The ability of a material to undertake a limited deformation caused by an applied stress is an important aspect to describe toughness. Typically, High strength materials have a high magnitude of Young's Modulus (E), and they have a low fracture toughness (K_{Ic}) and toughness (G_{Ic}). However, some of them may be a very 'tough' after typical processing. A high stress loading on a high strength material enables local dissipation which leads to material fracture. This is the reason that hard materials tend to be brittle and lower strength materials tend to be tougher (e.g. because the later have a reliable deformation capability (40)). A catastrophic fracture occurs when stored strain energy is released at a rate sufficient to initiate (and propagate) a crack. In a ductile material, for example Copper alloys or Lead alloys, the strain energy set up within the material is absorbed by energy dissipation due to plastic flow in the material near the crack tip, not by creating new surfaces. Whereas in brittle materials, such as ceramics or Tungsten-carbide, there is only a small degree of plastic deformation, so the strain energy is absorbed by creating new surfaces or cracks.

Figure 1.14 shows the fracture toughness of materials characterised by K-factor, K_{Ic}, for various Young's Modulus value. Increasing strength (Y, Yield strength) results in a decrease in the value of fracture toughness. For example, the Steel alloy 4140 tempered at 370^{o}C has a fracture toughness of 55—65 MPa.m$^{1/2}$ and a yield strength of 1,375-1,585 MPa; whereas, after increasing tempering temperature to 482^{o}C, the fracture toughness increases to 75-93 MPa.m$^{1/2}$ and the strength decreases to 1,100-1,200 MPa (41).

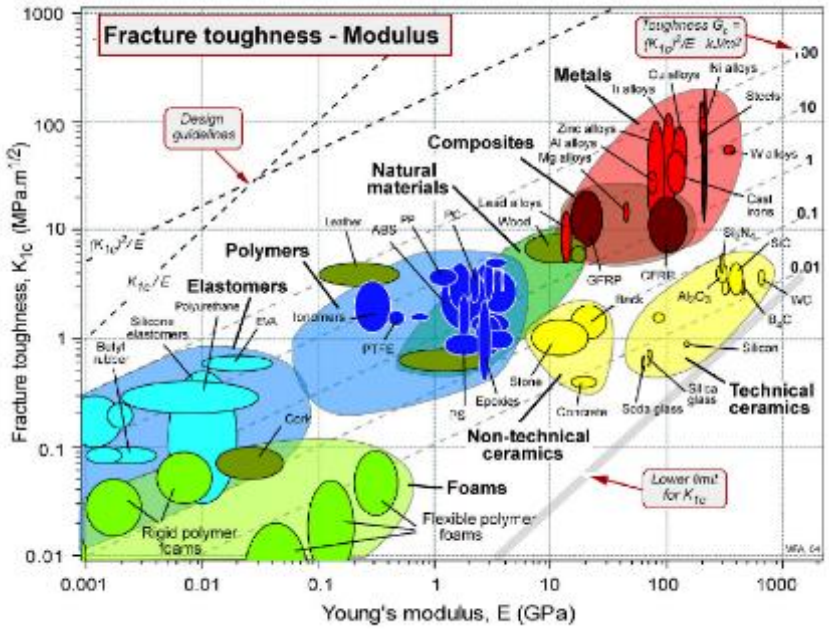

Figure 1.16 Fracture toughness against Young's modulus (42).

As shown in Table 1.3, Tungsten materials, especially Tungsten carbide have a high Young's modulus and a low fracture toughness, 601 GPa and 6-7 MPa.m$^{-1/2}$ respectively; when combined with the materials associated high hardness it may be considered a brittle material. Upon an impact with a lower hardness value material, Tungsten carbide erodes the incoming or target material because of its resistance to indentation, abrasion and wear. However, when a high stress loading which exceeds its strength is applied to the Tungsten carbide surface (for example via impact with a very strong ceramic), it leads Tungsten carbide to experience fast fracture.

On other hand, steel tend to be less brittle than Tungsten carbide. Steel has a higher fracture toughness at 80-170 MPa.m$^{-1/2}$ and lower Young's modulus, 210 GPa. Generally, when a high stress loading is set up within steel, it results in elastic and plastic deformation. That is why steel is able to absorb more energy upon impact. However, impact between steel and a high strength material will disrupt the steel's surface and initiate a fracture. To optimize the steels performance, a proper heat treatment needs to be applied to increase its hardness.

Table 1.3 Mechanical properties of steel and tungsten carbide

Material A	*Y (MPa)*	K_{Ic} (MPa.m$^{-1/2}$)	E (GPa)
Steel	200-1,800	80-170	210
WC	335-530	6-7	601

Interestingly, the failure mechanism of both materials under high strain rates can be affected by shock waves which are transmitted or reflected during the impact.

1.3.5 High strain rate characterisation of material

Material strain rates as a result of impacts vary linearly with the velocity of the specimen impacting the material surface and (by definition) are always a function of time. Strain rates below 10^{-6} s^{-1} represents a *creep* domain; with strain rates below 10^{-3} s^{-1} representing *quasi-static* deformation. In turn, strain rates above 10^{0} s^{-1} can be considered as being part of the *intermediate rate* domain, strain rates of 10^{2} s^{-1} can be classified as high strain rates, and those above 10^{4} s^{-1} are termed as very high strain rates (43). Finally, strain rates beyond 10^{6} s^{-1} are considered as ultra-high strain rates. In defence equipment testing, for example terminal ballistics observation, it was observed that a projectile impacting a target has strain rates from 10^{5} s^{-1} to 10^{6} s^{-1} under high velocity (1,000-2,000 m/s) impact (43). There are several methods used in high strain rate deformation observation of materials and parallel dynamic property consideration. Figure 1.15 captures the relationship between impact velocity and testing approaches.

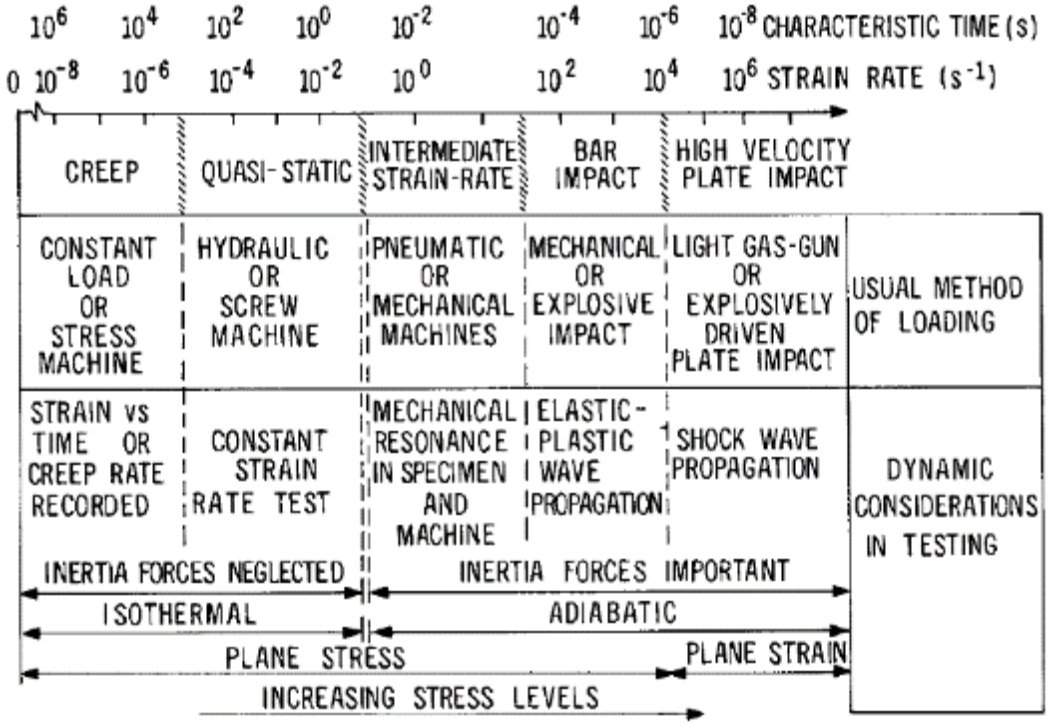

Figure 1.17 Material behaviour with changing strain rates and load duration (44).

It has been observed that increasing stress levels give a strain rate increase. This also affects the microstructure (deformation after impact), and material mechanical properties such as yield stress (which now becomes a dynamic function of loading conditions), hardness and ductility. For example in 310 stainless steel, higher strain rates will result in a decrease in ductility (for loading from room temperature) – a likely due to a thermal softening effect under shock loading (45). Harding (46) explained that impact under high strain rates on materials tends to result in an increase of the ratio of tensile to shear failure strength.

1.3.6 Wave propagation

High velocity impact between two materials can result in wave propagation at certain stress values. Stress waves can result in material failure based on material characteristics. There are two basic types of wave encountered during impact, these are elastic and inelastic (plastic) waves. Elastic waves occurs when

the induced stress is less than the yield strength (elastic limit point) of the material. On the other hand, when a higher dynamic loading is applied to the material surface, the stress wave amplitude will be higher than the material yield stress of the specimen. This phenomenon will lead the material to exhibit both elastic and plastic deformation.

Materials experience wave propagation in the form of transmission and reflection during a collision event. Wave propagation is governed by a material property known as impedance – the square root of the product of Young's modulus and material density (see equation 1.15 below). When an initial compressive wave (σ_I) travels through material A into a material B of higher impedance, a compressive wave (σ_T) is transmitted to material B and a compressive reflection wave (σ_R) is reflected into material A. Thus, this property of 'impedance' is essentially the ability of a material to couple incident energy. When applied to a sound wave through mediums, particle velocity would be the velocity of the continuum elements (atoms or particles) propagating the wave within the material in question. Such wave propagation is illustrated schematically below in Figure 1.8.

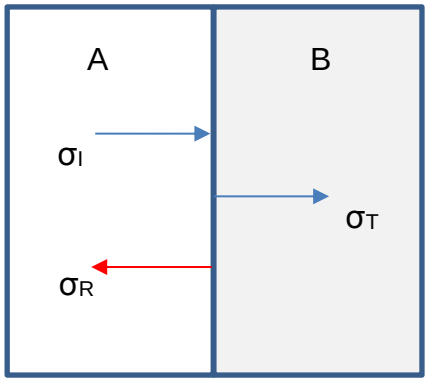

Figure 1.18 The wave propagation after two material impact.

From Figure 1.8, the interface will be in equilibrium at any given point in time. Therefore,

$$\sigma_I + \sigma_R = \sigma_T \quad \text{or} \quad (\sigma_I + \sigma_R)A_1 = \sigma_T\, nA_1 \qquad \textbf{(1.9)}$$

Further, particle velocity will be conserved across the interface (e.g. there will no gaps, and specimen is not able to superimpose upon itself), meaning that,

$$u_{pI} + u_{pR} = u_{pT} \quad \textbf{(1.10)}$$

$$u_{pI} = \frac{\sigma_I}{\sqrt{E_A \rho_A}} \, , \, u_{pT} = \frac{\sigma_T}{\sqrt{E_B \rho_B}} \, , \, u_{pR} = \frac{-\sigma_R}{\sqrt{E_A \rho_A}} \quad \textbf{(1.11)}$$

Assuming continuity,

$$\frac{\sigma_I}{\sqrt{E_A \rho_A}} - \frac{\sigma_R}{\sqrt{E_A \rho_A}} = \frac{\sigma_T}{\sqrt{E_B \rho_B}} \quad \textbf{(1.12)}$$

And from equation above, the ratio's between σ_T and σ_I and between σ_R and σ_I are given by,

$$\frac{\sigma_T}{\sigma_I} = 2\left(\frac{\sqrt{E_B \rho_B}}{\sqrt{E_A \rho_A} + \sqrt{E_B \rho_B}}\right) \quad \textbf{(1.13)}$$

$$\frac{\sigma_R}{\sigma_I} = \left(\frac{\sqrt{E_B \rho_B} - \sqrt{E_A \rho_A}}{\sqrt{E_A \rho_A} + \sqrt{E_B \rho_B}}\right) \quad \textbf{(1.14)}$$

$$Z = \sqrt{E\rho}, \quad \textbf{(1.15)}$$

Where Z = Impedance

The equations presented above give information with regards to the level of stress transmitted and reflected about an interface as a function of the impedance of individual materials (3). Table 1.4 demonstrates this effect for four different scenarios, where the initial material (material A) impedance is the same, lower or higher than that of the rear-most material (material B). For example in Table 1.4, copper which has lower impedance value than steel impacting steel target will transmit a higher stress compared to tungsten impact to steel. Moreover, only

0.10 of incoming stress is reflected to copper as compressive stress compared to 0.37 of incoming stress is reflected to tungsten as tensile stress (' - ' indicates tensile stress).

Table 1.4 Ratios of the transmitted and reflected stress from a wave transiting an interface between copper, tungsten, tungsten-carbide and steel

Material A	**Material B**	**Z_A x10^6 (kg/m^2s)**	**Z_B x10^6 (kg/m^2s)**	**E_A (GPa)**	**σ_T/σ_I**	**σ_R/σ_I**
Copper	Steel	33.01	40.58	122	1.10	0.10
Steel	Steel	40.58		210	1.00	0.00
Tungsten	Steel	88.95		411	0.63	-0.37
WC	Steel	94.11		601	0.60	-0.40

If the transmitted or reflected stress surpasses the yield strength of the material, the material will experience plastic deformation for ductile materials and fast fracture for brittle materials. Brittle materials have a higher strength than the ductile materials, and the higher the yield strength (*Y*), the lower its K_{Ic} (toughness) magnitude. However, as the yield strength increases, the Young's Modulus (*E*) and Impedance (*Z*) will also increase. A high impedance value will lead material to become subjected to more (reflected) tensile stress and consequently become prone to experience spall.

1.4 Steel

Steel is manufacture involve the oxidation of impurities within iron ores. These processes can be carried out by both open-hearth furnaces and the oxygen converter process. Steels may comprise of many impurities as well as the main alloying element of carbon. There are several types of steels: *plain carbon* or *non-alloy steels, alloys steel, low alloy steels* and *high alloy steels.* Those steels have a wide range composition and contain carbon at concentrations up to 5 per cent, along with other elements, such as manganese, silicon, nickel and chromium.

Iron and steels are allotropic and have two crystalline forms; body-centred cubic and face-centred cubic. These crystalline forms are stable in specific temperature ranges, with temperature and pressure change resulting in crystalline shape transformation. Pure iron has three ranges which show crystalline forms, namely: α iron which has a body-centred cubic form which is stable at temperatures up to 908^{o}C, while between 908^{o}C and 1,388^{o}C the crystalline form will be γ iron with a face-centred cubic structure. Further, increasing temperature up to 1,535^{o}C (*the melting point*) produces δ iron with a body-centred cubic structure (37).

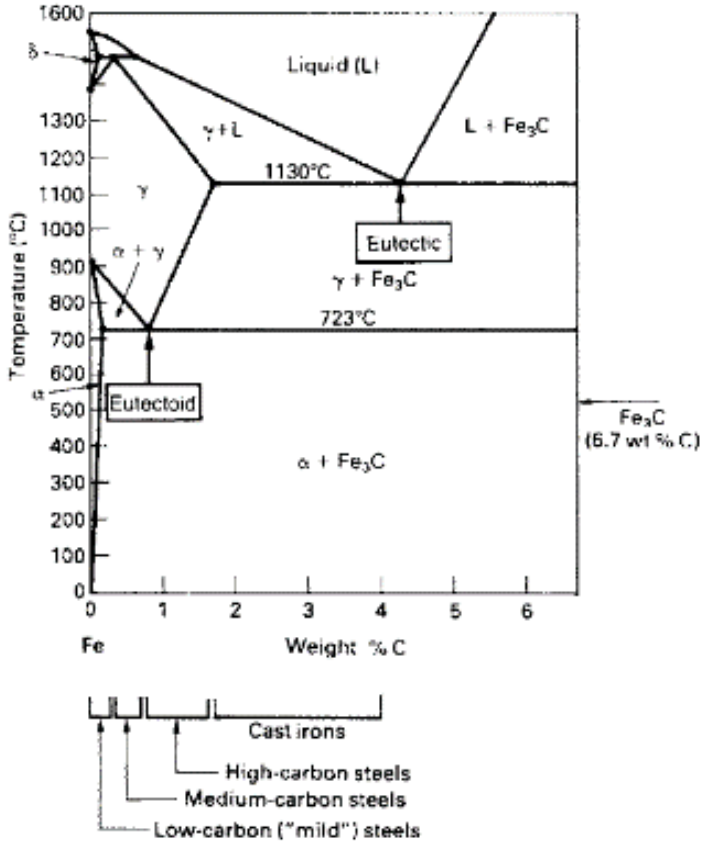

Figure 1.19 Iron-Steel phase diagram (47).

The iron-carbon phase diagram illustrated in Figure 1.19 shows how temperature and carbon percentage affect the structure and phase of steel. The eutectic point (indicated on the diagram) represents a mixture of substances in fixed proportions that melt and freeze at a single temperature which is the lowest melting point of a mixture of components. While the eutectoid is a mixture of substances similar

to a eutectic, but forming two or three constituents from a solid instead of from a melt. Special terms are generally used to denote the various phases and the structure types which exist (37):

a. ***Ferrite*** is the term used to describe α and δ iron as well as solid solutions which have a body-centred cubic structure.
b. ***Austenite*** is the term used to describe γ iron as well as solid solutions which have a face-centred cubic structure.
c. ***Cementite*** has a structure comprising of Fe_3C which is a brittle and hard compound.
d. ***Pearlite*** is produced when austenite decomposes during temperature decrement. Moreover it comprises a eutectoid mixture of cementite and ferrite which has a laminar structure.
e. ***Martensite*** is formed when the specimen at its austenitic state is cooled rapidly to form a highly supersaturated ferrite with dissolved carbon. It is very hard and brittle.
f. ***Bainite*** is the name used to describe the product of austenite decomposition in isothermal transformation or at an intermediate cooling rate.

Different carbon contents as well as hot working and various cooling treatments of steels give different physical characteristics (37). For example:

- Slow cooling of a hypo-eutectoid (a lower carbon content that the eutectoid point) form from the hot working temperature results in austenite transformation to ferrite and a eutectoid mixture of pearlite.
- In contrast, slow cooling of hyper-eutectoid (carbon content above that of the eutectoid point) steels after heating at high temperature produces a structure which alters austenite to pearlite in a eutectoid composition, which has precipitated carbon which remains as cementite. Moreover, cementite works as a boundary to the pearlite phase, increasing the steels strength.

- A rapid cooling from the hot working temperature alters austenite to be coarse pearlite, fine pearlite, bainite and martensite at increasing cooling rates.

The higher the cooling rate, the higher the resultant material hardness. Material hardness is related to carbon content of steel, and martensite increase the hardness of steels significantly.

Martensite is very hard, but it is also very brittle. A post transformation heat treatment is necessary to modify the steel properties in order to ensure good performance – for example, tempering. When a martensitic metal is heated at 300-600^{o}C, it can regain the lost toughness with a moderate hardness decrease. In tempering, it is possible for carbon to dissolve out from the highly supersaturated ferrite to precipitate and form Fe_3C (47). The lattice then returns to a body-centred cubic structure and as a result material ductility increases. An increase in terms of the tempering temperature will increase the rate of diffusion and precipitation, hence it will soften the material and release the internal stresses generated after hardening.

Steel performance for armour applications can be increased by annealing, hardening, tempering and also a spheroidising process as well as surface hardening treatments such as carburising, nitriding, cyaniding and, carbonitriding. An optimal set of heat treatments to increase the strength of steels involves hardening at 30-50^{o}C above the upper critical temperature followed by rapid quenching in water and a carburising surface heat treatment. The upper critical temperature is temperature above which the austenite phase is stable. A further heat treatment after hardening would then be tempering to relax material internal stresses (as with martensite). Moreover, the presence of alloying elements also improves the hardenability, gives the potential for solution strengthening and precipitation hardening (in certain case), can increase corrosion resistance and also stabilise austenite at room temperature (37, 47).

1.5 Numerical simulation

The development of ammunition, especially medium and large calibre ammunition, as well as armour materials is a very expensive undertaking because it involves many ballistic trials with numerous parameters which can affect the outcome. Consequently, numerical simulation has over recent years come to the fore as a tool to analyse ballistic impact behaviour. Such numerical simulations are usually complementary to / are calibrated and compared with experimental data. By using the calibrated parameters and applying them in numerical simulations, it is possible to reduce cost and time for collecting research data.

1.5.1 Numerical simulation development

Numerical simulations have been widely applied within both armour and anti-armour research to facilitate better understanding of complex dynamic behaviour with benefits including reduced cost, increased speed and attention to detail. In numerical simulations, systems are discretised in an appropriate manner and the effects of applied loads on these elements considered. Essentially, the material behaviour during the dynamic event is calculated step by step with each resultant strain increment leading to an associated stress change. Systems (e.g. projectile / armour combinations) can be modelled as 2-D or 3-D constructs using either finite element or finite difference methods as well as allowing for both linear and / or non-linear behaviour (10).

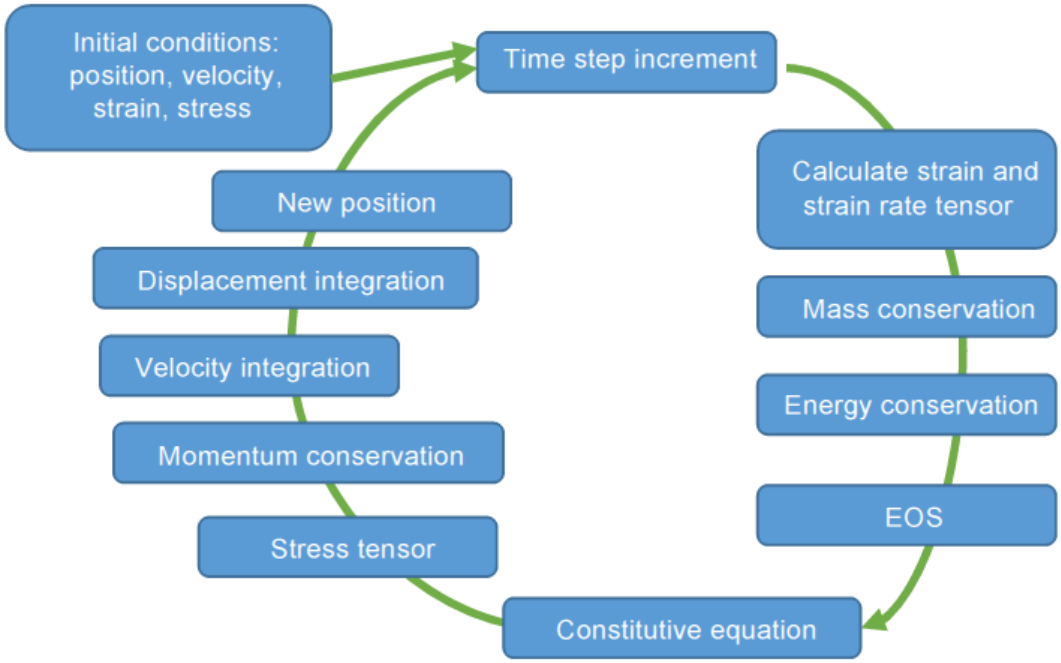

Figure 1.20 Typical integration scheme utilised in a hydrocode (10).

Numerical modelling for impact events are usually conducted in hydrocodes which are numerical program specialised for solving material behaviour related problems during impact / dynamic events. According to Zukas (44), the hydrocode term describes a hydrodynamic (fluid-like) behaviour which is assumed for high strain rate impact events. Most hydrocodes solve short-term problems by implementing an explicit formulation which is preferable for small time steps.

These are numerous studies which have implemented numerical simulation for impact-related phenomena in the literature. Modellers use different combinations of software system, solvers, equation of state, strength model, damage criteria, and erosion function of models as required for a given problem – as shown in Table 1.5.

Table 1.5 Fundamental parts of applied numerical models (10).

Aspect	Example	Comment
Software system	Autodyn, LS-Dyna	Now ANSYS (via LEAP Australia)
Solvers	Lagrangian, Eulerian, ALE, SPH	Select, as appropriate
Equations of state	Linear, bulk, shock, etc	Conservation of energy and momentum
Constitutive equations (strength models)	• Modified Zerelli–Armstrong	• Numerous models
	• Johnson–Holmquist	• Requires determination of constants
	• Cowper–Symonds	• Requires high strain rate material characterisation data
		• Use anisotropic values, if available
Damage criteria	Johnson–Cook parameters	Requires another set of input data
Contact algorithms	Coulomb friction	How to treat interfaces
Cell erosion	Critical strain	How to attribute energy when cells become too distorted

In a typical study, Johnson and Cook (48) conducted computational work using the Lagrangian EPIC code to simulate oblique and yawed rod impact on thin single and spaced steel plates at various velocities. The simulation results were found to be similar to both experiments and previously published computational work conducted using the Eularian MESA code. Usefully, however, the simulation time of the Lagrangian EPIC code was shorter than for the Eularian MESA code results previously published.

In similar work, Iqbal et al. (49) conducted three-dimensional numerical simulations of sharp nose projectile impact against ductile materials. A three-dimensional finite element (FE) model was constructed by using ABAQUS/CAE as shown in Figure 1.19. The projectile was modelled as analytical rigid part and the target as a deformable body. This work was then compared with previous experimental and axi-symmetric numerical results. As with the study by Johnson

and Cook (48) it was again found that the results were in a good agreement with the experimental studies. Numerical simulation of 7.62 and 12.7 mm projectile impact to high hardness steel (Armox 500T) has been also been conducted using calibrated material models (50), illustrating the breadth of simulation based work previously presented in the literature.

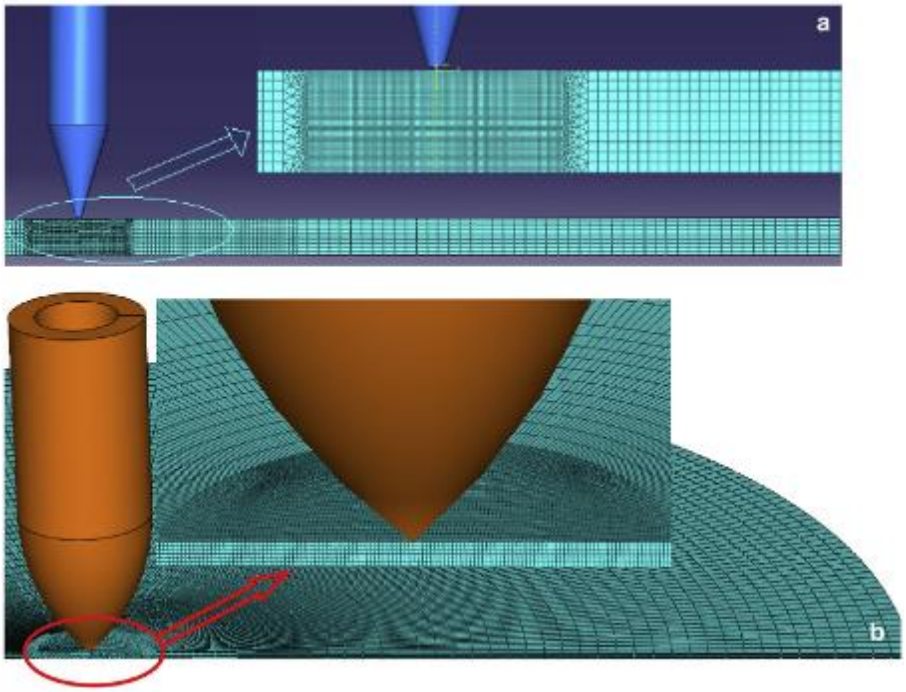

Figure 1.21 Finite element model: (a) thick steel plate target; (b) thin aluminium target (49).

Some numerical simulations in the literature have been conducted by implementing LS-DYNA (6, 51-54). The LS-DYNA package is a multi-physics solver widely known as an explicit code intended for short term dynamic event simulations. For example, Kilic and Ekici (6) have conducted ballistic limit testing of 500 HB armour steel against 7.62mm API hardened steel core ammunition. A three-dimensional numerical simulation was carried out using both Lagrange and smoothed particle hydrodynamics (SPH) simulations. Both Johnson-Cook strength and failure models (discussed in more detail later in this thesis) were implemented to reproduce projectile and steel armour failures observed in the experimental work. Similar simulations with the same method were also performed to investigate explosively formed projectile (EFP) impact into concrete

targets, perforation of sandwich panels with an aluminum foam core, and steel armour impact modelling in different oblique angle (52-54).

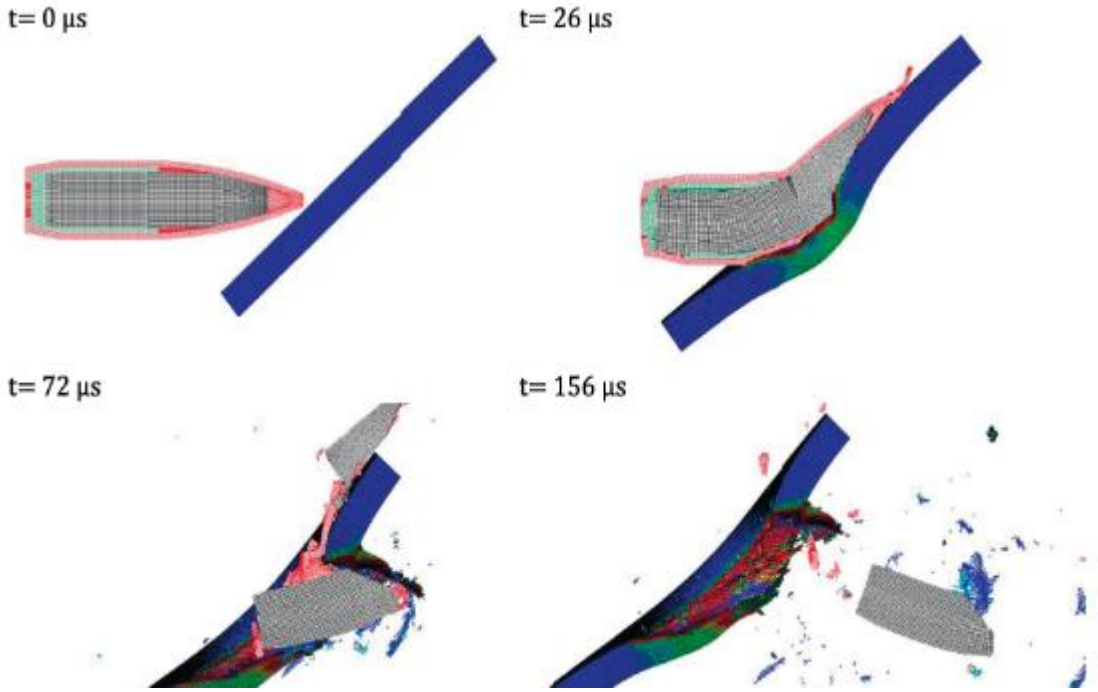

Figure 1.22 A sequence of plots describing the perforation of steel plate by 7.62 mm AP bullet at 50^{o} impact obliquity (52).

1.5.2 Modelling method

The commercial hydrocodes ANSYS explicit dynamics and ANSYS Autodyn® have been used in this study to simulate the impacts between the projectile and steel target plate. Both programmes are part of ANSYS Workbench suite, version 18.1. ANSYS Autodyn® consists of multiple solvers for different material characteristics which also can be combined for highly complex programs. Some common method which are used in simulation of high velocity impact are as follows (55-56):

a. ***Finite element for structural dynamics (Lagrange)***

   In this method, the mesh is integrated with the material and during deformation the associated elements are always in the same relative position as before. This method allows the system to track materials and material flow easily. Contact between two materials can be determined as

contact of nodes and element edges. When a large deformation occurs, the elements will be distorted and lose their accuracy. The time step is defined from the smallest element in the system so the simulation can run at a small time step that will increase the computation time. In order to solve the problem above, the erosion method is often applied in certain condition based on material characteristics. When using the erosion method during simulation, it is possible to retain the nodes from eroded elements as well as keep kinetic energy in the system.

b. Finite volume for transient fluid dynamics (Euler)

In the Euler method, the mesh is established and material flows through the mesh from one cell to another cell. The Lagrange method problem is eliminated because the cells do not experience distortion and large deformations do not affect the simulation's time step.

c. Adaptive mesh for structural dynamics with large deformation (ALE)

The Arbitrary Lagrange Euler (ALE) approach is a combination of the Lagrange and the Euler methods. This method runs as a Lagrange simulation with mesh deformation, within which an interval of iterations is set to restructure the mesh and prohibit highly skewed elements from being generated. During the restructuring, the stresses and deformations are moved from former nodes to new elements and nodes which is the same method with the Euler method.

d. Mesh-free particle for large deformation and fragmentation (SPH)

Smoothed-Particle Hydrodynamics is a mesh-free method where the nodes are not associated with elements or cells. By doing so, the large distortion and infinitesimal time steps associated with elements are eliminated. Material failure and fracture are also defined more naturally.

1.5.3 Material models

Material models in dynamic simulations comprise of multiple parts depending on material behaviour and application. These range from simple linear models for static behaviour to complex ones with many factors involved. Different parts can be combined together to provide an accurate simulation (55-56). Some of the models usually used in ballistic impact event are the Equation of state (EOS), strength and failure models.

An equation of state (EOS) is a relation between pressure (hydrostatic stress) applied on a given material, local density, and local specific energy. Hooke's law is the simplest expression of an equation of state and it is formulated as bulk modulus. The bulk modulus describes a linear relation between hydrostatic stress and change in volume, and does not calculate temperature effects (essentially, the EOS deals with volumetric effects but not deviatoric – or strength – ones). Hooke's law is only valid for linearly elastic materials which usually experience only ca 2% of volumetric change up to the elastic limit. In ANSYS Autodyn®, this simple EOS is applied as a linear EOS. Some of the steel models in the ANSYS library use a shock EOS. According to ANSYS, this EOS is established from the Rankine-Hugoniot equations for shock conditions (57). It also relates the hydrostatic stress to density change, specific energy and particle velocity. The Mie Grúnessian gamma formulation of the shock EOS is presented in the equations shown below (55).

$$p = p_H + \Gamma \rho (e - e_H) \quad \textbf{(1.16)}$$

$$p_H = \frac{p_0 C_0^2 u\,(1+u)}{(1-(S-1)u)^2} \quad \textbf{(1.17)}$$

$$e_H = \frac{1}{2}\frac{p_H}{p_0}\left(\frac{u}{1+u}\right) \quad \textbf{(1.18)}$$

$$u = \frac{\rho}{\rho_0} - 1 \quad \textbf{(1.19)}$$

Where p is pressure, u is particle velocity, e is specific energy, C_0 is bulk sound speed named as C_1 in the ANSYS library, S is the Hugoniot linear slope coefficient (in the shock velocity / U_S – particle velocity / u plane) named as S_1 in the library, e is specific energy and Γ is the Gruneisen coefficient.

During an impact event, a large plastic (as well as elastic) deformation of the materials involved will likely occur. Generally, the deformation element of the event represents the material strength. One of the most famous strength model is the Johnson-Cook (JC) model which was introduced by Johnson and Cook (48) to observe material behaviour in various strains, strain rates, pressures and temperatures. In this model, thermal softening, strain and strain-rate hardening are all taken into account. All required material parameters were derived from three test procedures (10):

- A torsional test for strain rates between quasi-static to 400 m/s.
- Split-Hopkinson pressure bar (SPHB) tensile tests at different temperatures.
- Quasi-static tensile tests.

Experimental results from the three test detailed above are combined to simplify the model and provide a reasonable accuracy when employed in numerical codes (10, 48). The Johnson-Cook model can be described as follows:

$$\sigma_{eq} = [A + B\varepsilon^{n}]\,[1 + C\ ln\acute{\varepsilon}^{*}]\,[1 - T^{*m}] \quad \textbf{(1.20)}$$

$$\acute{\varepsilon}^{*} = \acute{\varepsilon} / \acute{\varepsilon}_0 \quad \textbf{(1.21)}$$

The three terms in equation (1.20) represent the following:

1) The first bracket equation represents the yield stress increase due to strain hardening. Where A is the yield strength, B is the strain hardening, ε is the equivalent plastic strain and n is the strain-hardening exponent.
2) The second bracketed term describes the yield stress increase with strain-rate increment. Where C is the strain rate constant, $\acute{\varepsilon}$ is the equivalent

plastic strain rate and ε* is the dimensionless plastic strain-rate for the reference strain rate ($\dot{\varepsilon}_0$) is 1.0 s^{-1}.

3) Finally, the last term of the JC model is homologous temperature T*. This expression describes the thermal softening of the material because of thermal plastic instability.

It is worth noting that the JC model is only one approach and that other strength parameters are also applied in numerical simulations, for example The Steinberg-Guinan, bilinear or multilinear hardening, and the Zerilli Amstrong model.

At typical high load values, especially in hydrocodes where pressures can be very high magnitude, materials will experience failures. Capturing the effects of these material failures is one of the important factors in hydrocodes studies. To simulate this, failure is divided into two parts that are failure initiation and failure response. Several parameters are used in determining failure initiation, for instance plastic strain, principle stress failure, Johnson-Cook failure and more. While post-failure response can involve both instantaneous and gradual failure (52).

1.6 Project to be undertaken

As detailed previously, in this study armour-piercing penetration of metals and other hard materials has been investigated. The 12.7 mm projectiles were used for the experiments. Penetration of 12.7 mm projectiles on high hardness steels were observed by measuring residual velocity – with a particular focus on gilding jacket effect on penetration (an area identified in the literature as important, but where additional insight has been identified in the literature survey as being potentially beneficial). Moreover, penetration mechanism was observed by capturing Flash X-Rays images and numerical simulation. Further, the influence of both different projectile materials and variations in their hardness (accessed via differing heat treatments) was also examined.

2 Materials

In this study, copper jacket was produced and attached to steel cores to observe the effect of the copper jacket to projectile performance into Armox Advance penetration. En8 and M2 steel core were used in the experiments. En8 steel was used to produce initial core samples because it was able to be heat treated at Cranfield University's Shrivenham Campus where the experiments were being undertaken. In contrast, M2 steel needed to be procced in a vaccum oven to produce the desired / targeted hardness conditions, nessecitating off-campus processing. Consequently, the En8 steel cores were used to conduct initial experiments to validate experimental processes / investiagte mechanims before the main experiments with three M2 steel hardness conditions were undertaken. A 5 and 9-mm thick Armox Advance were also applied in this experiments to give insight into projectiles penetration in different plate thickness.

2.1 Materials list

A number of different materials were employed in the experiments discussed in this thesis. These comprised of:

1. 5 and 9-mm thick Armox Advance plate were used as target materials during forward and reverse ballistics testing. The plates were cut into 45-mm diameter or 150 mm x 150 mm rectangular shapes as-required. The plate's hardness was measured as 58-63 HRC.
2. En8 and M2 Steel were used for projectiles.
3. Finally both 30 and 50-mm diameter Acetyl sabots were employed as-required.
4. 12-mm thick PMMA backing (~60x60 mm^2), 8-mm aluminium 7075 target (~60x60 mm^2), and 25 mm Mylar^{TM}.

2.2 Equipment list

Key equipment employed consisted of:

1. 30-mm bore, 4.5-m barrel single-stage gas gun
2. 50-mm bore, 6-m barrel single-stage gas gun
3. Four channel Scandiflash Flash X-Ray system (operating at up-to 350 kV per-channel)
4. High speed video cameras (of type V7 or V12 as-required manufactured by Vision Research)

2.3 Projectiles preparation

The projectiles employed in the sequence of experiments discussed in this thesis were prepared in Cranfield University's workshops. There were two types of bullets produced: a projectile with a copper jacket and one without copper jacket – in both cases these were assembled into a brass driving band projectile body. Those bullets were processed from En8 Steel and M2 Steel as-required. The bullet calibre is for 12.7x99 mm ammunition with a 12.7x99mm armour piercing ammunition. Details of the projectiles manufactured are given Table 2.1 along with Figure 2.1.

Table 2.1 Samples used in experiments.

Material type	Hardness	With copper jacket	Without copper jacket
En8 Steel	52-53 HRC	20 pcs	20 pcs
M2 Steel	42-45 HRC	20 pcs	20 pcs
	52-55 HRC	20 pcs	20 pcs
	62-65 HRC	20 pcs	20 pcs

The projectile samples were also prepared for V_{50} (velocity-50%) test, but the test was not able to be conducted due to the Cranfield University's Ballistic Range closure.

(a) with copper jacket (b) without copper jacket

Figure 2.1 12.7mm armour piercing projectiles: (a) with jacket and (b) without jacket.

A copper jacket addition to the steel core resulted in a 3 gram heavier of jacketed projectile. The average mass of the unjacketed core was 27 gram, while the jacketed core was 30 gram. This discrepancy generated a different kinetic energy of the projectiles in the case where the projectile was fired into stationary Armox Advance targets. The kinetic energy of the unjacketed core at 750 m/s velocity was 7.8 kJ compared to the kinetic energy of the jacketed core of 8.4 kJ at the same velocity. This condition would have led to some errors in the data in the Forward Ballistic tests and is consequently considered in subsequent discussions.

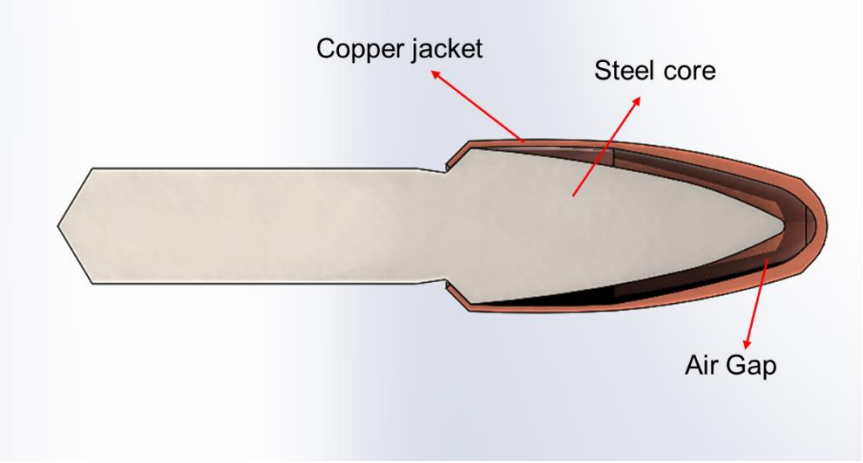

Figure 2.2 Cross-sectional view of jacketed projectile.

2.3.1 En8 and M2 steel heat treatments

Further details of the two steels employed for projectiles, along with details of the heat treatments employed for each, are presented below:

- **En8 carbon steel** is a medium carbon and medium tensile steel, with improved strength over mild steel, through-hardening medium carbon steel. EN8 steel is also readily cut in any condition. In the manufacturing process adopted here, En8 steel round bar was machined before the heat treatment process. A batch of the En8 steel cores were hardened at 860^{o}C for 20 minutes then oil quenched. This was followed by a tempering heat treatment at 250^{o}C for 40 minutes before air cooling (58).
- **M2 steel** is molybdenum-type high speed steel with excellent material toughness and cutting properties. In this case the M2 steel round bar was also machined to form the core geometry before the heat treatment process. In this study, three hardness conditions were used to observe the influence of hardness on penetration mechanism. A batch of steel cores was pre-heated at 700^{o}C and 870^{o}C and then ramped to 1190^{o}C. The steel cores were quenched with nitrogen gas at a pressure of 3 bar. To give three different hardness conditions, there are three tempering temperature which were subsequently applied for the following heat treatment step as shown below (59).

Table 2.2 Tempering condition for M2 steel cores

No	Tempering Temperature (^{o}C)	Holding time (minute)	Hardness result (HRC)
1	680	120	42
2	640	120	52
3	540	120	62

2.3.2 Copper jacket production

In this study, a typical new copper jacket design was used to examine its effect on the penetration mechanism of steel cores into Armox Advance plate. The copper jacket was made from a C101 copper with 1.5-mm thickness (60). Generally, the copper jacket of a projectile is produced by using an industrial automatic punching or drawing machine or a simple set of punch and die tools. In this study, however, the copper jacket was manufactured in Cranfield's Workshops using 20 sets of punch and dies tools via the following core stages:

- First, a coin-shaped piece of copper disc is punched out of a strip or a sheet. The punch is usually a round metal cylinder that is pushed through the jacket material into a die.

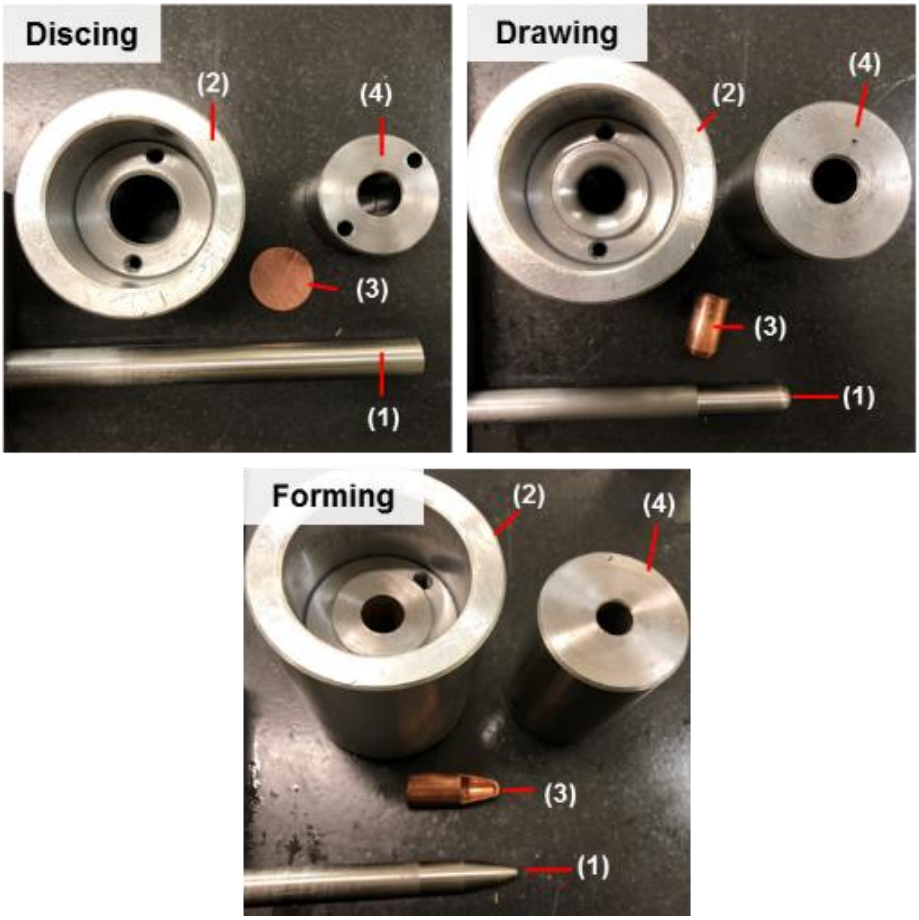

Figure 2.3 Tool set for discing, drawing and forming step in copper jacket production. (1) punches; (2) dies; (3) punch holders; (4) outputs.

- Next, the jacket material is then placed in a drawing die or over a punch and the punch is forced into the die. This method is applied from step 2 to 18 and may involve several different punches and dies which are used to form specific features in the jacket. Figure 2.2 shows dies and punches design for discing, drawing and forming step.
- At the eighteenth step, the copper jacket is annealed with gas torch until become cherry red. This annealing increase material ductility and allows copper jacket to be stretched more as well as prevent cracking.

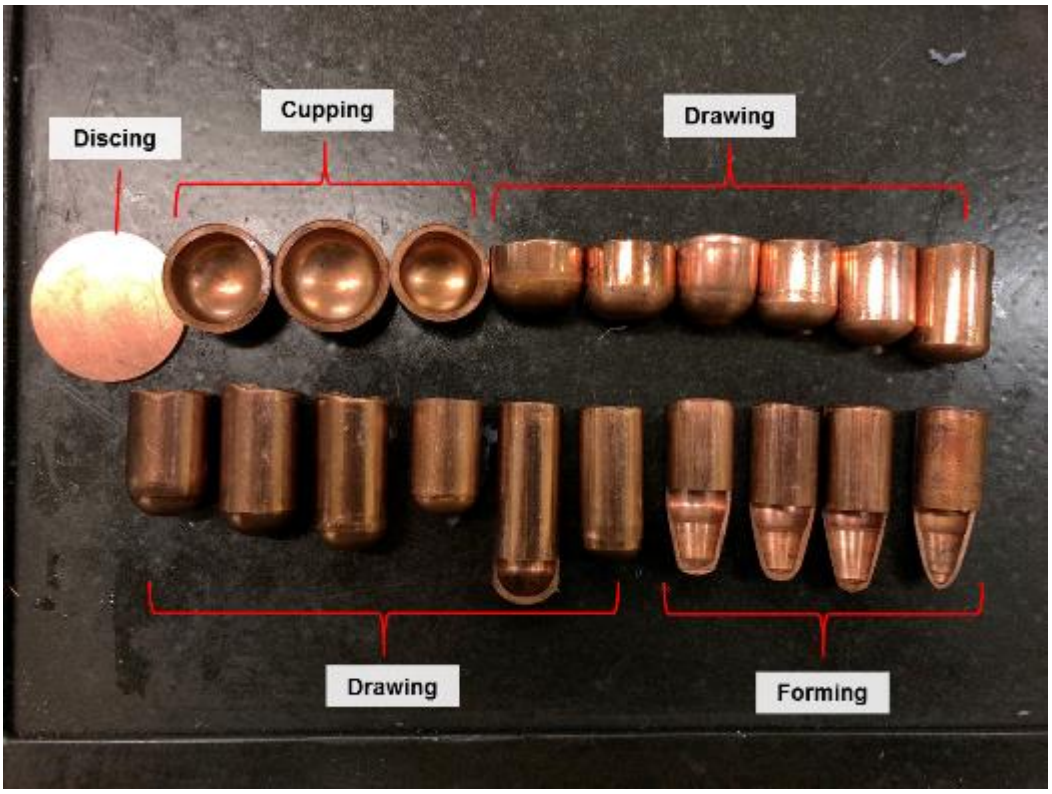

Figure 2.4 Copper jacket production steps.

2.3.3 Hardness measurement

All materials hardness were measured using micro hardness Vickers tester. The Vickers hardness value was converted to Hardness Rockwell C (HRC). The samples were embedded into plastic resin mixture and let them dry. The prepared samples were ground and polished to provide very smooth surface, so the indentation was clearly defined. Particularly at lower forces, a rough surface, or a surface affected by grinding or filing will give inaccurate results.

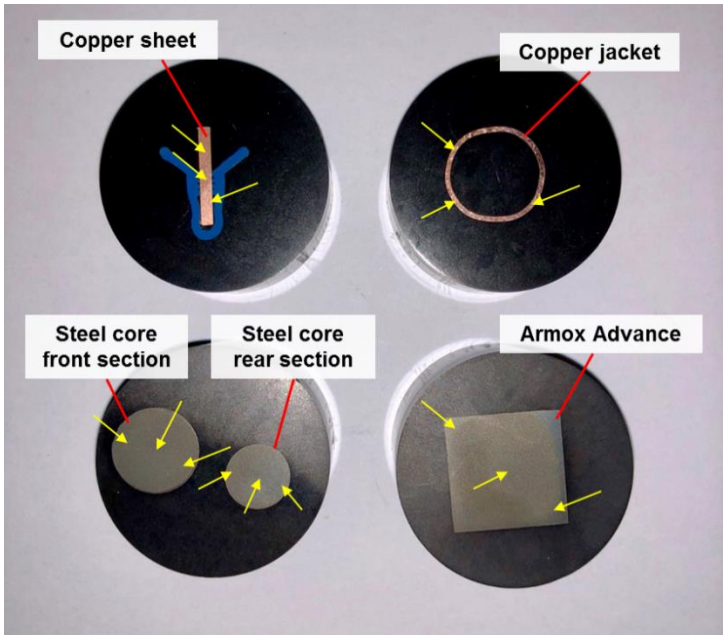

Figure 2.5 Top view of hardness measurement samples (copper sheet, copper jacket, steel core and Armox Advance plate).

The hardness value of materials were measured in various position as shown by yellow arrows in Figure 2.5 to give average hardness value.

3 Experimental set-up

All ballistics tests are to be carried out within the Dynamic Response Group Laboratory at Cranfield University, Shrivenham, United Kingdom.

3.1 Forward-ballistics experiments

Forward ballistics testing were be carried out using a 30-mm bore single-stage gas gun. This was used to launch saboted-projectiles into desired target material. The experiments were designed to investigate the effect of the gilding jacket on projectile penetration towards steel plates. In these experiments as shown in Figure 3.1 and 3.2, no backing material was employed during the shots. Instead, the projectile was simply fired through the target material to analyse the energy loss for the two types of bullet under consideration (see Figure 3.3). The projectile velocity after leaving barrel was nominally 765 ± 20 m/s, confirmed by measurement using light gates. The velocity before and after perforation was also be measured via high speed camera, with this data than employed to confirm a kinetic energy loss because of the projectile and steel plate impact.

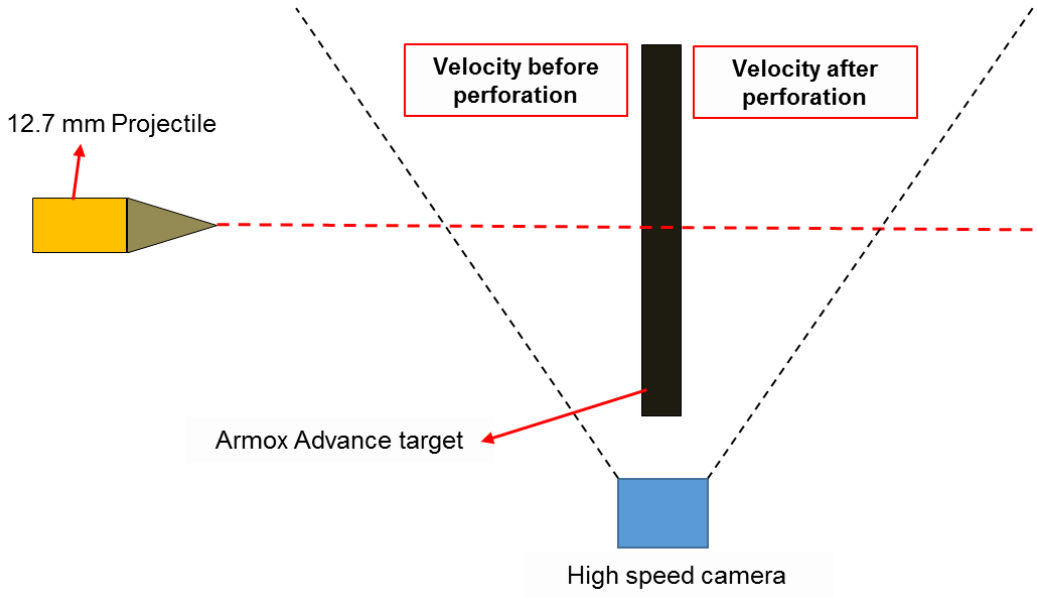

Figure 3.1 Schematic illustration (not to scale) showing experimental set-up for the forward ballistic tests to measure bullet's velocity before and after impact.

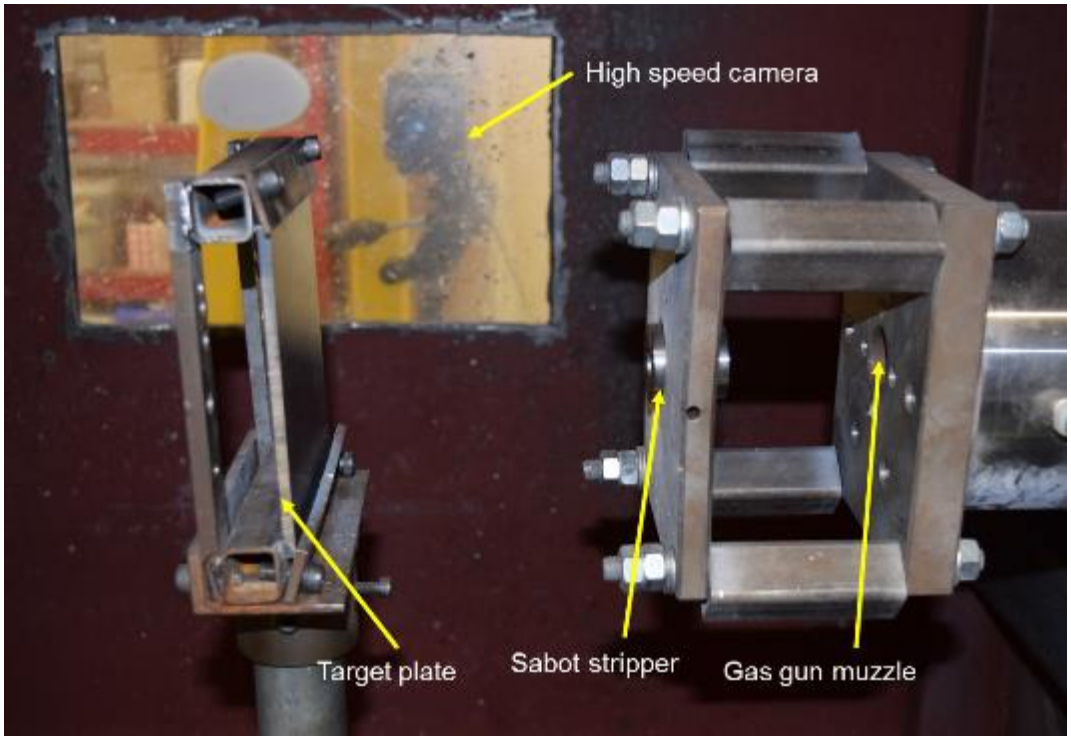

Figure 3.2 Experiment set up inside gas-gun target chamber.

Figure 3.3 Jacketed and un-jacketed projectiles embedded in 30-mm diameter sabot.

Forward ballistic test was the simplest experiment compared to other experiments. Moreover, residual velocity of projectile fragments were able to measured using this method. However, fragments movement along z-axis and parallax phenomenon affected the velocity measurement accuracy. Moreover, the projectile mass discrepancy influenced the results due to the kinetic energy difference at the same velocity.

3.2 Reverse-ballistics experiments

The reverse ballistics experiments using both jacketed and unjacketed projectiles and were conducted using the apparatus shown schematically in Figure 3.4, comprising a 50-mm bore single-stage gas gun (61) with projectile impact velocities of 750 ± 20 m/s (Figure 3.6 (a)). This gun launched the steel-plate targets fixed to acetal sabots towards stationary projectiles mounted on a polycarbonate support structure (Figure 3.6 (b)). This approach eliminates the yaw associated with a small projectile in a large sabot and, importantly, ensures that impact occurs at a precise spatial point to facilitate analysis. Moreover, observation of different projectile designs was able to be conducted without kinetic energy discrepancy because the projectiles were prepared as stationary object. Just before impact, a Scandiflash four-channel flash X-ray system was initiated via a laser light gate and delay mechanism to capture radiographs at precise 10-μs intervals (impact occurred nominally 30 μs after light gate activation). Four radiographs were produced per impact, designed to visualize the impact and determine the penetration mechanism.

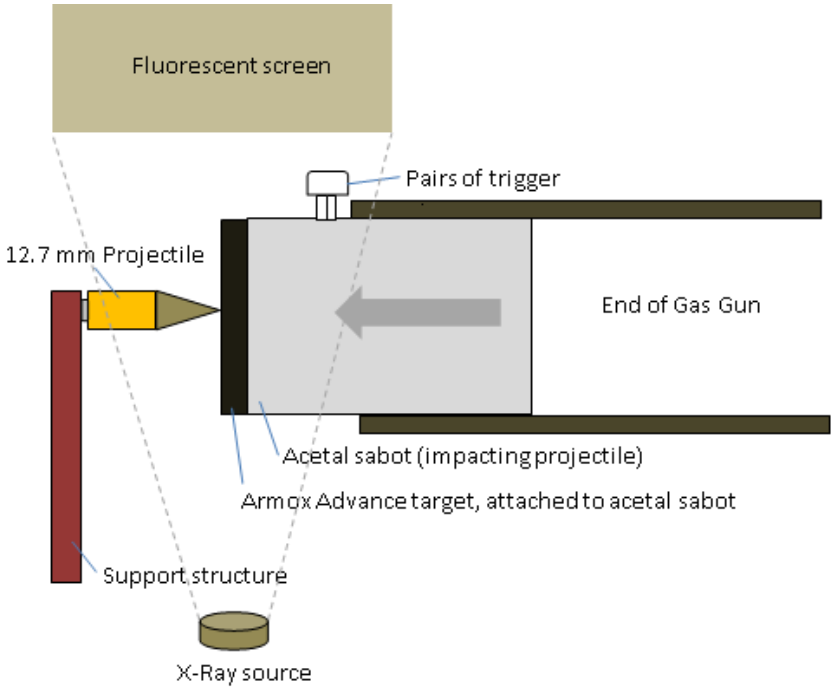

Figure 3.4 Schematic illustration (not to scale) describing experimental set-up for the reverse ballistic.

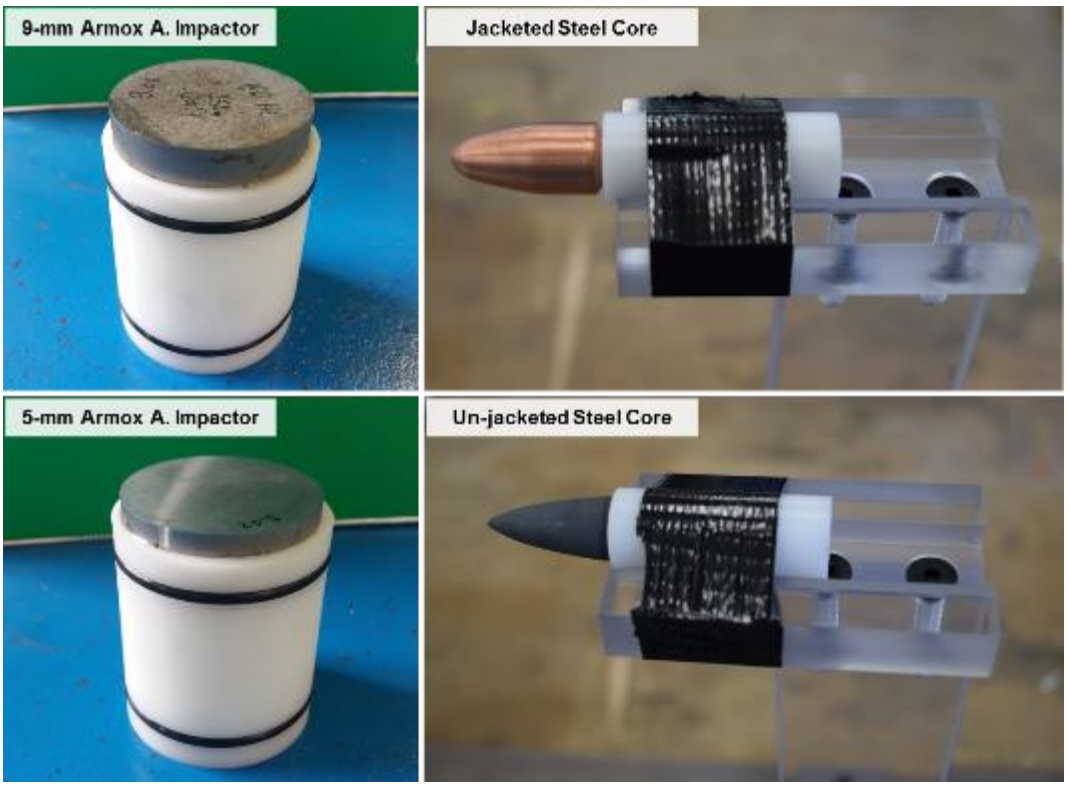

Figure 3.5 Impactors and projectiles used in reverse ballistic experiment.

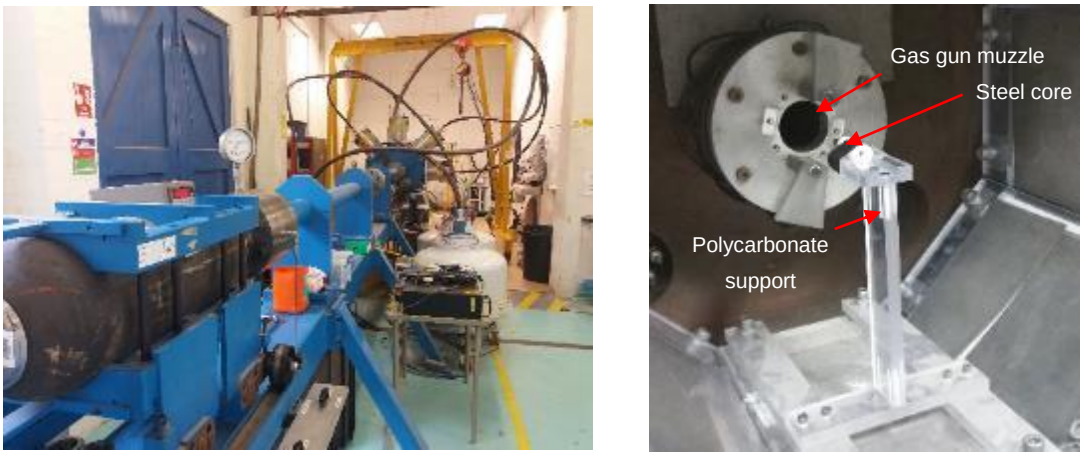

(a) (b)

Figure 3.6 The key elements of the reverse ballistic experiments. (a) Compressed gas-gun viewed from the breech end plus flash X-ray system (silver cylinders radiating from target vessel). (b) Core on polycarbonate mount positioned in front of the muzzle.

In this study, reverse ballistic experiment was used to observe the penetration mechanism qualitatively through captured x-ray image. To explain further insight in penetration behaviour, the reverse ballistic experiment must be followed by forward ballistic and pressure gauge experiments as well as numerical modelling.

3.3 Pressure Gauge Experiment

Impact tests comprising form of plate-impact experiment with Manganin pressure gauges (62-64) were employed to investigate the pressure on the targets during impact. A 50-mm single-stage gas gun was used for these shots (61). An 8-mm aluminium 7075 target (~60x60 mm^2) was placed in front of a 12-mm PMMA backing plates of the same size. A 25-μm thick insulating Mylar™ sheet and a Manganin™ gauge (48.0 Ω, Vishay LM-SS-125CH-048) were introduced between the aluminium target and PMMA backing plate as shown in Figure 3.7 (a). All components were bonded together using an epoxy adhesive (Loctite® EA 3421) and clamped overnight.

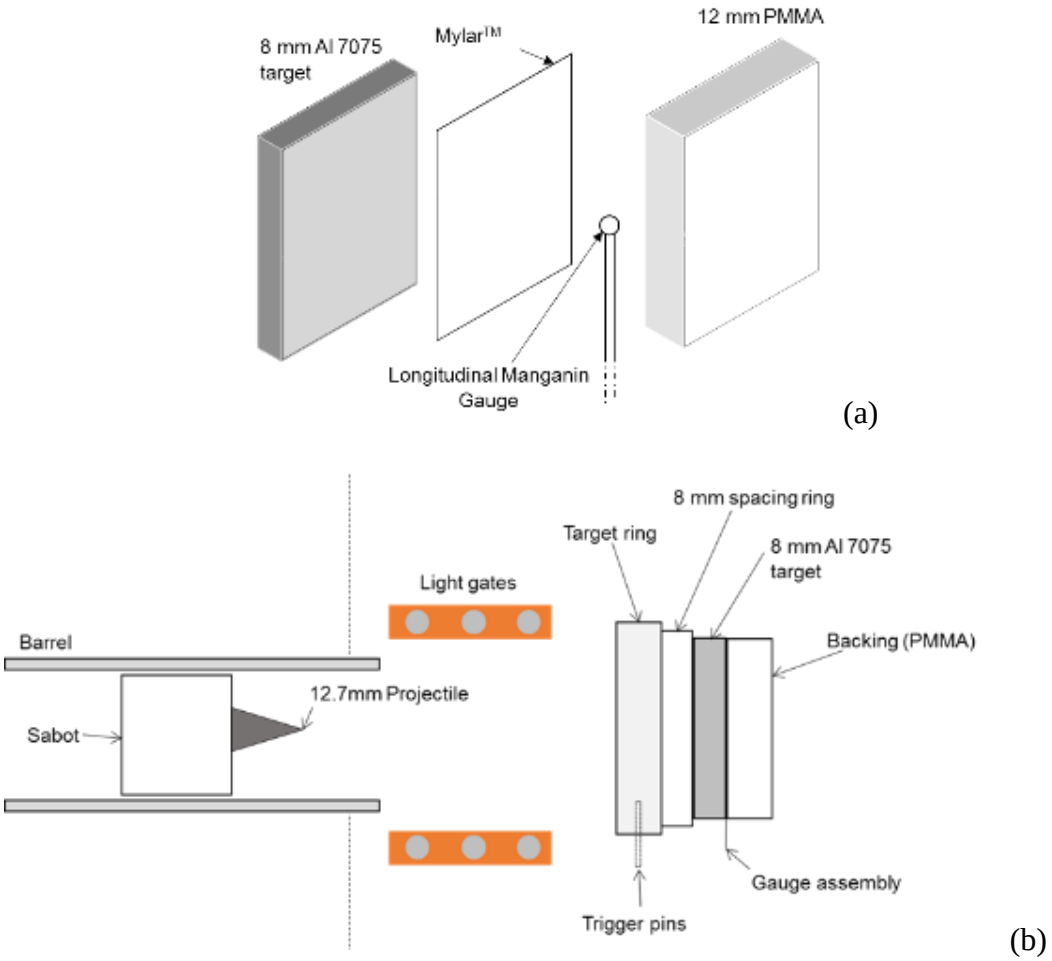

Figure 3.7 schematic ilustration of projectile-impact experiment using Manganin gauge (a) exploded view of target configuration; (b) experimental set-up for experiments.

Following assembly of the core elements of the arrangement a target set was assembled with an 8-mm aluminium spacing ring and a target ring containing a pair of trigger pins to initiate signal recording on an attatched oscilloscope. The aluminium spacing ring was included so that the sabot would initiate measurement when the tip of the projectile was ~2 mm away from the target, with the latter installed in a barrel extension and tightened with pins. The 12.7 mm En8 steel core projectile was inserted into a 50-mm diameter acetal sabot as shown in Figure 3.8 (a). The projectile was fired at 250 bar air pressure to reach a target velocity of 650 ± 20 m/s. Gauges were interpreted according to the Rosenberg et al. (65).

(a) Inserted unjacketed and jacketed cores in 50 mm acetal sabot.

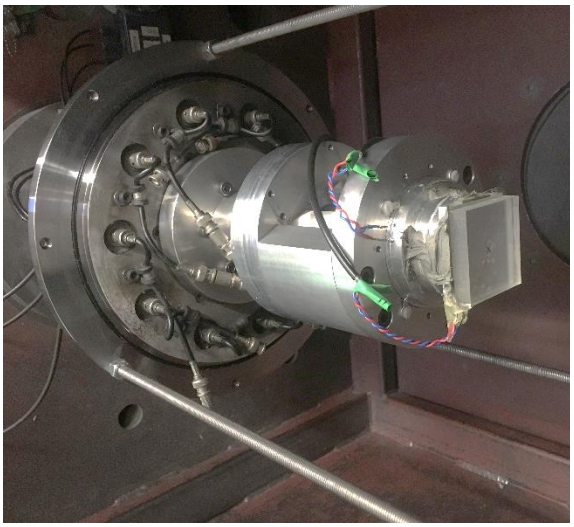

(b) A target set mounted to barrel extension on muzzle.

Figure 3.8 Pictures showing the main components of the reverse ballistic experimental arrangement.

In this experiment, aluminium 7075 was used as target instead of Armox Advance plate because it was readily available and easy to prepare to a good surface finish. Meanwhile, Armox Advance plate preparation took a long time to be finished. The PMMA backing was applied in this experiment because it was a less expensive material which was, never the less, well characterised. In addition, its clear surface facilitated the pressure gauge positioning.

The pressure gauge experiment presented pressure generated by projectile on PMMA surface. This presented a further explanation of the effect of copper jacket during penetration compared to forward and reverse ballistic. Moreover, the shock wave behaviour upon impact was clearly observed through pressure gauge traces. However, improper target set preparation and gauge calibration could affected the measurement result.

4 Modelling procedure

In this study, the commercial software ANSYS Explicit Dynamic and ANSYS Autodyn® have been applied to simulate the impact of steel projectiles and Armox Advance plates. Both programs are in ANSYS Workbench package version 18.1. ANSYS Explicit Dynamic is applied to build the model from an imported *.STEP format drawing file which was generated in Solidworks software as presented in Figure 4.1. Engineering data input and the model's meshing were carried out using Explicit Dynamic due to its accessibility and ability to provide parametrising inputs and outputs. Parametrising is quite useful when running multiple similar simulations and changing only a small part of parameters. In turn Autodyn® was used as a solver because its gives more control to the user.

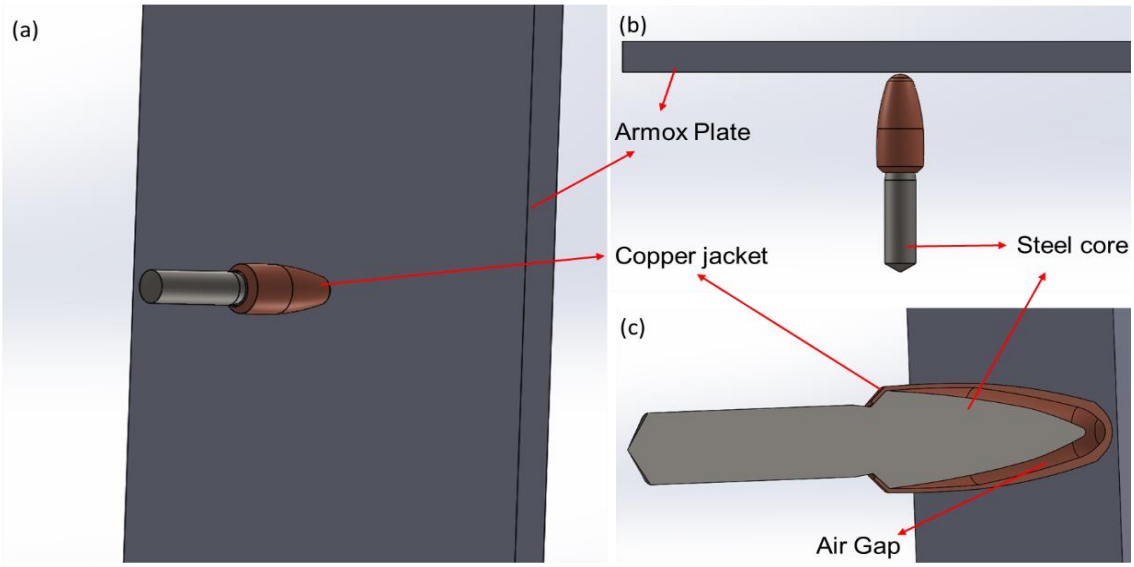

Figure 4.1 Projectile and target drawing in Solidworks; (a) overall view; (b) X-axis view and (c) cross-sectional view of projectile.

Three different part drawings were created for these models, namely that for the target plate (Armox Advance), steel core and copper jacket. There was an air gap between steel core and copper jacket as shown in Figure 4.1(c). Those

geometries were developed individually and then compiled as one assembly file before being exported to the requisite *.STEP file.

The Armox Advance steel targets of thicknesses 5 and 9 mm were modelled as three-dimensional deformable bodies on ANSYS Explicit dynamic. The size of the target was 150 mm x 150 mm. The projectiles were also modelled as three-dimensional deformable bodies of 12.7 mm armour piercing (AP) core. Those parts geometries were imported from the .STEP file and sliced to a half symmetry model in order to reduce the computational resources required during the simulation. The half symmetry model represented the same behaviour with a full three-dimensional model (55). In turn, the Armox plate was divided into two parts to allow set finer mesh size on a smaller part in the middle (close to the area of impact) and a coarser mesh on the rest of the structure in consideration of reducing nodes and elements.

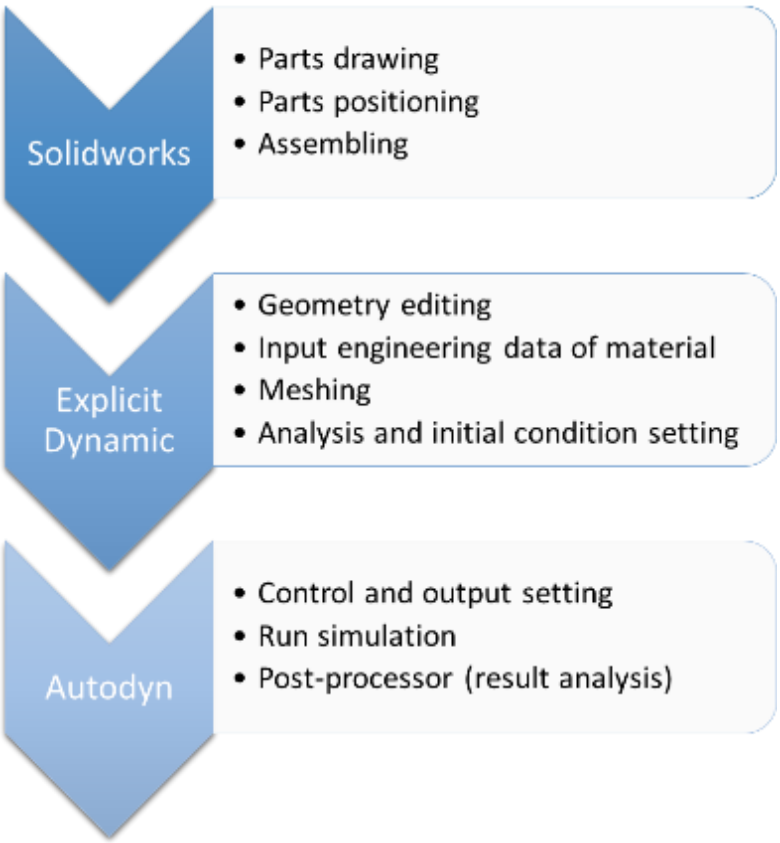

Figure 4.2 Numerical simulation works order.

Material properties of the Armox Advance steel target, steel core, and copper jacket were imported from the ANSYS library, with some parameters edited manually according to experimental results and references. The target was meshed using the multizone method and body sizing with element sizes of 0.5 and 1 mm respectively for the finer and coarser areas. Whereas, the copper jacket and the steel core were meshed by the patch independent method with an element size of 1 mm. The projectiles were impacted on the target at an incident velocity of 750 m/s. All the material properties used in the simulation are described in Table 4.1, 4.2 and 4.3.

Table 4.1 Material properties of Armox Advance.

Description	**Notation**	**Numerical value**
Modulus of elasticity	E (Pa)	2.19×10^{11}
Density	ρ (kg/m3)	7,783
Specific heat	Cp (J/kg.C)	550
Johnson Cook Strength		
Strain rate correction		First order
Initial yield stress	A (Pa)	1.58×10^{9}
Hardening constant	B (Pa)	9.58×10^{8}
Hardening exponent	*n*	0.175
Strain rate constant	*C*	0.00877
Thermal softening exponent	*m*	0.172
Melting temperature	θ_{melt} (K)	1,800
Reference strain rate	ε_0	$1\ s^{-1}$
Shear modulus	G (Pa)	
Shock EOS Linear		
Gruneisen coefficient	Γ	1.6
Parameter C1	C1 (m/s)	3,980
Parameter S1	S1	1.58
Parameter quadratic S2	S2 (s/m)	0
Principal stress failure		
Maximum tensile stress	(Pa)	2.25×10^{9}
Maximum shear stress	(Pa)	-

Table 4.2 Material properties of Copper.

Description	Notation	Numerical value
Modulus of elasticity	E (Pa)	1.23×10^{11}
Density	ρ (kg/m3)	8,900
Multilinear isotropic hardening		Tubular data from ANSYS library
Specific heat	Cp (J/kg.C)	1×10^{-12}
Shear modulus	G (Pa)	4.64×10^{10}
Shock EOS Linear		
Gruneisen coefficient	Γ	2
Parameter C1	C1 (m/s)	3,958
Parameter S1	S1	1.497
Parameter quadratic S2	S2 (s/m)	0
Geometric strain failure		1.5

Table 4.3 Material properties of M2 steel core.

Description	Notation	Numerical value
Modulus of elasticity	E (Pa)	2.29×10^{11}
Density	ρ (kg/m3)	8,100
Specific heat	Cp (J/kg.C)	598.33
Bilinear isotropic hardening		
Yield strength	Y (Pa)	2.46×10^{9}
Tangent modulus	E_t (Pa)	1.47×10^{11}
Shear modulus	G (Pa)	8.97×10^{10}
Shock EOS Linear		
Gruneisen coefficient	Γ	2.17
Parameter C1	C1 (m/s)	4,569
Parameter S1	S1	1.49
Parameter quadratic S2	S2 (s/m)	0
Principal stress failure		
Maximum tensile stress	(Pa)	2.46×10^{9}
Maximum shear stress	(Pa)	-

Different material properties were applied in these numerical simulations. All of the copper properties was loaded from the ANSYS materials library also with

selected engineering data for the M2 steel core and the Armox Advance plate. The M2 steel core properties are similar to those of S-7, while the Armox Advance steel plate has a similar strength to steel V250. In addition, key elastic properties (modulus of elasticity, tangent modulus and shear modulus) of both M2 steel and Armox Advance were determined ultrasonically by measuring longitudinal and shear wave velocities at 1.0 Mhz traveling within materials. In turn, material desnities were accurately measured via the Archamedes principle (Mettler Toledo Density Measurement Kit (Mettler Toledo) (66).

Table 4.4 shows details of the meshing methods applied to the parts. A multizone meshing method was used for the Armox Advance components before body sizing was applied to reduce element size. The multizone method automatically decomposes geometry into blocks which comprise of a dominant hexahedron mesh with the remaining region filled with unstructured hexahedron core or tetrahedron mesh elements. This method reduced the number of elements as well as simulation run time. Because of their complicated geometries, a patch independent method was employed for the copper jacket and steel core parts to generate tetrahedron elements. The patch independent method meshes volume first before face and edge meshing (67).

Table 4.4 Meshing of target plate and projectile.

Part	Meshing	Element type	Mesh quality
Armox Advance 1	Multi-zone (0.5 mm) and Body sizing (1mm)	Hexahedron	0.59471 - 0.91643
Armox Advance 2	Body sizing (4 mm)	Hexahedron and wedge	0.16462 - 0.78929
Steel core	Patch independent (1 mm)	Tetrahedron	0.43356 - 0.99609
Copper jacket	Patch independent (1 mm)	Tetrahedron	0.39419 - 0.99869

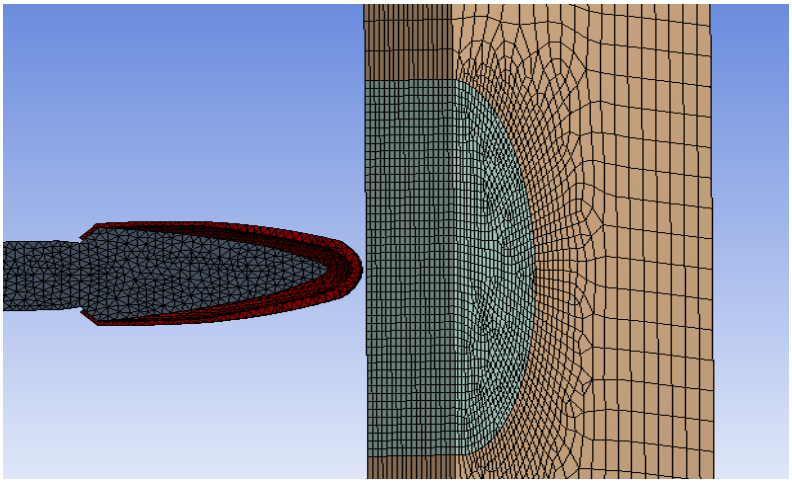

Figure 4.3 Projectile and target meshing in a half symmetry model.

An initial velocity applied to the moving parts (e.g. the copper jacket and steel core) of 750 m/s along z-axis. Fixed supports (e.g. constraints in terms of motion in all three planes) were then applied on both the top and bottom faces of the Armox Advance plate as shown in Figure 4.4 (b) to simulate the retention approach adopted experimentally (see figure 3.1). At this point the setup data was exported to Autodyn® and simulation end time, other control parameters and output files were arranged before running the simulation. Typically, output comprised of residual velocity, wave propagation pictures, and stress.

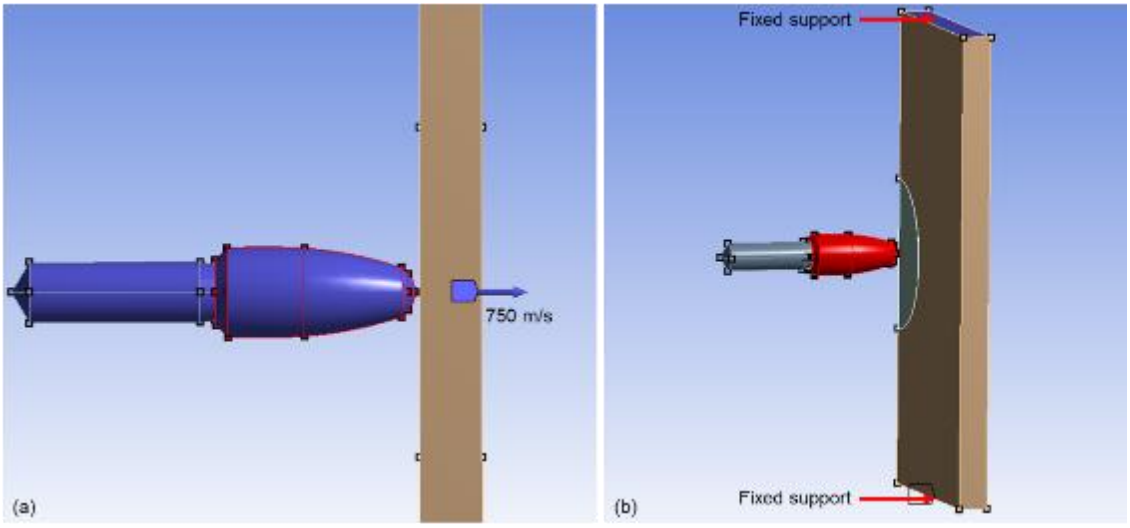

Figure 4.4 (a) initial velocity direction and (b) fixed supports position.

5 Result and discussion

This section outlines and discusses the results obtained from all experiments. Results from forward ballistic, reverse ballistic, stress gauge experiments and numerical simulations are all presented and discussed with the aim of highlighting the effects of differing projectile configurations on their ballistic response.

5.1 Material characteristics

Four core materials were employed for these experiments; two steels (En8 and M2 high speed steel (HSS)) for the bullet core; Armox Advance for the targets and C101 copper for the bullet jackets (where present). Hardness values for these different materials – and the different heat treatments employed – are detailed in Table 5.1.

Table 5.1 Hardness of materials

Materials	Average hardness value	
	Hardness Vickers (HV)	**Hardness Rockwell C (HRC)**
Copper Jacket	84.7	-
Armox Advance	677.0	59
En8 Steel	558.3	52.9
M2 HSS Steel 42	429.0	43.5
M2 HSS Steel 52	551.5	52.4
M2 HSS Steel 62	827.2	64.8

From Table 5.1 it is apparent that the copper material has the lowest hardness value, consistent with its ductile characteristic (something enhanced by annealing during production – as detailed in the next few sections). Whereas En8 steel has a similar hardness value with M2 HSS steel 42. The En8 steel core was used in initial sample in reverse ballistic tests. Interestingly, the Armox Advance plate

hardness is only surpassed by that of the M2 HSS steel 62. In this study, M2 HSS steel cores were prepared in three different hardness configurations as detailed in Table 5.1 (42, 52 and 62 HRC). Hardness was controlled via tempering temperature; decreasing temperature increased the amount of the harder martensitic phase, in turn reducing the proportion of the softer retained austenitic phase. More details on each of these materials are presented in the following sub-sections.

5.1.1 Bullet Materials

En8 steel and M2 high-speed steel (HSS) with various hardness conditions were used to produce steel cores to observe the influence of material and hardness on penetration performance. As discussed in Section 2.3, both steels were machined before heat treatment process. Figure 5.1 shows optical micrographs illustrating the microstructure of both En8 steel and M2 HSS steels with hardness targets of 42, 52 and 62 HRC.

In the En8 microstructure, blue crystals were observed representing martensite in an austenite matrix. Martensite is generated by rapid cooling after hardening from the austenite temperature. In turn, the M2 steel is observed to exhibit both martensite (blue crystals) and an additional phase comprising of a metal carbide (MC and M_6C types), as shown in Figure 5.1. It's also worth noting that a greater proportion of martensite was found in the higher hardness 62 HRC M2 steels compared to those with other hardness conditions.

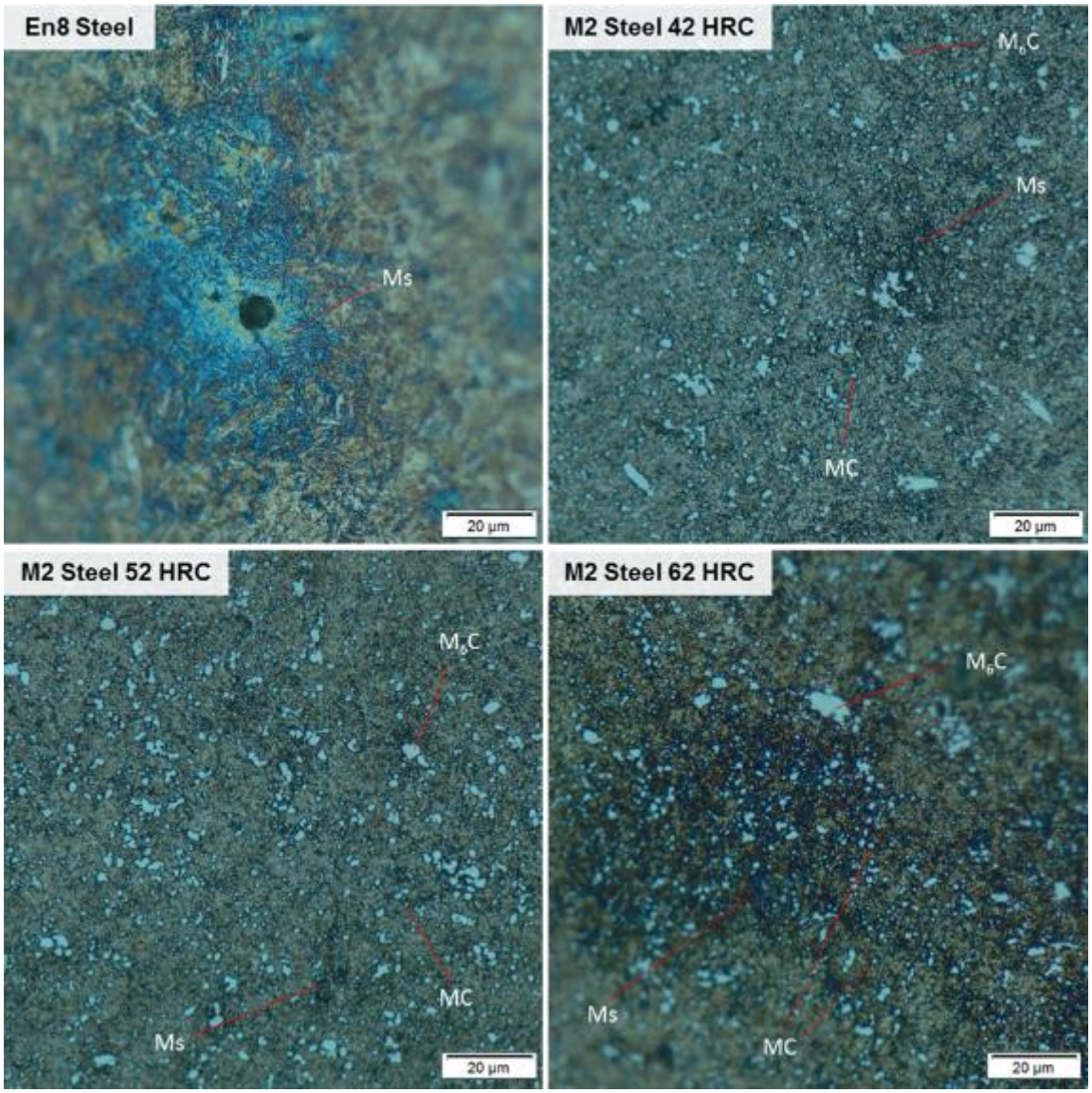

Figure 5.1 Microstructure of En8 steel and M2 steel in various hardness contains martensite and metal carbide in austenite matrix.

The micrographs presented in Figure 5.1 are consistent with the known properties of both materials; in particular:

- En8 steel is an unalloyed medium carbon steel grade with reasonable tensile strength. It is broadly used for applications which require better mechanical properties than mild steel. Usefully, En8 can be flame or induction hardened to produce a good surface hardness with moderate wear resistance.

- M2 High speed steels comprise a family of alloys mainly used for cutting tools. These steels contain a soft metallic matrix with hard ceramic particles that withstand wear. The high-speed steel term is a synthesis of the following two components. First, the alloys belong to the Fe–C–X multicomponent system, where X is a group of alloying elements encompassing Cr, W or Mo, V, and Co. Second, the alloys are defined by their capability to retain a high hardness level even when submitted to elevated temperatures as a result of cutting metals at high speed. The carbides are predominantly consist of the strong carbide formers V, W, Mo and Cr (68).

5.1.2 Target plate material

Armox Advance, employed as the target material for the experiments discussed in this thesis, is an engineered armour steel which hardness in the range 58 to 63 HRC whose preparation involves a rapid cooling (quench) (69). Figure 5.2 shows the microstructure of the Armox Advance plates employed here; martensite crystals are apparent distributed alongside ferrite in an austenite matrix.

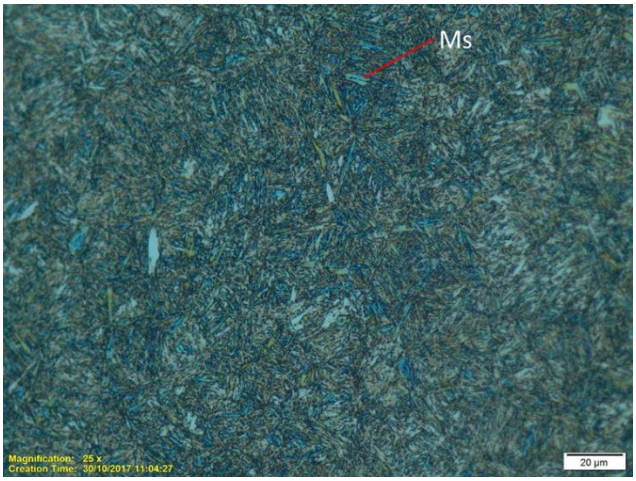

Figure 5.2 Microstructure of Armox Advance plate.

Bullet jackets were comprised of C101 copper (99%) sheets. During cupping, drawing and forming steps, the copper sheet was stretched leading to strain hardening. Consequently, an annealing process was employed in the forming steps to facilitate stress relaxation. This reduces hardness / increasing ductility – thereby enhancing formability and reducing the chance of resultant cracks). A typical resultant microstructure is shown in Figure 5.3 alongside the as-supplied material, showing large grains post-processing along with some residual twins from the cold drawing.

Figure 5.3 Microstructure of Copper C101 before and after annealing.

5.2 Forward-ballistics experiments

5.2.1 Residual velocity measurement

As detailed in Section 3.2, forward ballistic tests were employed to investigate the influence of both the jacket and projectile hardness on residual velocity of projectiles following perforation of a target plate. For these experiments, initial (post-muzzle) velocity was found to be relatively consistent and was measured as 741-794 m/s. Table 5.2 shows the measured residual velocity of projectile fragments after penetration for the experiments undertaken. The initial and residual velocities were measured using the PCC 2.7 (Phantom high-speed camera) software. Before velocity measurement, the system was calibrated by measuring the ruler's scale along the projectile flight path (x-axis). The residual velocities were measured by calculating the distance and the time difference of projectile fragments after leaving the target between two captured frames. In the residual velocity measurement, there were two potential errors that affected the measurement results. First, fragments may have been moving into or away from the screen (moving in the z-axis). Second, the measurement error caused by the apparent displacement of the projectiles because of a change in the high-speed camera's point of view. This phenomenon is called parallax. It is likely that these potential errors may have resulted in a lower measured residual velocity. Further, as discussed in section 2.3, the forward ballistic result may not be as comparable as it could be due to the different KE of the un-jacketed and jacketed projectiles. From all of the results, only the jacketed projectile with hardness 42 and 52 HRC were not able to penetrate the target. Thus, there was no residual velocity measured.

Table 5.2 Measured projectile fragments (residual) velocity.

M2 HSS Steel Core Hardness (HRC)	Residual velocity (m/s)			
	Unjacketed projectile		Jacketed Projectile	
	Armox 5 mm	Armox 9 mm	Armox 5 mm	Armox 9 mm
42	624	77	617	0
	614	147	611	0
	-	147	-	0
52	678	243	657	0
	697	274	678	0
	670	287	720	0
62	711	421	797	588
	736	446	721	553
	-	506	-	594

Figure 5.4 illustrates the influence of both projectile hardness and the jacket on projectile interaction with 5-mm thick Armox Advance targets. Several key elements fall out of this plot which highlights average residual fragment velocity post-penetration for the various projectile configurations considered.

As projectile hardness increases, residual velocity of fragments are also observed to increase. For the un-jacketed projectiles moving from a core hardness of 42 to 62 HRC leads to an increase in residual velocity of ca 17% - with an even more marked increase of ca 24% for the jacketed case. The higher is residual velocity, the lower is energy loss. Energy loss is not considered due to the erosion of the projectiles. Instead, we consider velocity drop either side of the target as an indicative measure of armour / projectile performance. This suggest two key things: (1) that (as might be expected) harder cores are more efficient at penetrating and; (2) that the jacket for the highest hardness cores considered clearly plays a role in maximising penetration efficiency (e.g. leading to a higher residual fragment velocity – although it's worth noting that for lower

hardness systems the different in projectile performance due to presence of the jacket is likely statistically insignificant).

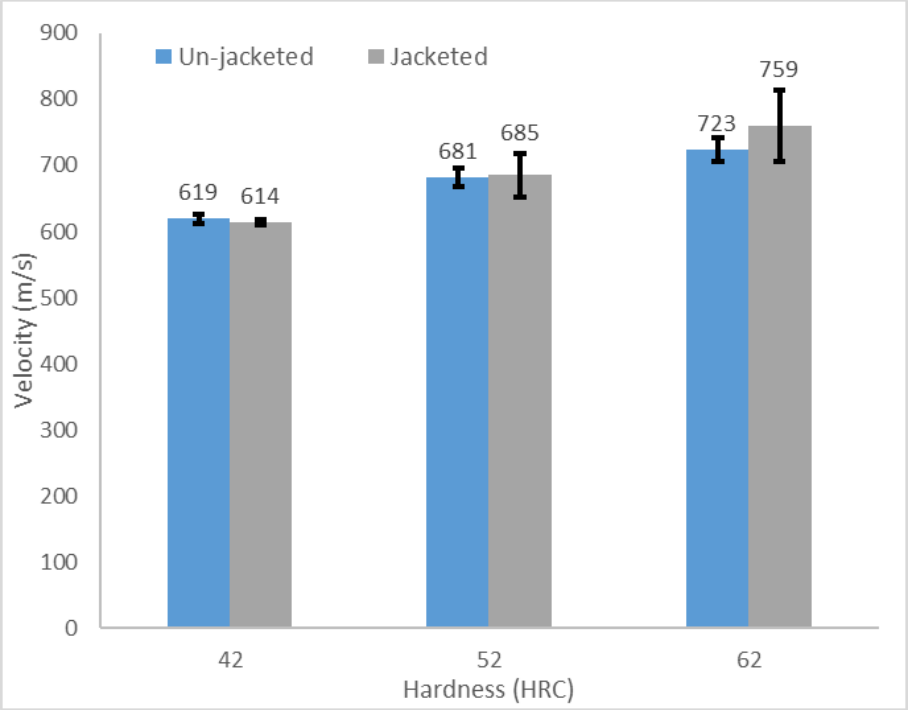

Figure 5.4 Average residual velocity of the un-jacketed and the jacketed projectiles after penetrating 5-mm thick Armox Advance plate.

As might be expected moving to a thicker target plate (9 rather than 5-mm thickness) led to a reduction in fragment residual velocity – as shown in Figure 5.5. Importantly, however, a clear enhanced penetration efficiency was apparent not only as core hardness increased, but also particularly where a jacketed round was employed for the 62 HRC case. However, at lower hardness (42 and 52 HRC), the presence of the copper jacket stopped the core's penetration.

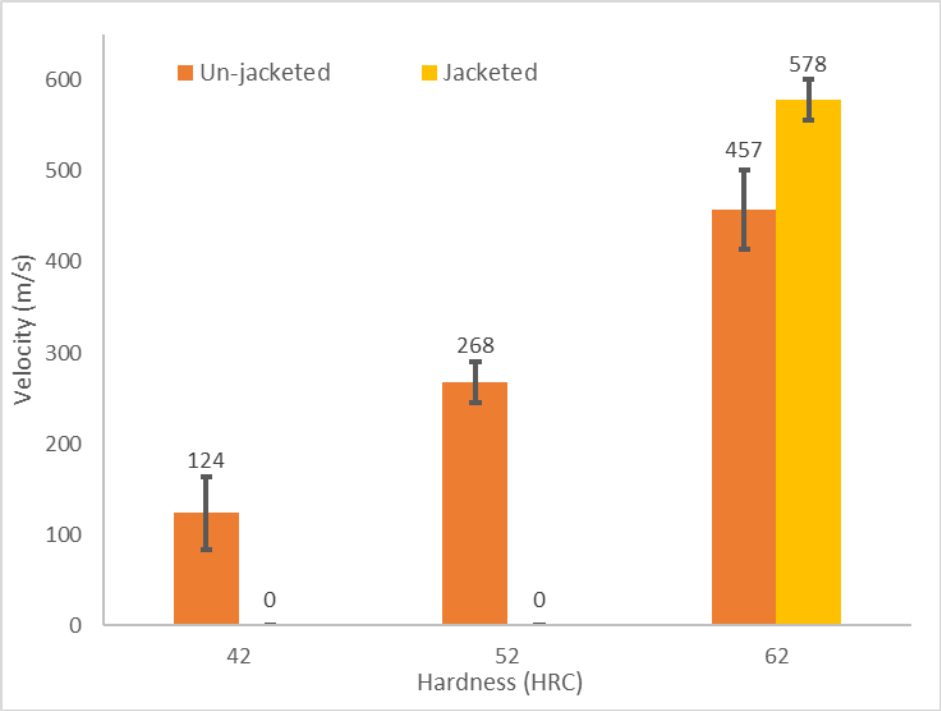

Figure 5.5 Average residual velocity of the un-jacketed and the jacketed projectiles after penetrating 9-mm thick Armox Advance plate.

Overall, the enhanced performance of rounds in the 62 HRC case in both Figure 5.4 and Figure 5.5 correlates with the fact that in these cases the projectile was harder – and therefore overmatched – the Armox plate with hardness 59 HRC (see Table 5.1). Whereas, the un-jacketed cores whose hardness's were lower than the Armox plate were more penetrative compared with the jacketed cores with the same hardness. While there is an argument that the jacket may be both cushioning and confining the core, the importance of projectile hardness suggests that a cushioning effect (e.g. protection of the harder core on impact) may be of particular importance.

5.2.2 Recovered projectiles and targets

Both projectiles and targets (in both cases either complete or fragments) were collected post experiments to help provide a more detailed explanation about the penetration mechanisms in operation as well as those governing both projectile and target failure. Figure 5.6 and Figure 5.7 show representative photos of similar rounds fired in forward ballistic experiments.

Both the (potentially fragmented) projectiles and the 5-mm Armox Advance targets, post experiments, are shown in figure 5.6. These refers to experiments 1 to 12 in Table 5.3. All projectiles penetrated and perforated the targets. It was also observed that the un-jacketed projectile perforated the target either by plugging or adiabatic shear failure as indicated by red arrow in Figure 5.6. However, a different failure mechanism was observed in the jacketed projectile penetration. Interestingly, the jacketed projectiles created a bigger hole on the targets. For example, the 62 HRC un-jacketed projectile impact produced a hole with a peak width at the widest point of 22.97 mm; whereas the same hardness projectile covered with copper jacket resulted in a comparatively bigger penetration hole, with a maximum diameter of 37.89 mm. It is postulated that this difference – attributable to the presence of the copper jacket – arise due to the jacket's ductile nature which would have absorbed energy on impact via elastic / -plastic deformation, protecting the core and also – potentially – pre-stressing (due to the high impedance of copper) the target plate.

Figure 5.6 Recovered fragments of projectiles and 5-mm target plates, (a) to (c) un-jacketed projectiles; (d) to (f) jacketed projectiles.

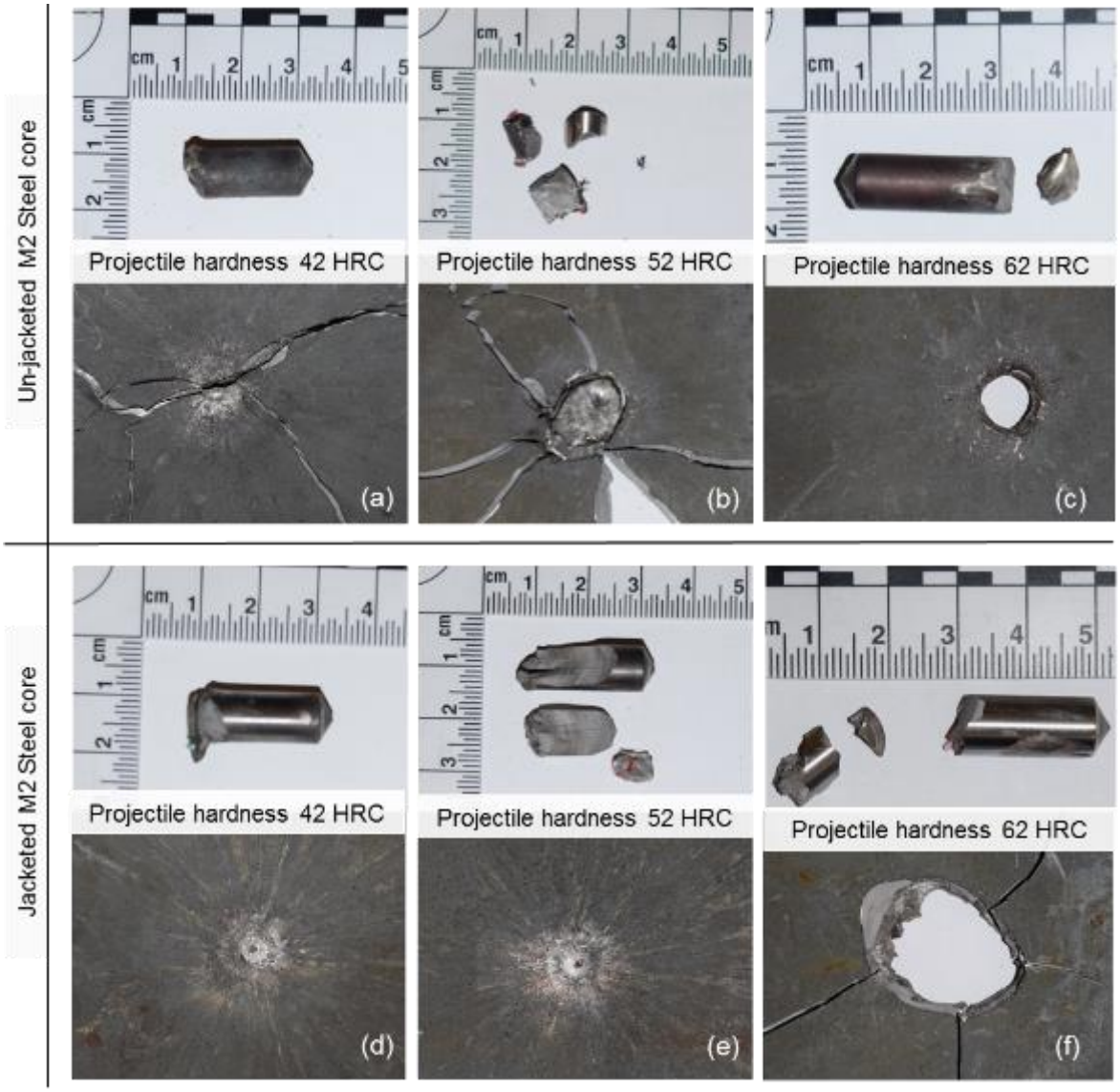

Figure 5.7 Recovered fragments of projectiles and 9-mm target plates, (a) to (c) un-jacketed projectiles; (d) to (f) jacketed projectiles.

In contrast, the un-jacketed and the jacketed projectiles impacts onto 9-mm thick targets showed some different results. In particular:

1) The un-jacketed projectiles having 42 and 52 HRC hardness were able to break the target. This is illustrated in Figure 5.7 (a) and (b) which show that the projectile fractured the target with cracks radiating from the point of impact. This cracking appears to have been initiated by the projectile's sharp tip impact before it eroded.

2) For jacketed projectiles having 42 and 52 HRC, different behaviour was noticed with no obvious damage or cracking of target plates. (see Figure 5.7 (d) and (e)). In this case, the 42 and 52 HRC jacketed projectiles simply indented the target surface. It was observed that the indentation size and depth increased with the hardness.
3) A similar penetration behaviour for jacketed and unjacketed impactors was apparent for the 62 HRC projectiles. The figure 5.7 (c) clearly shows that the 62 HRC un-jacketed projectile perforated the target by plugging but this damage to the target occurred without causing any additional fracture around the vicinity of perforation. However, jacketed round catastrophically defeated the target as shown in Figure 5.7 (f).

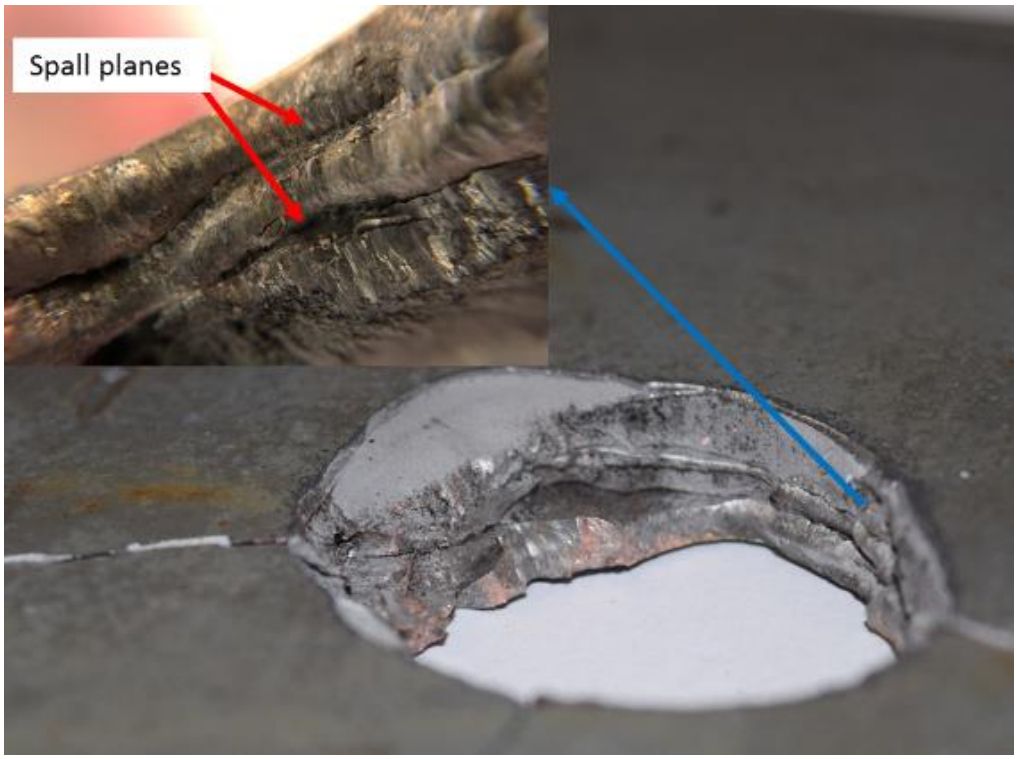

Figure 5.8 Spall plane on the Armox Advance target plate after penetration by the 62 HRC jacketed projectile.

The penetration of the 62 HRC jacketed projectile on the target also resulted in spall planes as shown in Figure 5.8. These spall planes were caused by reflected wave collisions within the target. The shock wave reflected back and propagated

within the steel core-copper jacket body and target plate. This reflected wave then generated a spall failure when the reflected wave from the rear surface of projectile and target collide (3, 57).

A summary of the complete set of forward ballistic experiments conducted is presented in Table 5.3. These results provide further insight into the penetration behaviour of the un-jacketed and the jacketed projectiles on the 5-mm and 9-mm targets discussed above / shown in Figure 5.6 to Figure 5.8.

Table 5.3 Forward ballistic result for all projectile and targets.

No	Experiments [a]	Target failure			Core's Hardness > Armox's Hardness
		Fragmented	Perforated	Indented	
1	42 UJ - A5	√	√	-	No
2	42 J - A5	√	√	-	No
3	52 UJ - A5	√	√	-	No
4	52 J - A5	√	√	-	No
5	62 UJ - A5	√	√	-	Yes
6	62 J - A5	√	√	-	Yes
7	42 UJ - A9	√	√	-	No
8	42 J - A9	-	-	√	No
9	52 UJ - A9	√	√	-	No
10	52 J - A9	-	-	√	No
11	62 UJ - A9	-	√	-	Yes
12	62 J - A9	√	√	-	Yes

[a] UJ = un-jacketed projectile; J = jacketed projectile; 42, 52, 62 = projectile hardness; A5 = Armox Advance 5-mm thick; A9 = Armox Advance 9-mm thick.

Overall from Table 5.3, as well as the residual velocity data presented in Figure 5.4, it is apparent that in the 5-mm target case for penetration by both jacketed and unjacketed projectiles, that an increase in hardness and / or the presence of the copper jacket has minimal effect for the lower two hardness values considered. As discussed in previous section there is some effect / different in performance at 62 HRC – however this is relatively minimal.

On the other hand, in the 9-mm target penetration by the projectiles, it is immediately apparent from both Table 5.3 and Figure 5.5 that projectiles need to be harder to perforate the target. When the projectiles hardness is higher than the target hardness, the copper jacket leads to extra damage upon impact. Whilst, when the target is harder than the projectiles the use of an un-jacketed projectile is observed to result in the target becoming fragmented. In contrast, under otherwise identical impact conditions, the use of a jacketed projectile results in indentation on the target surface without any fragmentation.

In addition to visual analysis of impacted targets, the recovered projectile fragment lengths were also measured with the aim of investigating the effect of hardness and the presence (or otherwise) of the copper jacket on the (projectile) core. Figure 5.9 shows the total length of cores which were recovered intact after impacting the various target plates. Considering the un-jacketed and jacketed cases separately:

- **Un-jacketed case:** as shown in Figure 5.9, the intact core length of the un-jacketed core increased from 30.69 mm for the softest core to 36.14 mm at the 52 HRC condition and then decreased again to 32.07 mm for 62 HRC condition. Overall, it is apparent that the projectile hardness was having relatively little effect on core erosion when a jacket was not present. This therefore implies that another phenomenon – e.g. shattering / spallation of the core – may have been dominant.
- **Jacketed case:** in contrast to the un-jacketed case, a small but consistent increase in intact (recovered) core length with projectile hardness is apparent in Figure 5.9. This, in line with the discussion following Figure 5.4 and Figure 5.5, appears to suggest enhanced protection of the core by the jacket leading to increased penetration at higher velocities as core erosion is reduced (e.g. Figure 5.9).

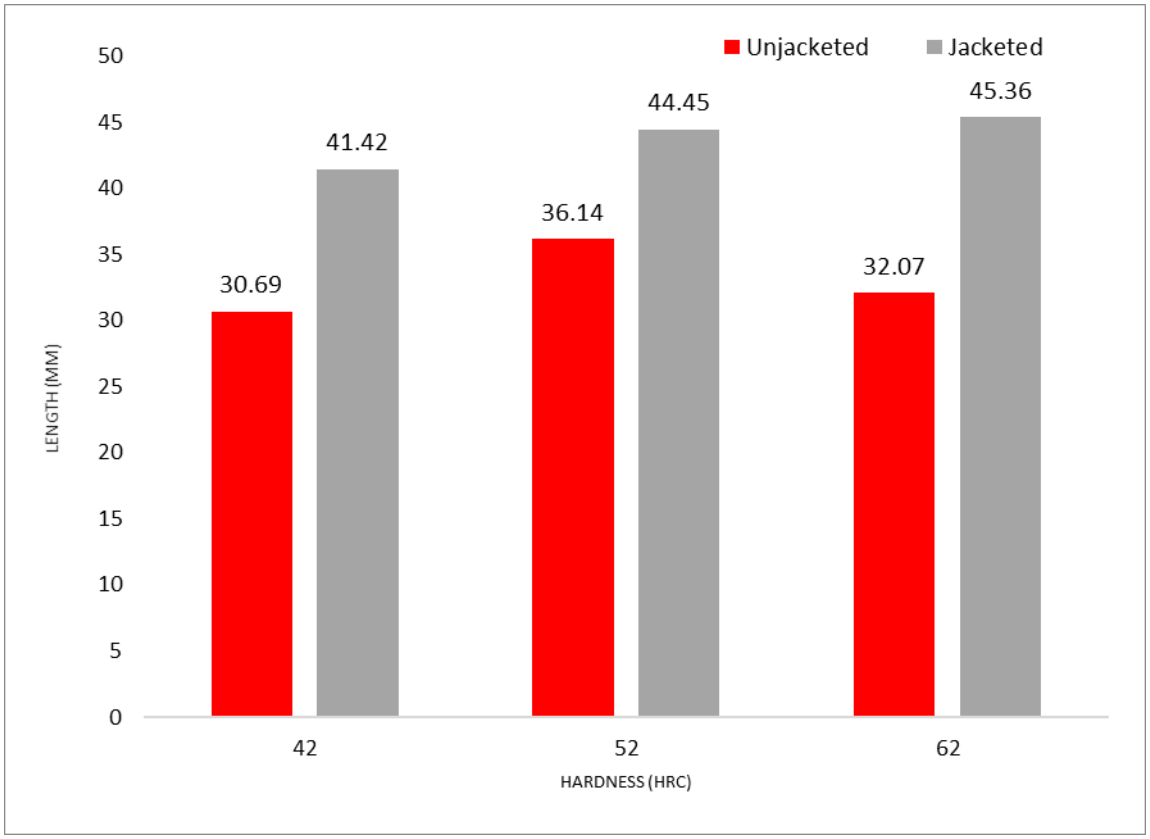

Figure 5.9 Recovered projectiles (un-jacketed and jacketed) after impacting the 5-mm thick Armox Advance target plate.

In contrast to the results for the 5-mm thick Armox Advance plate in Figure 5.9, for the 9-mm thick case, as shown in Figure 5.10, a lot more variability is apparent. While the presence of a jacket again appears to enhance ballistic response of the projectiles (e.g. longer intact cores are recovered) having 42 and 52 HRC, this was not reflected in the higher (62 HRC) hardness projectiles. The response of un-jacketed projectiles suggest that the higher thickness of steel target is now dominating ballistic behaviour and masking the contribution of the core hardness and jacket that was much clearer in the case of 5-mm thick plate as shown in Figure 5.9.

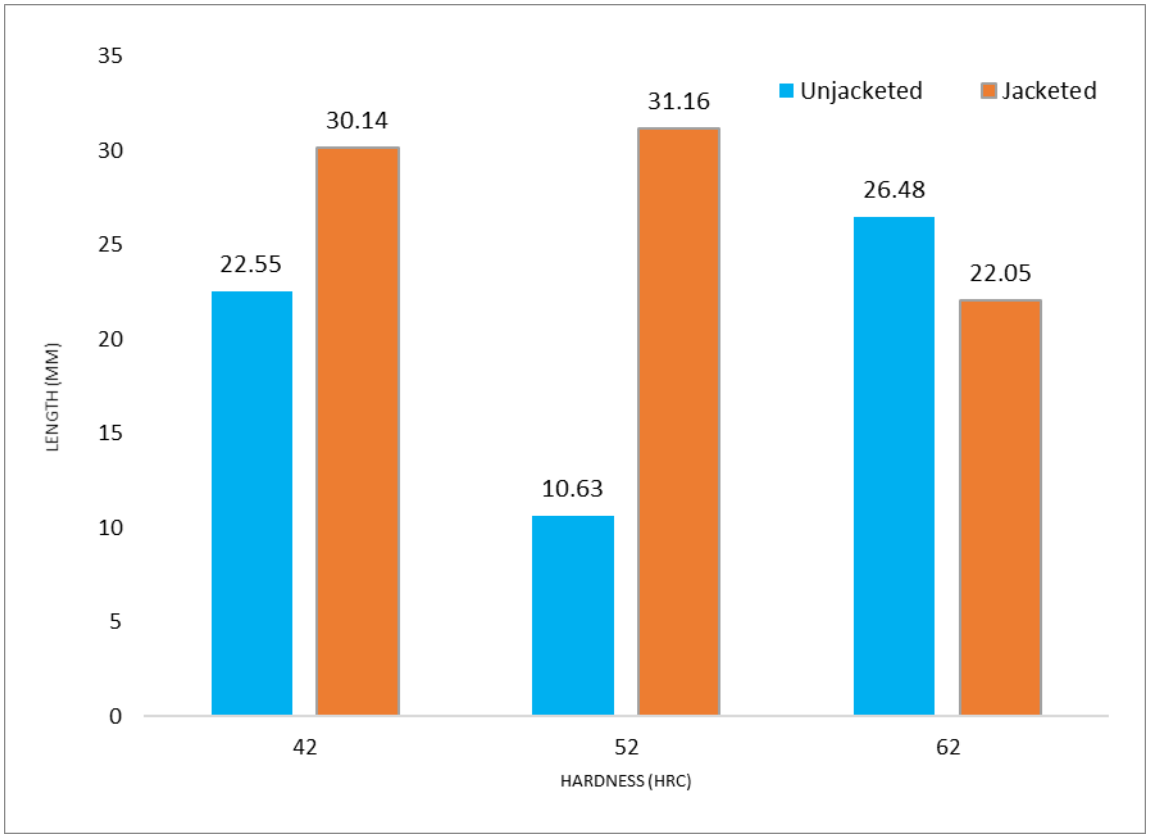

Figure 5.10 Recovered projectiles (un-jacketed and jacketed) after impacting the 9-mm thick Armox Advance target plate.

In line with the variation in data highlighted above in Figure 5.10, it is worth noting that in the forward ballistic experiments it was more difficult to collect all the projectile fragments, which were formed following the perforation event. Essentially, enhanced physical separation of the target and fragment collecting area in this forward ballistic test configuration (as opposed to the more compact reverse ballistic tests) meant that the projectile elements leaving the target often impacted either the target tank / tunnel frame or target supports. This resulted in further particulation and consequently smaller proportion of fragments were recoverable when compared to the projectile fragments observed in the associated high-speed camera footage. As an example of this phenomenon, Figure 5.11 shows the difference in fragment scale for a 62 HRC jacketed core observed perforating a 9-mm thick plate using a high-speed camera compared to the physically recovered fragments collected after the shot.

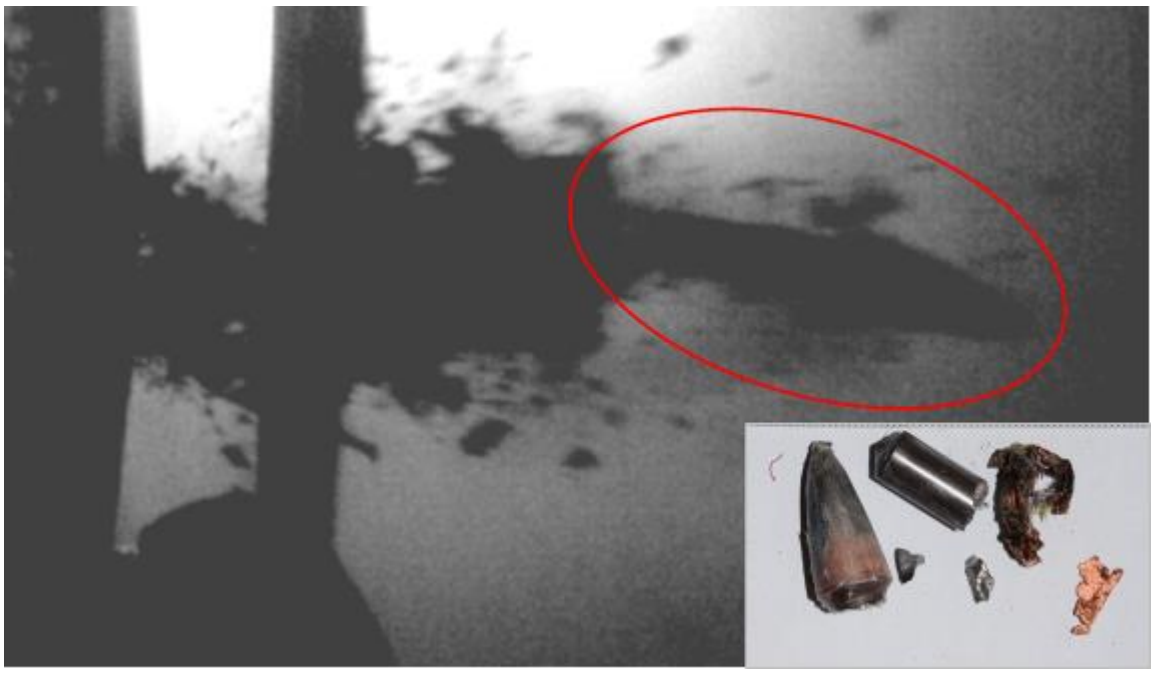

Figure 5.11 The 62 HRC jacketed core fragments observed in high-speed camera and collected post experiment.

Usefully, reverse ballistic experiments did not encounter the same experimental challenges detailed above. To this end, further observation of the effect of both the presence of a copper jacket and projectile hardness on penetration mechanism and projectile fragments formation / behaviour were made by conducting reverse ballistic tests. The reverse ballistic test also eliminated the projectile's yaw and ensured that impact occurs at a precise spatial point.

5.3 Reverse-ballistics experiments

5.3.1 En8 steel cores

5.3.1.1 X-Ray images

In order to provide further information with regards to the influence of the bullet jacket on penetration a series of four reverse ballistic experiments were carried out for the En8 steel cores bullets. The En8 steel cores were applied as initial

experiments before M2 steel cores test in three-hardness condition. These employed a standard En8 core of nominally 26 $\pm$ 2 g both with and without a crimped copper jacket (adhered in line with the approach detailed previously in Section 2.1) as required. This reverse ballistic test used 1 sample for each characteristic compared to forward ballistic which used 2 to 3 samples. Key experimental data for these tests is presented in Table 5.4.

Table 5.4 Key experimental data.

Exp. no.	Thickness of impactor (mm)	Impact velocity (m/s)	Jacket present
1	5.02	763	No
2	5.01	763	Yes
3	9.06	733	No
4	9.06	733	Yes

As detailed in Section 3.3 / Figure 3.4, flash X-rays were captured for all experiments. These are presented, with the time-base normalised nominally to the point of impact, for the 5-mm thick impactor case in Figure 5.12. Both un-jacketed and jacketed cores penetrated 5-mm thick Armox Advance perfectly. However, X-ray images at 10 μs show different behaviour for the core during penetration. A red-circled area in Figure 5.12 (a) shows that the unjacketed core started to erode at this point, with debris visible along the surface of the impactor. This behaviour is attributed to the lower hardness of the core as opposed to the Armox Advance plate. In contrast, the copper jacket present for the core in Figure 5.12 (b) appears to provide enhanced protection. Essentially, the presence of this jacket appears to protect the core's tip from damage and let the core continue to penetrate the plate beyond a comparable point post-impact for the case where no jacket was included. This behaviour is highlighted in the blue-dashed-circled area in Figure 5.12 (b); further, comparing Figures 5.12 (a) and (b) at 30 μs, it is immediately apparent that more damage has been done to the impactor plate in the jacketed case in Figure 5.12 (b). Overall, both cores penetrated the 5-mm plates and led to the formation of a number of both core and impactor fragments.

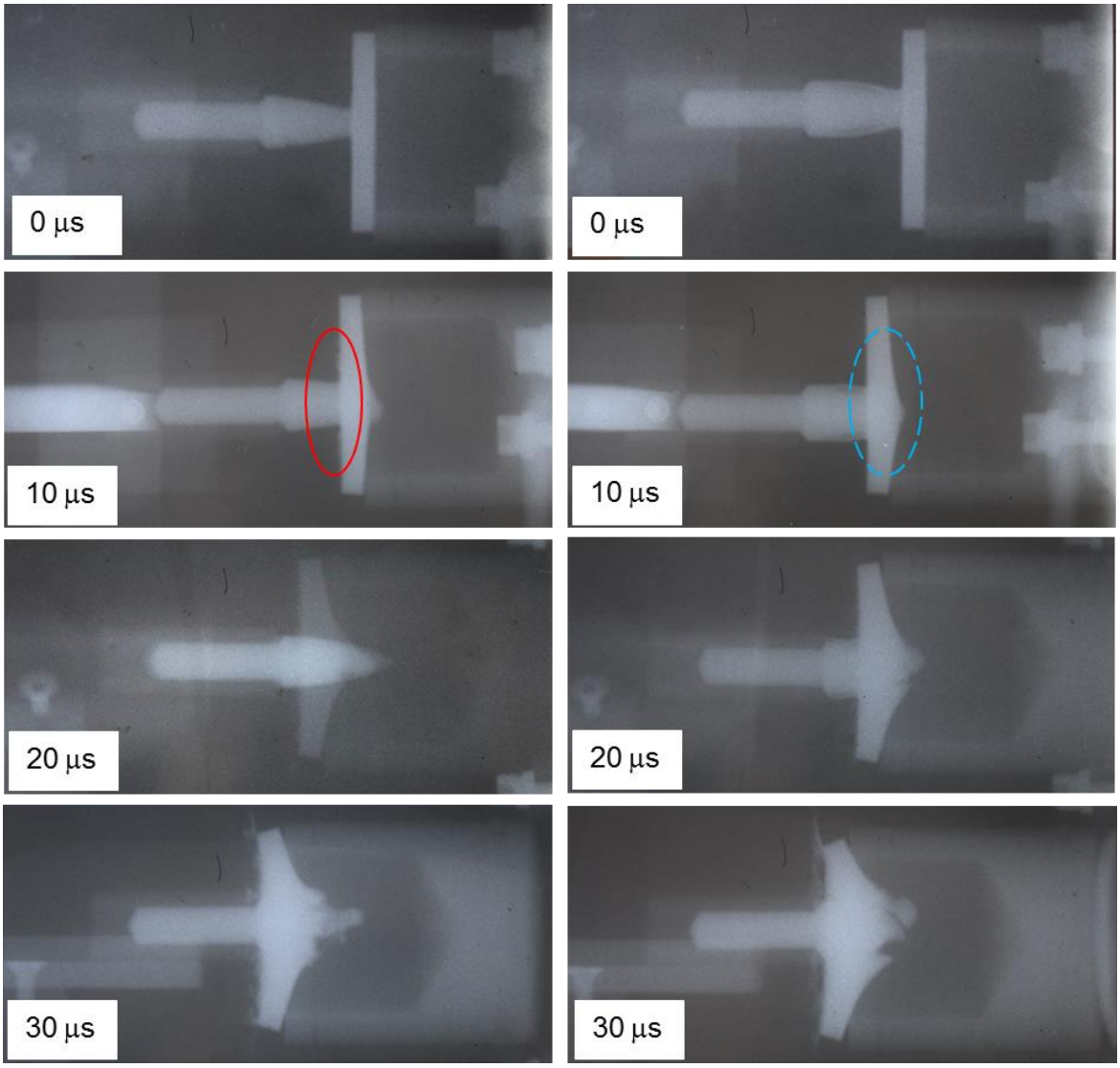

(a) un-jacketed core – exp. no. 1 (b) jacketed core – exp. no. 2

Figure 5.12 Flash X-rays showing impact of a 5-mm thick Armox Advance steel plate onto pre-positioned En8 steel AP cores (experiments no. 1 and 2 from Table 2).

As shown in Figure 5.13, the use of 9-mm rather than 5-mm thick impactors led to an even clearer picture of the cores behaviour during impact as the greater thickness enhanced the interaction time / also allowed the impactor to avoid catastrophic failure.

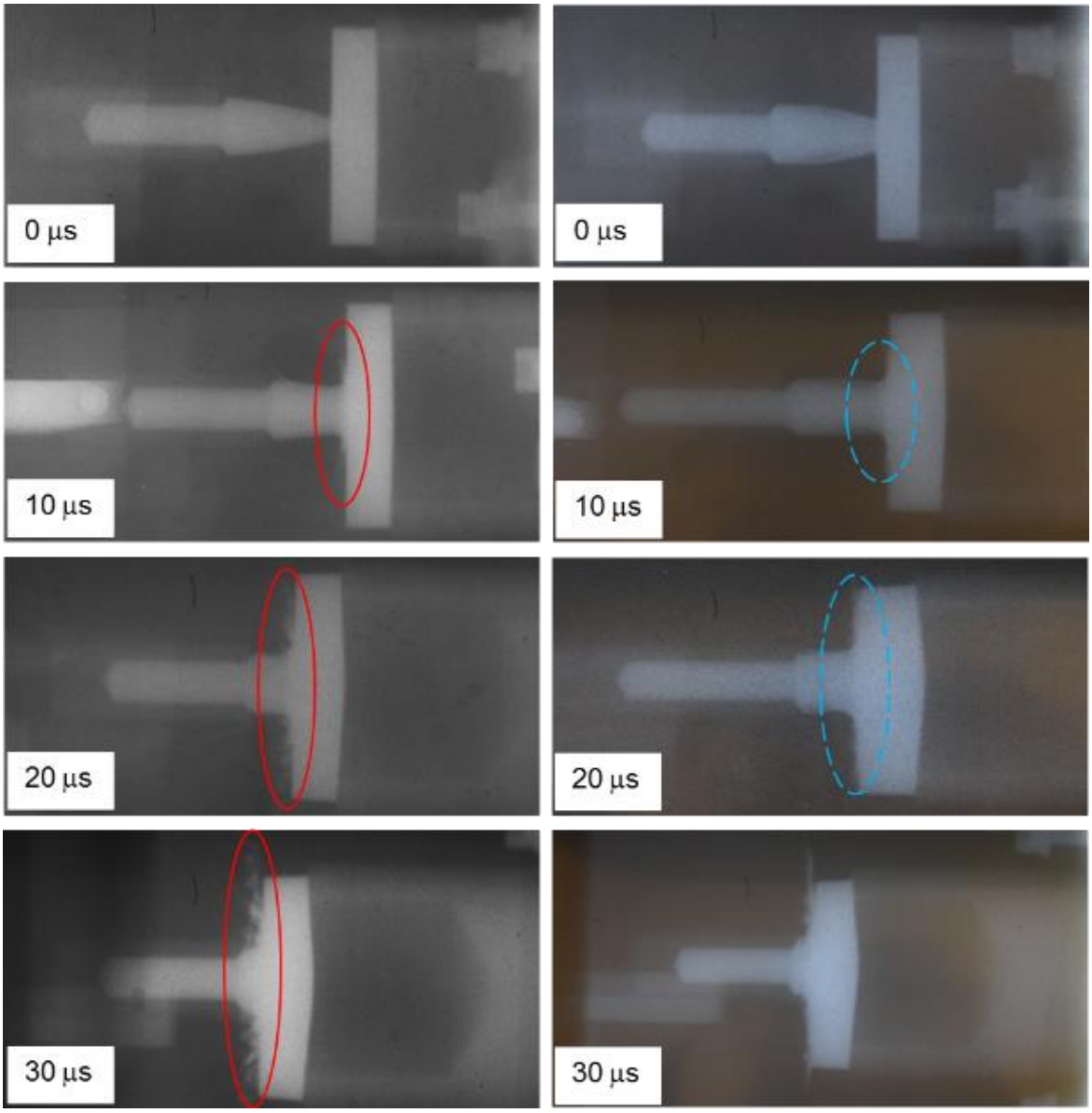

(a) un-jacketed core – exp. no. 3 (b) jacketed core – exp. no. 4.

Figure 5.13 Flash X-rays showing impact of a 9-mm thick Armox Advance steel plate onto pre-positioned AP cores (experiments no. 3 and 4 from Table 5.4).

From red-circled area in Figure 5.13 it is apparent that the un-jacketed core's failure started at nominally 10 μs after impact with some radial flow of the core visible; whereas in the jacketed case in Figure 5.13 (b), copper jacket deformation occurs before the core impacts the plate – evidenced by a conical interaction

zone between the jacket and impactor plate at this point highlighted by blue-dashed-circled area. Further contact with the impactor plate for the un-jacketed case results in continued failure of the core. This is illustrated by the flow of fragments around the point of impact / the corresponding red-circled area at 20 and 30 μs in Figure 5.13 (a) which show that the impact generates a large number of small core fragments. In comparison, the red-circled area at 20 μs in Figure 5.13 (b) indicates that the jacketed core shows relatively little damage with only copper jacket 'splash' on the 9-mm thick impactor plate surface observable. Furthermore, it is apparent that the jacketed core only begins to flow on the surface of the 'impactor' at around 30 μs. Comparing Figure 5.13 (a) and (b), it is clear that at this 30 μs mark the presence of a copper jacket leads to a much finer (both in size and dispersion) degree of eroded material moving radially away from the point of impact. This behaviour, indicative of a more efficient penetration, is in line with the observations made at a similar time post-impact for the 5-mm plate impact shown in Figure 5.12.

Overall, for the En8 steel-based bullets the copper jacket appears to give an intrinsic protection to the core – via a combination of confinement and cushioning (with the ductile copper preventing excessive loading on impact) such that the (shielded) core remains intact for longer than in the unjacketed case. Consequently, the core in the jacketed case has a higher energy density on impact and a greater penetrability.

5.3.1.2 Recovered projectiles and target plates fragments

As detailed in the section presented above, reverse ballistic testing resulted in clear (X-ray) images of both (stationary) 'projectile' and 'impactor' (accelerated target) behaviour during the impact / penetration process. To provide further insight into the influence of the copper jacket effect on penetration, both impactors and the associated cores were also recovery and investigated after each experiment. Figure 5.14 shows the recovered core and impactor fragments for the 5-mm thick Armox Advance plate cases from Table 5.4, with material for the corresponding 9-mm thick impactor cases shown in Figure 5.15.

Figure 5.14 Recovered impactors (5-mm thick Armox Advance) and En8 steel cores: (a) and (b) un-jacketed core shots and; (c) and (d) jacketed core shots from Table 5.4.

(a) Un-jacketed core (b) Jacketed core

Figure 5.15. Impactors (9-mm thick Armox Advance) and En8 steel cores after impact (Table 5.4).

Based on the recovered material shown in Figures 5.14 and 5.15, Table 5.5 presents reduced data illustrating the quantity and size of recovered fragments / core material. Based on this information a number of observations can be made:

1) For the 5-mm core case the jacketed En8 steel core and plate impacts resulted in more fragments compared with the unjacketed case (10 fragments above 0.8 grams versus 7 fragments respectively).
2) As shown in Figure 5.15, both the unjacketed and jacketed En8 steel core were not able to perforate the 9-mm thick Armox Advance impactors. However, from the impactor plate's surface, it is apparent that the jacketed core's impact created a bigger crater than for the unjacketed case.
3) In terms of recovered core length, for both impactor plate thicknesses, the presence of a jacket reduced the degree of projectile erosion (thereby enhancing penetrability). Interestingly, for both impactor plate thicknesses, the jacket appeared to reduce core erosion by around 2.5% (overall erosion was, unsurprisingly, greater for the thicker 9 mm plates). This appears to tentatively suggest a quantitative bound on the contribution of the jacket under these conditions to core protection / penetration.

Table 5.5. Steel core (initial length 55.31 mm) and impactor recovery after impact.

Experiment no. (see Table 2)	Thickness of impactor (mm)	Jacket present	No. of impactor fragments (> 0.8 g)	Remaining core length (mm)	Percentage reduction in core length (%)
1	5.02	No	7	45.50	17.74
2	5.01	Yes	10	46.90	15.21
3	9.06	No	- intact -	27.64	50.03
4	9.06	Yes	- intact -	28.96	47.64

A consistent trend in the results of jacketed and unjacketed En8 steel core impacts can be observed in the reverse ballistic shots for both 5 and 9 mm

impactors. Essentially, for both impactor thicknesses considered the lack of a jacket led to enhanced erosion / reduction in recovered core length. This is consistent with the observations from the captured flash X-rays as well as the results from the forwards ballistic experiments discussed previously in Section 5.2.

5.3.2 M2 Steel cores

As detailed previously in Section 2.1 high-speed molybdenum-based steel (M2) was also investigated as a potential core material via reverse ballistic testing. The aim of these experiments was to assess the influence of projectile hardness on performance against high hardness steel armour (Armox Advance). Whereas the results presented in Section 5.3.1, detailed the influence of the jacket on as-manufactured / supplied En8 steel cores, which are a medium carbon steel, here three different core hardness values were employed. In addition, in-line with its importance, these experiments were also designed to provide additional reinforcement of the previous findings with regards to the influence of the copper jacket on projectile / target interaction.

5.3.2.1 X-Ray images

A series of twelve reverse ballistic experiments were carried out using M2 high speed steel core with and without a crimped copper jacket. The same method explained in section 3.3 was employed in these shots. For each shot, four X-Ray images were captured. Table 5.6 highlights key experimental data for these tests – with dashed lines delaminating the different core hardness's employed.

Table 5.6 Key experimental data.

Exp. no.	Thickness of impactor (mm)	Projectile hardness (HRC)	Impact velocity (m/s)	Jacket present
1	5.01	42	778	No
2	5.01	42	763	Yes
3	5.00	52	778	No
4	5.00	52	778	Yes
5	5.00	62	763	No
6	5.00	62	763	Yes
7	9.06	42	763	No
8	9.06	42	718	Yes
9	9.07	52	747	No
10	9.06	52	747	Yes
11	9.04	62	763	No
12	9.07	62	763	Yes

For the experiments detailed in Table 5.6 both the un-jacketed and jacketed projectile were able to fully penetrate (perforate) the 5-mm thick Armox Advance plate in all cases. However, for the 9-mm thick targets only the un-jacketed and jacketed projectile with a hardness of 62 HRC were able to perforate the impactor / target. The other projectiles only indented the target surface and were eroded. It is clear that the un-jacketed and jacketed projectiles need to be harder to be able to penetrate the targets. Figure 5.16 (a) shows flash X-ray images of an M2 steel 42 HRC projectile impacting a 5-mm thick target in 10 μs intervals. From those pictures it can be observed that the head of the un-jacketed projectile was largely eroded before failure of the 5-mm impactor. Whereas for the corresponding jacketed projectile case in Figure 5.16 (b), less debris is observed and as clearly shown at 30 μs the core largely survived the penetration process.

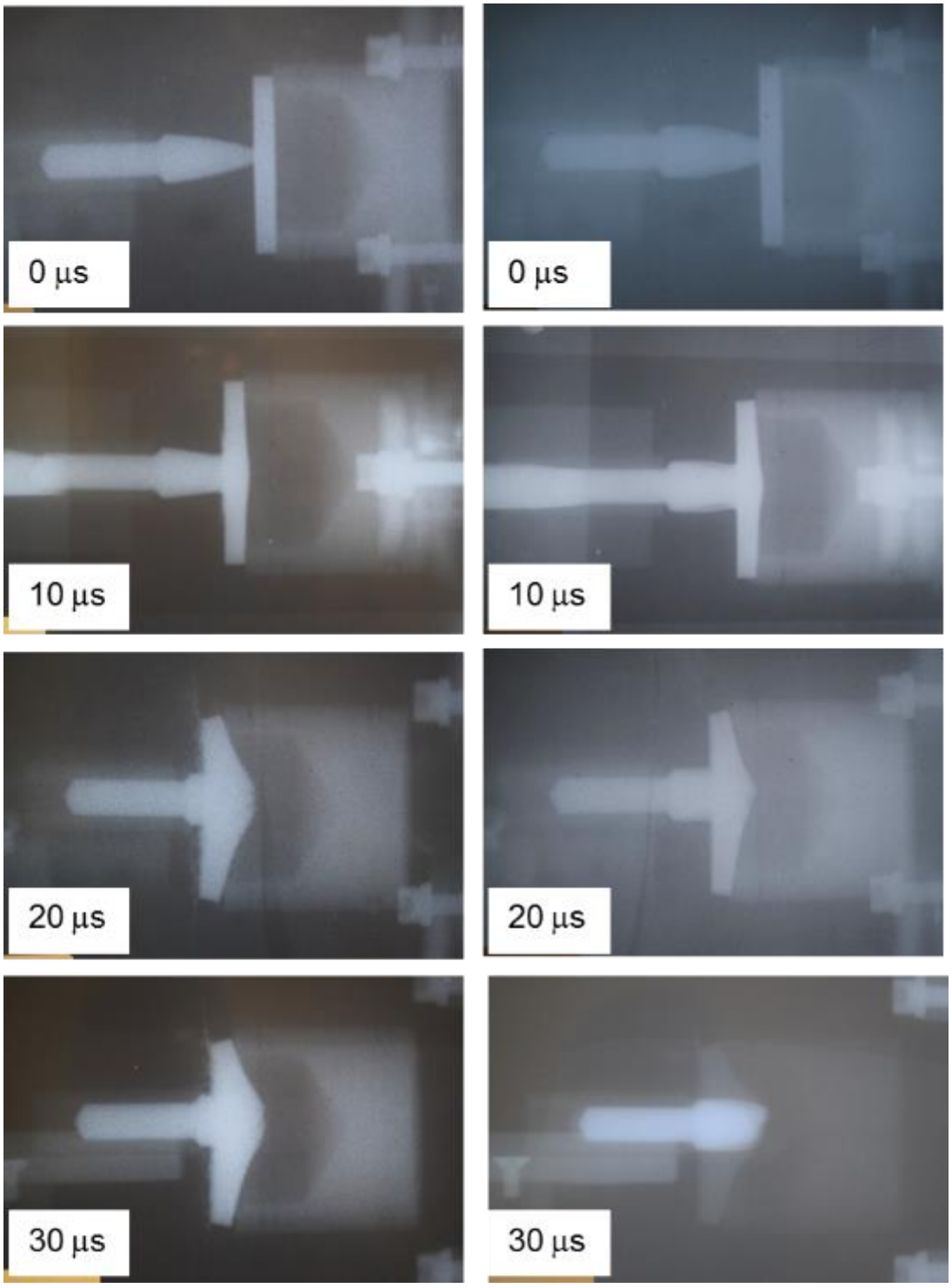

(a) un-jacketed core – exp. no. 1 (b) jacketed core – exp. no. 2

Figure 5.16 Flash X-rays showing impact of a 5-mm thick Armox Advance steel plate onto M2 steel core 42 HRC (experiments no. 1 and 2 from Table 5.6).

From these experiments the importance of the copper jacket is again highlighted. Interestingly, moving to an impactor plate thickness of 9 rather than 5 mm gave a significant difference in penetration performance. It was noted that the un-jacketed and jacketed rounds with hardness of 42 HRC were not able to penetrate the 9-mm target as shown in Figure 5.17 (a) and (b) – although again less erosion (surface 'splash') was apparent where a jacket was present. Given that there is a difference in behaviour even when the hardness of the core is relatively low this suggests that an element of this enhanced performance may be attributable to steel core confinement as well as the cushioning effect – e.g. that the jacket acts to reduce radial expansion during the impact event, confining the core and enhancing its ability to penetrate the target.

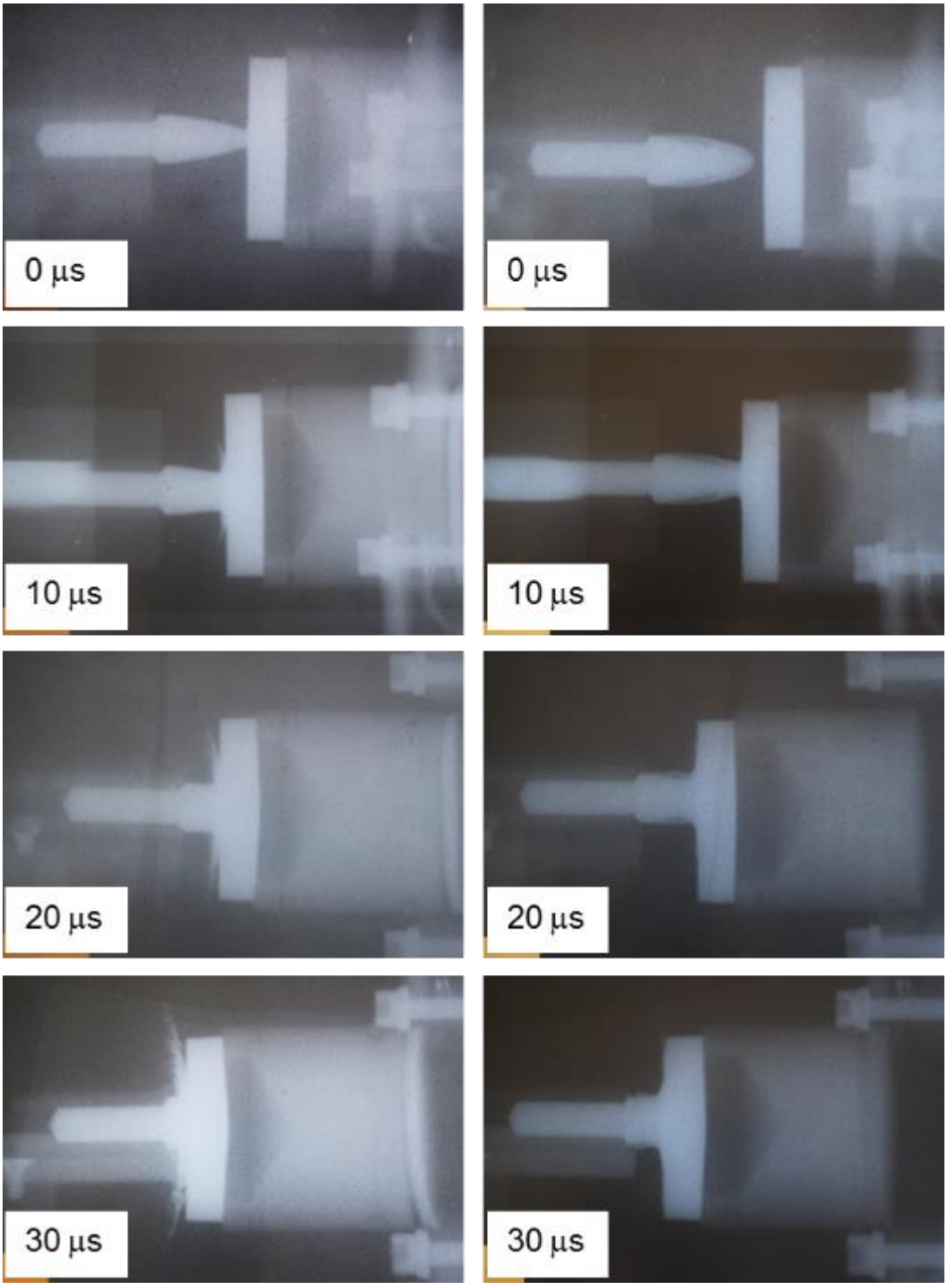

(a) un-jacketed core – exp. no. 7 (b) jacketed core – exp. no. 8

Figure 5.17 Flash X-rays showing impact of a 9-mm thick Armox Advance steel plate onto M2 steel core 42 HRC (experiments no. 7 and 8 from Table 5.6).

The same basic penetration behaviour noted for the 42 HRC case was observed for the M2 steel projectiles with hardness's of 52 HRC. Figures 5.18 (a) and (b) show how the un-jacketed and the jacketed projectile penetrated the 5-mm thick impactor. Both projectiles tips were eroded during penetration, but again it was notable that the jacketed projectile exhibited less erosion because of the presence of the copper jacket protection. In turn, Figure 5.19 presents the flash X-rays captured during the corresponding (52 HRC) 9-mm thick impactor experiment. . In this case the 9-mm target had an average measured hardness of 59 HRC meaning that the 'target' still over-matched the projectiles. However, it can be observed from Figure 5.19 that the impact of this steel core resulted in less material fragments spreading on the target surface compared 5-mm target impact.

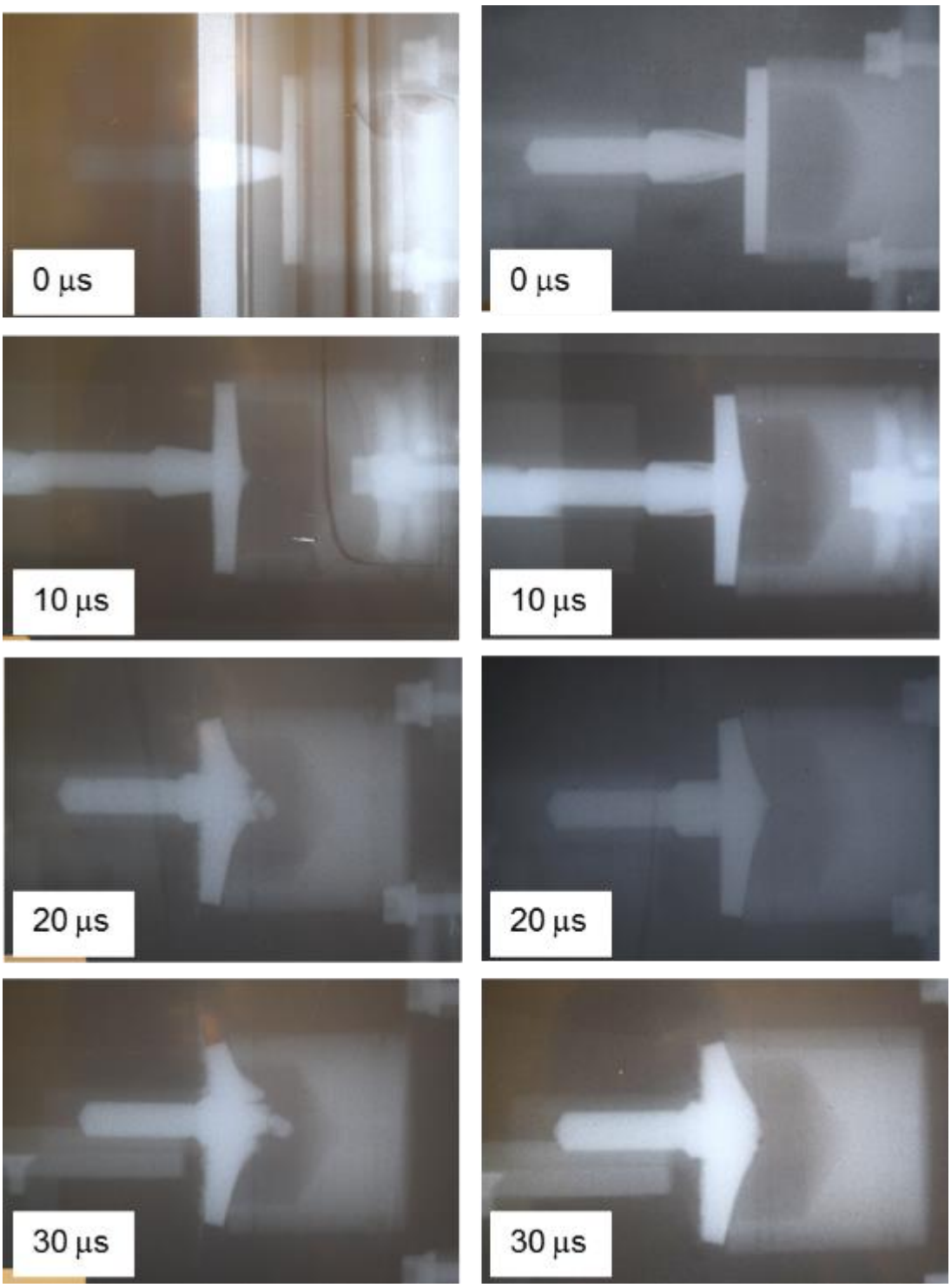

(a) un-jacketed core – exp. no. 3 (b) jacketed core – exp. no. 4

Figure 5.18 Flash X-rays showing impact of a 5-mm thick Armox Advance steel plate onto M2 steel core 52 HRC (experiments no. 3 and 4 from Table 5.4).

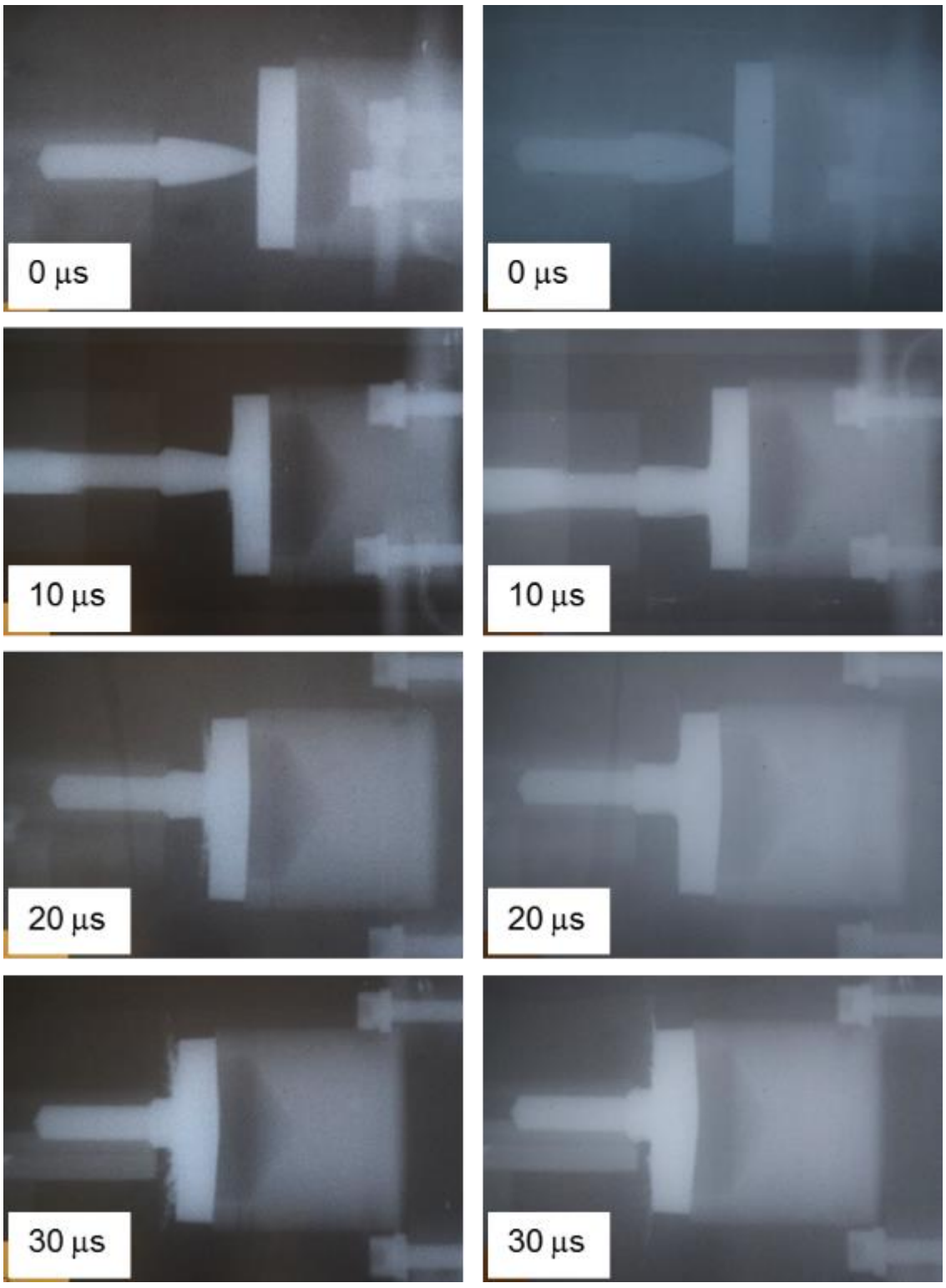

(a) un-jacketed core – exp. no. 9 (b) jacketed core – exp. no. 10

Figure 5.19 Flash X-rays showing impact of a 9-mm thick Armox Advance steel plate onto M2 steel core 52 HRC (experiments no. 9 and 10 from Table 5.4).

In contrast to the 42 and 52 HRC projectile experiments, use of the highest steel hardness – 62 HRC – led to a catastrophic failure of the targets during the penetration process. Both the un-jacketed and jacketed projectiles penetrated the target steel with 5 and 9 mm in thickness (Figure 5.20 and Figure 5.21 respectively). The un-jacketed projectile penetration mechanism on the 5-mm thick impactor plate is described by X-Ray images in Figure 5.20 (a), with the corresponding jacketed projectile penetration event illustrated in Figure 5.20 (b). At the moment of impact, the un-jacketed projectile eroded the impactor surface because of its higher hardness characteristic. Following this, at 20 and 30 μs after the first impact, the penetrator had passed through the 5-mm thick plate and had a broken tip. A different result was generated by the jacketed projectile penetration. The copper jacket appeared to cause initial damage to the impactor while also confining and protecting the core (which appears from Figure 5.20 (b) to have remained in one piece). Figure 5.20 (b) then illustrates at 20 and 30 μs complete penetration of the jacketed projectile without any tip erosion, although some core plastic deformation from the penetration process is apparent.

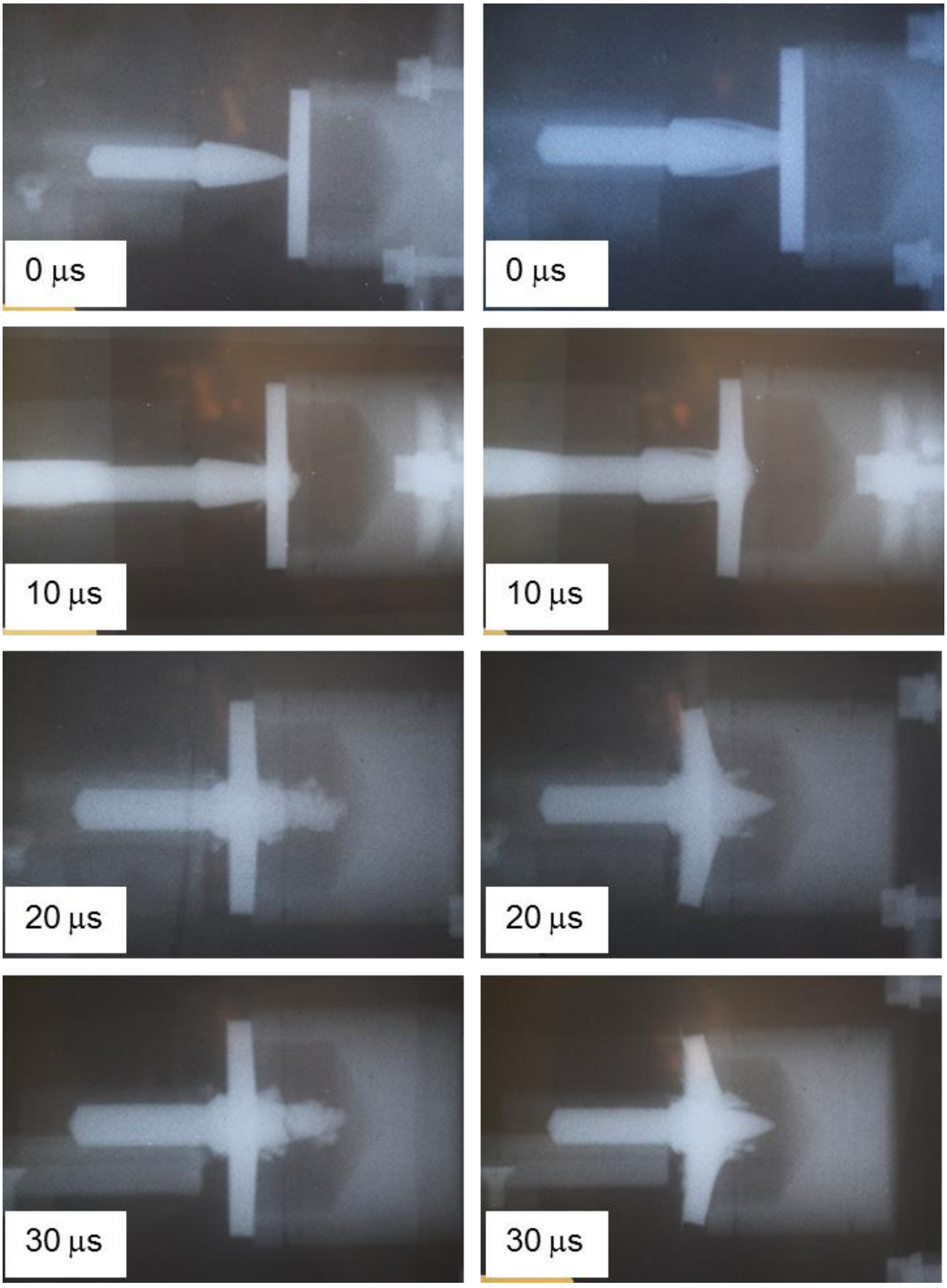

(a) un-jacketed core – exp. no. 5 (b) jacketed core – exp. no. 6

Figure 5.20 Flash X-rays showing impact of a 5-mm thick Armox Advance steel plate onto M2 steel core 62 HRC (experiments no. 5 and 6 from Table 5.4).

Increasing the target thickness to 9-mm did not prevent the 62 HRC steel core from penetrating the plate. Figures 5.21 (a) and (b) describe the penetration of the un-jacketed and the jacketed projectile on the 9-mm Armox Advance plate respectively. A consistent behaviour was observed during penetration. Again, it was noted – as in the 5-mm thick impactor case in Figure 5.20 (a) – that the presence of the copper jacket appeared to initiate a degree of 'pre-damage' as well as confining the core. To provide further insight into the penetration behaviour of all types of projectile impact on both 5 and 9-mm thick Armox Advance plate, the projectiles and the impactor plate were recovered after the tests and further analysed.

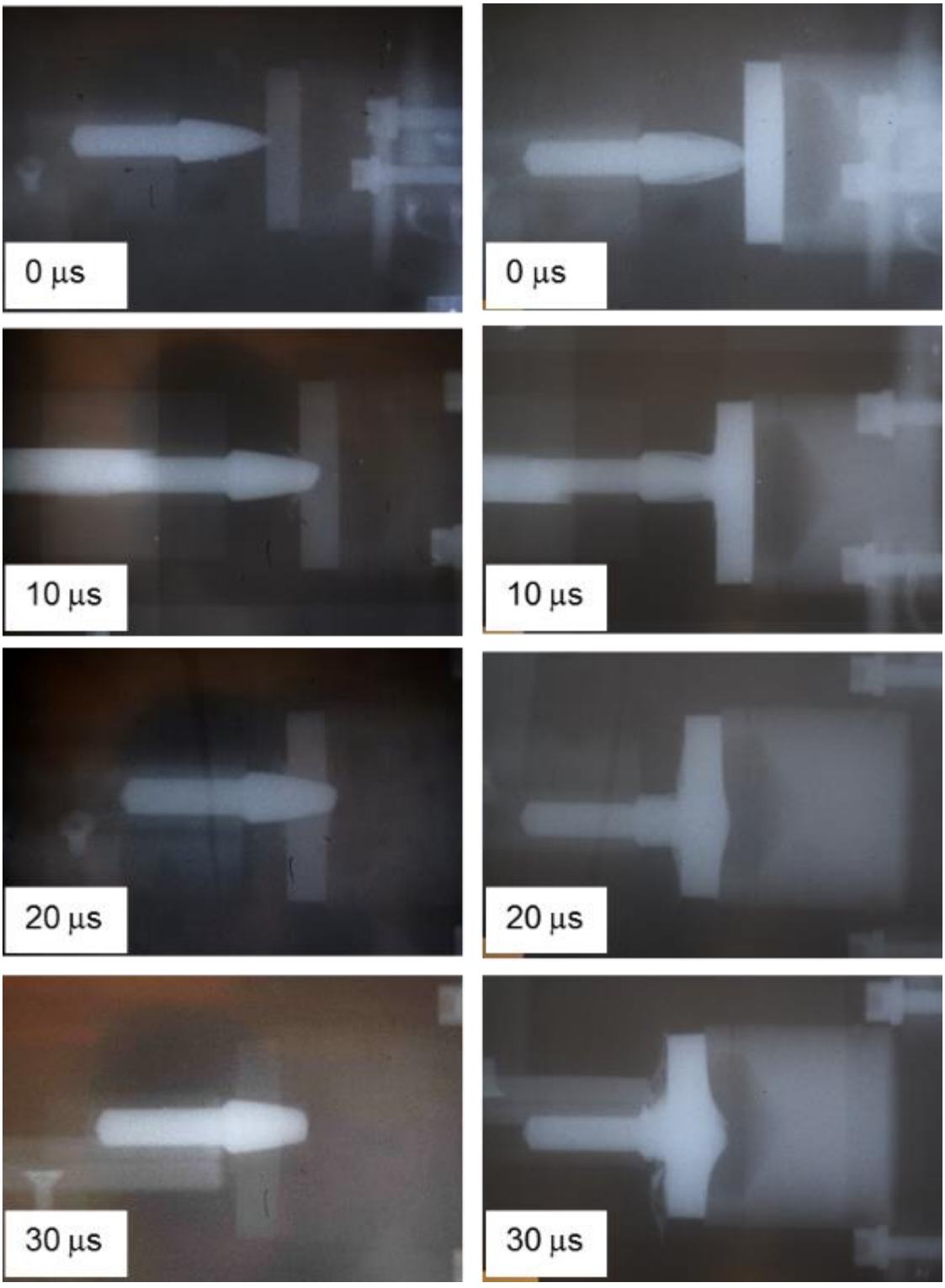

(a) un-jacketed core – exp. no. 11 (b) jacketed core – exp. no. 12

Figure 5.21 Flash X-rays showing impact of a 9-mm thick Armox Advance steel plate onto M2 steel core 52 HRC (experiments no. 11 and 12 from Table 5.4).

5.3.2.2 Recovered projectiles and target plates fragments

As with the forward ballistic experiments (Section 5.2), projectile and impactor fragments were collected after each test to provide further insight into the influence of both (M2 steel) core hardness and the presence (or lack thereof) of the copper jacket. In this reverse ballistic test, 50-mm diameter Armox plates with thickness 5 and 9-mm were employed as impactors. These impactor plates were smaller compared to forward ballistic targets which were 150 mm x 150 mm. A smaller edge to edge distance in the 50-mm diameter plate minimised plate stretching and bending during penetration. While, in 150 mm x 150 mm plates, stretching and bending occurred upon impact due to projectile pressure. Those resulted in an additional cracking damage during penetration.

Figure 5.22 shows the projectiles and impactor debris recovered from the 5-mm impactor reverse ballistics experiments. As detailed in the preceding section, projectiles with hardness's of 42, 52 and 62 HRC were all able to penetrate 5-mm thick Armox Advance plate. Of particular note is the fact that the 5 mm plate fragments in the un-jacketed projectile experiments in Figure 5.22 appear to be generally larger than those for generated by jacketed projectile impact (e.g. for the 62 HRC projectile case there are just 4 large fragments for the un-jacketed case versus ca 11 for the jacketed case). This is consistent with the concept of the jacket enhancing penetration – with the lower number of 'target' fragments in the un-jacketed case suggesting that energy has been coupled back into the projectile, disrupting / reducing its ability to penetrate – rather than into target defeat.

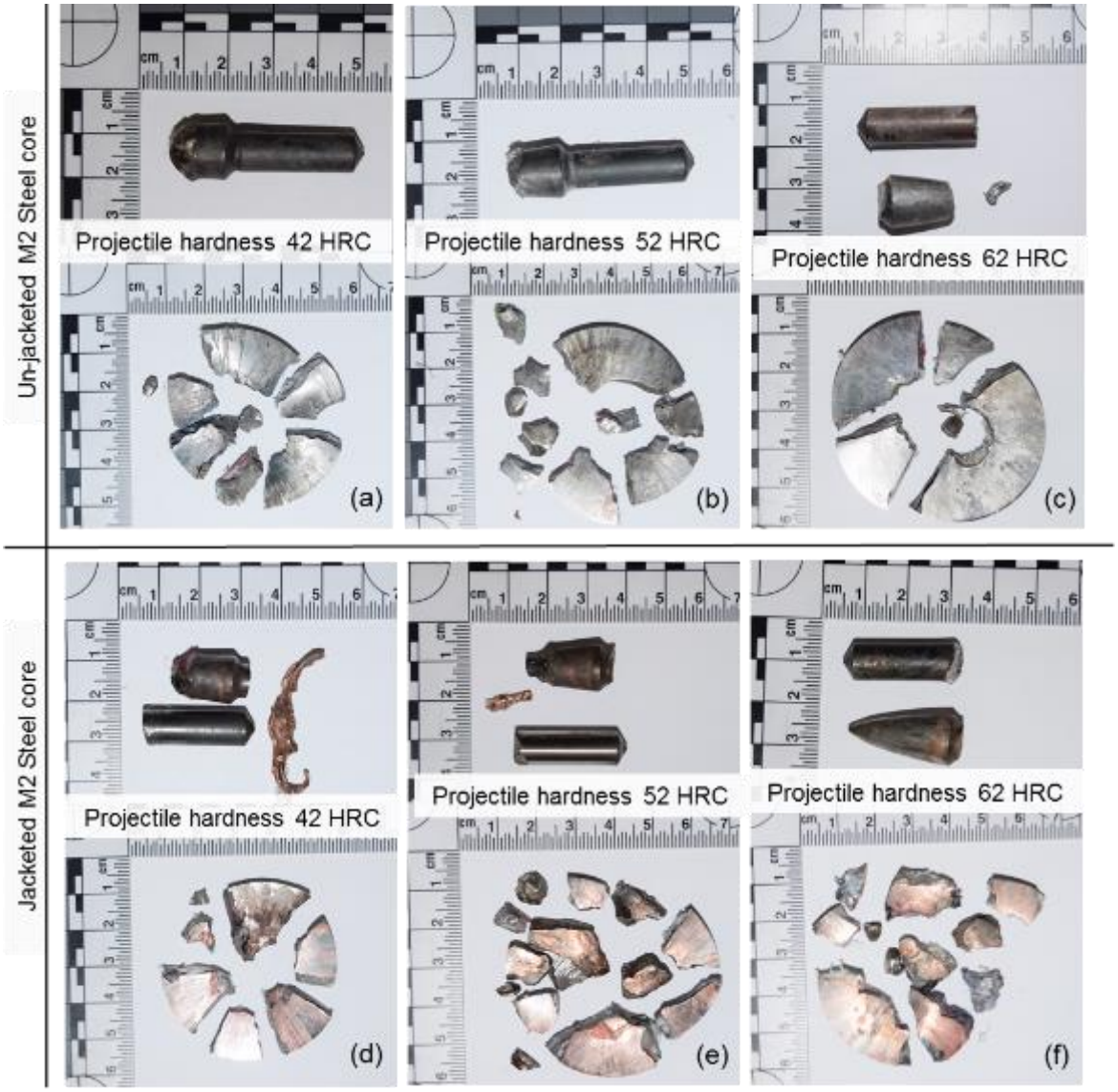

Figure 5.22 Recovered fragments of projectiles and 5-mm impactors, (a-c) un-jacketed projectiles; (d-f) jacketed projectiles.

In was also observed – as touched on in discussion of previous experiments – that the copper jacket appeared to protect the core from direct damage. This was reflected in a higher overall length of recovered core material post-shot. This effect is highlighted Figures 5.23 and 5.24 which show total recovered core length for the un-jacketed and jacketed cases against 5-mm thick Armox Advance plates (following reverse ballistic testing) respectively.

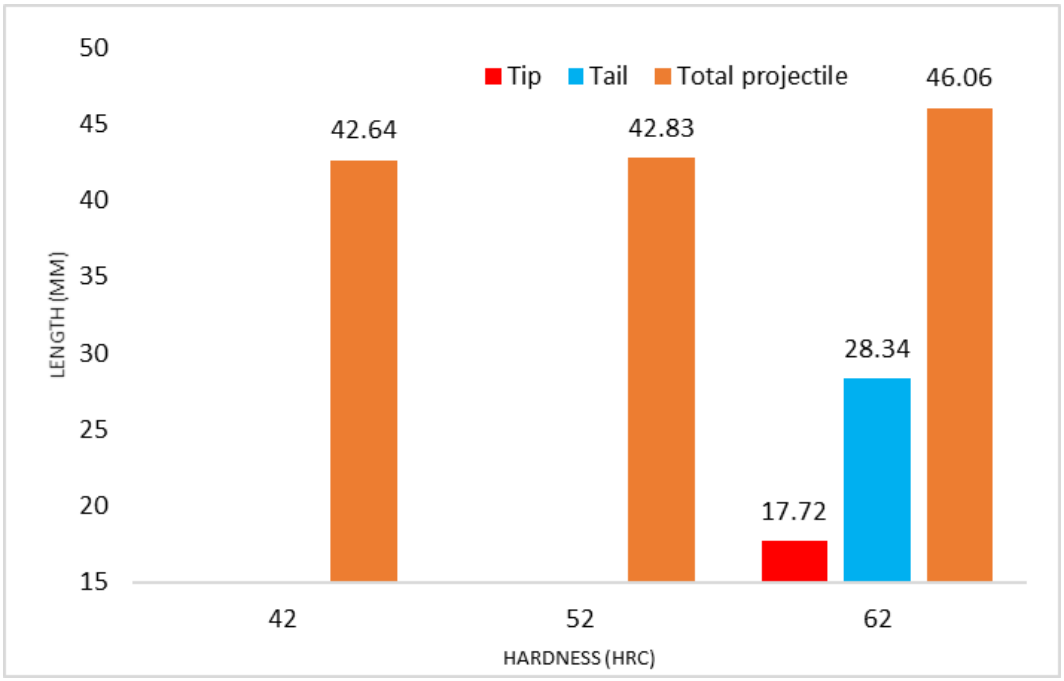

Figure 5.23 Recovered projectiles (42, 52, 62 HRC) of un-jacketed projectile after being impacted by 5-mm thick Armox plates.

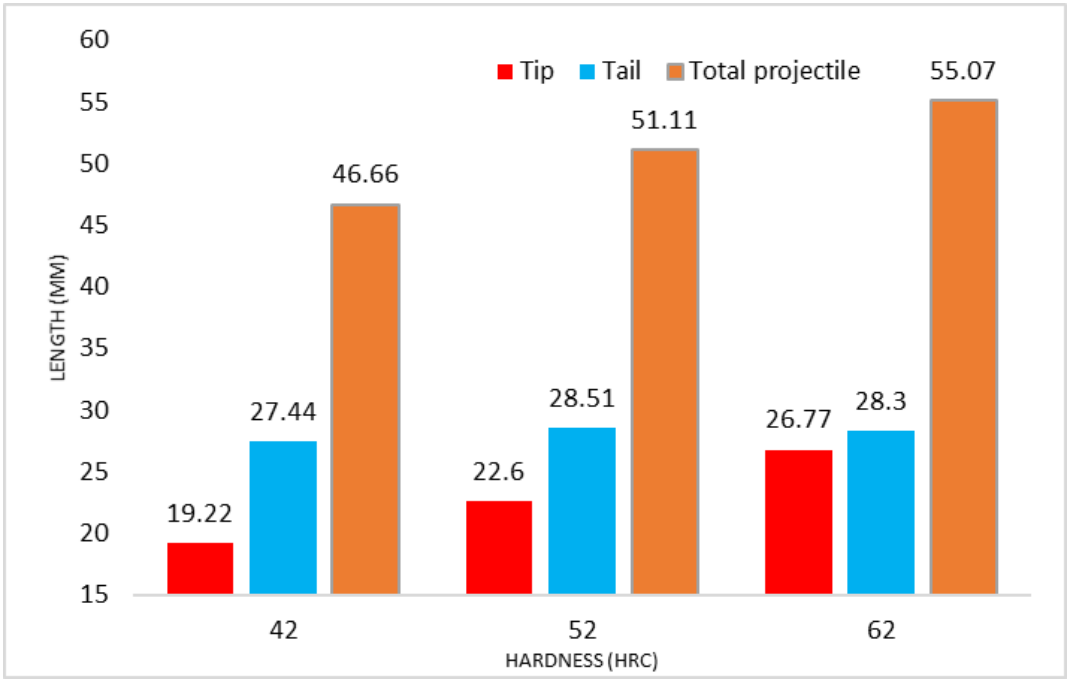

Figure 5.24 Recovered projectiles (42, 52, 62 HRC) of jacketed projectile after being impacted by 5-mm thick Armox plates.

However, it was interesting to note that the presence of the copper jacket consistently led the projectile to be broken after leaving the plate. This is reflected in Figure 5.24 where in each case lengths of key individual fragments recovered along with the total length of large coherent core segments recovered are plotted (this was also the case for the highest hardness un-jacketed case in Figure 5.23).

Essentially, the presence of the copper jacket with its high density / impedance will have led to generation of a higher pressure during the impact than in the corresponding un-jacketed case. This higher-pressure wave would have then reverberated leading to spallation of the core. This behaviour is particularly interesting, however, as it clearly indicates that confinement is playing a part during the penetration process – e.g. that the projectile despite this higher initial loading when a jacket is present only fails once confinement is relieved (e.g. on exit from the target – at which point, as illustrated clearly in Figure 5.20 (a). this conclusion is backed by the fact that only the highest hardness (62 HRC) un-jacketed projectile was found broken; in this case presumably because of enhanced brittleness (the harder the material, the more brittle it is) leading to increased susceptibility to failure following tensile release post-impact.

In both the un-jacketed and the jacketed projectile experiments, hardness condition played an important role in core intact length after penetration. Increasing hardness values consistently led to a larger recovered core length. Overall, over-match is also clearly important; e.g. the projectiles with hardness of 42 and 52 HRC were eroded by the Armox Advance plate before complete penetration, whereas for the 62 HRC projectile the target plate's strength was overcome and the target was rapidly penetrated. These phenomena were clearly described by the X-ray images presented previously and are supported by the analysis of recovered experimental (projectile and impactor / target) material discussed here.

Finally, this behaviour was reinforced with reverse ballistic experiments with a 9-mm thick Armox Advance impactors. As illustrated in Figure 5.25, overall no significant penetration occurred in either the jacketed or un-jacketed for hardness values of 42 and 52 HRC. Although for the un-jacketed case the projectile fractured into two distinct parts, consistent with a higher projectile loading experienced due to the lack of a cushioning jacket. However, for the 62 HRC hardness, the projectiles overmatched the target and resulted in target defeat. For both jacketed and un-jacketed cases, the projectiles were significantly fragmented – although this appears to have occurred after penetration. On both cases, impactor material appears to have plugged / sheared ahead of the projectile. However, while for the un-jacketed case the impactor plate was broken into just three distinct parts, for the jacketed projectile the impactor plate was entirely fragmented. This clearly shows enhanced coupling of energy into the target. Interestingly, the cushioning effect of the jacket is also reflected in the presence of copper jacket material on the surface of the impactor plate fragments in Figure 5.25 (f) – showing that the jacket flowed over the surface on impact, protecting the core from an impulsive loading that might have shattered it prematurely. This allowed the projectile to be guided intact into the impactor plate, imparting more KE and ultimately leading to the observed enhanced fragmentation / comminution compared to the corresponding un-jacketed case in Figure 5.25 (c) / illustrated in Figure 5.26 which details the dimensions of revered core material for these 9-mm thick impactors / targets.

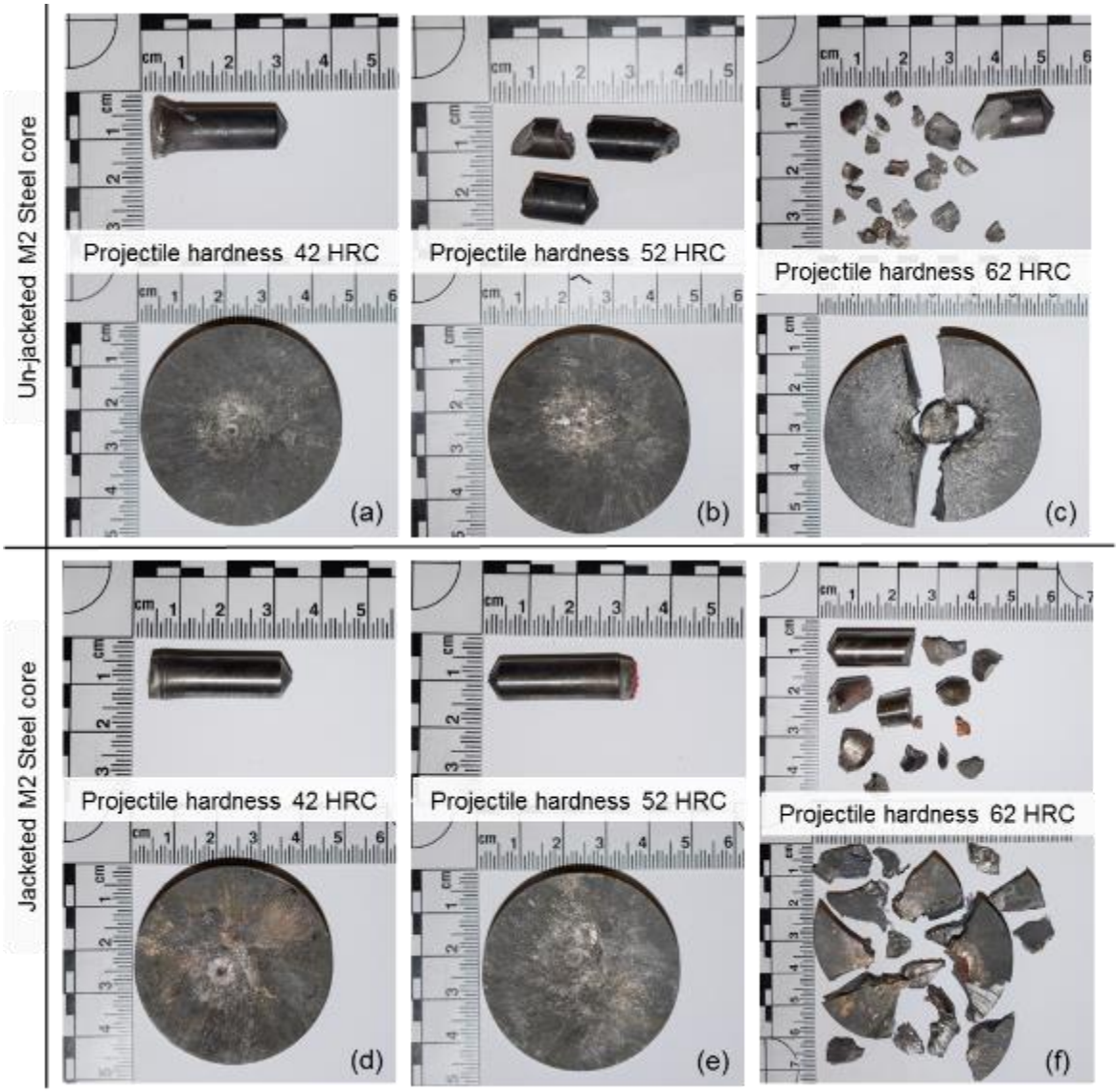

Figure 5.25 Recovered fragments of projectiles and 9-mm impactors, (a-c) un-jacketed projectiles; (d-f) jacketed projectiles.

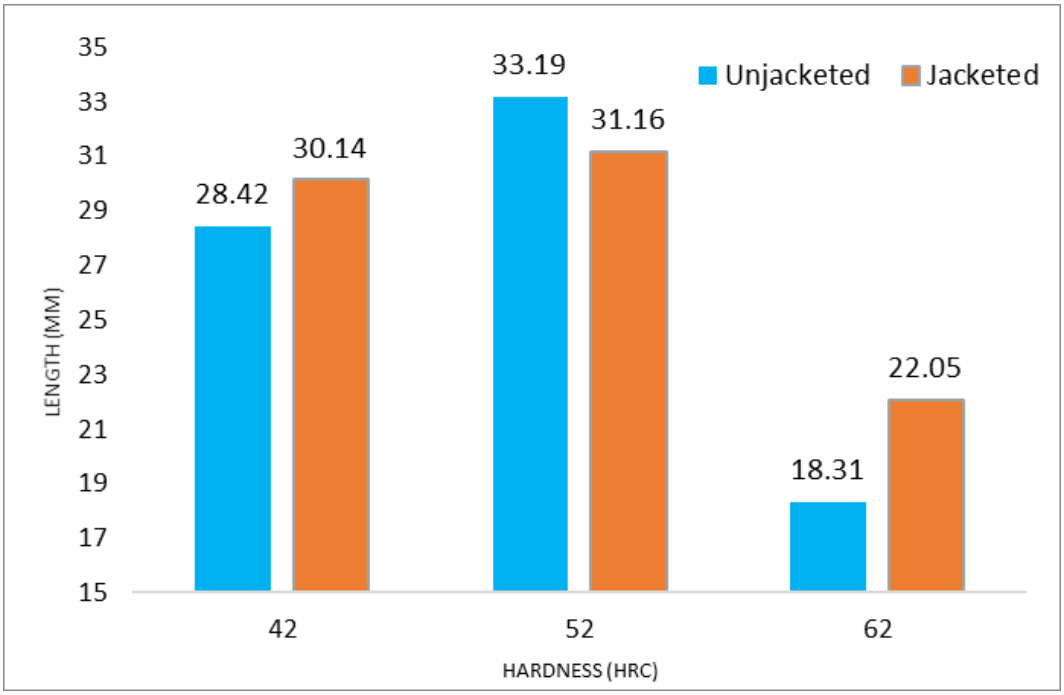

Figure 5.26 Recovered projectiles (42, 52, 62 HRC) of un-jacketed and jacketed projectile after being impacted by 9-mm thick Armox.

Forward and reverse ballistic experiments showed comparable results and highlighted the importance of both core hardness and the presence of copper jacket for penetration into Armox Advance plate. Essentially, harder cores had a better penetration performance while the copper jacket appears to pre-damage the target and, protects / cushions the cores from direct contact with the target surface. However, those experiments did not fully elucidate the nature and extent of energy transfer during the impact event. To this end, further observation of shock wave propagation in both the projectiles and the targets during the impact event were made by conducting pressure gauge experiment – something supported by numerical modelling.

5.4 Pressure gauge experiments

In addition to the ballistic experiments as discussed in section 5.2 and 5.3, a series of pressure gauge experiments were also conducted in order to investigate details of the impact conditions with / without jackets. A pair of target sets were tested by using the un-jacketed and jacketed projectile. There was a kinetic energy discrepancy between the un-jacketed and jacketed projectile due to mass difference as discussed in section 2.3. Resultant data for these experiments – following the setup detailed Figure 3.7 – are set out in Table 5.7 which shows projectile impact velocity, pressure measured in the PMMA backing, as well as details of target and projectile recovery.

Table 5.7 Pressure gauge experiments results.

Parameters	**Unjacketed core**	**Jacketed core**
Projectile velocity (m/s)	641.03	641.03
Pressure measured (GPa)	0.136	0.185
Al 7075 target fragments	4 fragments, 1 big crack	5 fragments, 3 layers of spalling planes
En8 Steel core fragments	1 core intact with eroded tip	2 fragments

A typical pair of gauge traces recorded in the PMMA backing behind the targeted Armox plates are presented in Figure 5.27. Both un-jacketed and jacketed projectiles have a similar curve pattern. On impact a shock caused by projectile impact results in a rapid rise of to a pressure peak. The jacketed core projectile impact leads to a higher-pressure rise (b) compared to the pressure measured after un-jacketed core impact (c). This likely reflects the cushioning effect of the core touched on previously. The initial shocks decay back because the incoming shocks are reduced by reflected wave that propagates back into the projectile. The higher the initial stress, the higher the amplitude of the reflected wave. This behaviour is in agreement with the subsequent pressure decrease in the jacketed core impact (d) which exceeds that of the unjacketed core (c). The shock wave

continue to propagate within the target (e) as long as it does not surpass the material strength.

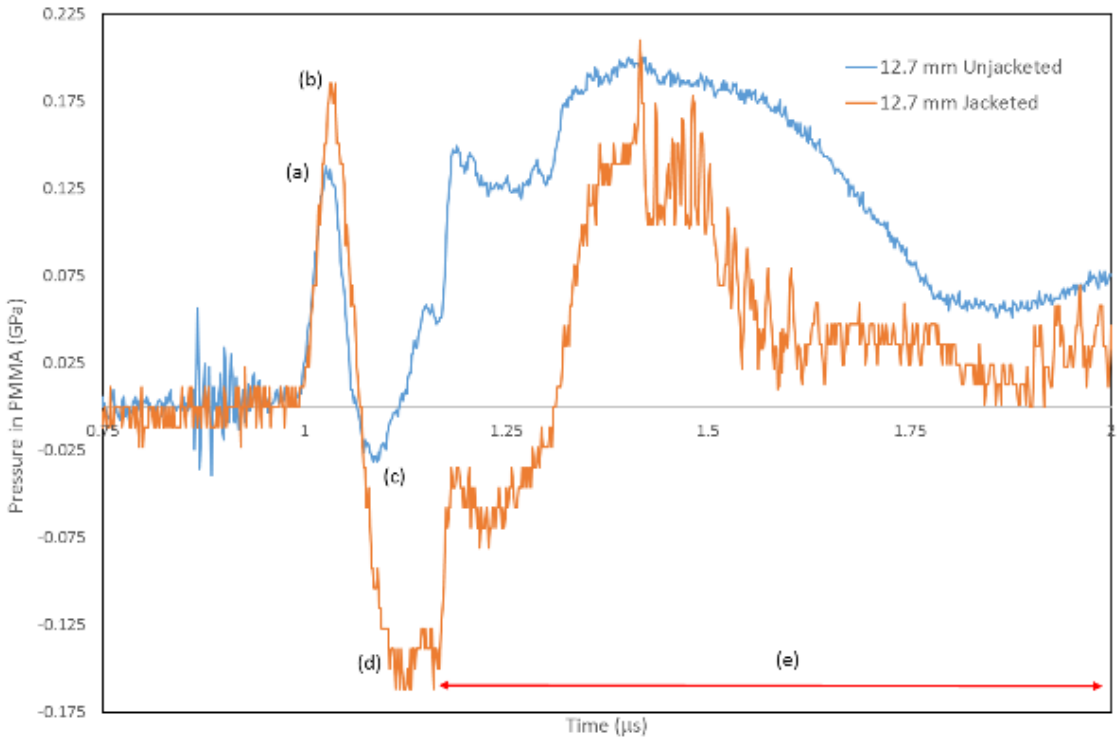

Figure 5.27 Pressure gauge traces of the jacketed and unjacketed 12.7 mm En8 steel cores.

As discussed in section 1.3.6, when an initial compressive wave travels through projectile into target which is assumed to be a higher impedance material, a compressive wave is transmitted to the target and a compressive reflection wave is reflected back into projectile. If the reflected or transmitted stress wave surpasses the yield strength of the material, the material will experience plastic deformation for ductile materials and fast fracture for brittle materials.

Overall, from these traces – consistent with the findings from the forward and reverse ballistic impact experiments discussed previously – it is apparent that the copper jacket protecting the core has a significant effect on the impact of the projectile. The copper jacket appears to provide initial damage to the target

surface and, simultaneously, absorbs the shock wave reflected by the targeted Aluminium plate back into the projectile. The copper protection therefore allows the steel core to penetrate with a better performance. In contrast, the un-jacketed core projectile was damaged at the moment of impact with the target and a reflected shock wave was directly transferred within both the projectile and the impacted steel material. Analysis of recovered core material suggests that this exceeded the dynamic tensile strength of the core leading to spallation as shown in Figure 5.28.

(a) Recovered En8 steel cores (b) Al target's fragments

Figure 5.28 Projectile and Al 7075 fragments.

As touched on above, Figure 5.28 shows evidence of spall in the shocked un-jacketed projectile (a) and both Al 7075 plates (b). Such dynamic tensile failure arises due to the release of compressive loading following impact and subsequent tensile failure. This spall behaviour also occurred in the Al target; a total of five-Al fragments were recovered and those fragments showed that the Al targets penetrated by the jacketed core had typically three-spall planes (e.g. energy was successfully coupled into the target) – whereas that for the un-jacketed round had just one (indicative of inefficient energy transfer into the target / consistent with the premature core failure detailed in Figure 5.28 (a).

5.5 Numerical simulation

A series of numerical simulation were performed using the projectile with the best penetration performance based on experimental results that was that with a hardness of 62 HRC. This research focused on the copper jacket effect on the penetration mechanism of the M2 steel core into Armox Advance target plates. Both un-jacketed and jacketed projectiles were employed in the simulation according to procedure explained in Section 4. The projectiles were modelled by using Solidworks software and exported as a *.STEP file before being applied as a 3D model in ANSYS Explicit Dynamic. All engineering data assignment, meshing as well as analysis and initial condition setting were done in ANSYS Explicit Dynamic. The initial velocity in x-axis direction of projectile was 750 m/s. The following steps, control-output setting; simulation running; and post analysis, were conducted in ANSYS Autodyn®. The residual velocity of fragments were obtained from the velocity of the intact core after leaving the target in the post simulation result display in ANSYS Autodyn®.

5.5.1 Mesh sensitivity study

In this simulation work, modelling was done by using different mesh size to observe the effect of mesh size on the residual velocity of projectiles. Mesh sizes employed to this study were consistent across the different model / system components (core, jacket and target plate) for a given simulation and were 0.6, 0.7, 0.8, 0.9 and 1.0 mm. Figure 5.29 describes the resultant simulated fragment velocity of un-jacketed and jacketed projectiles for the different mesh sizes considered versus experimental results.

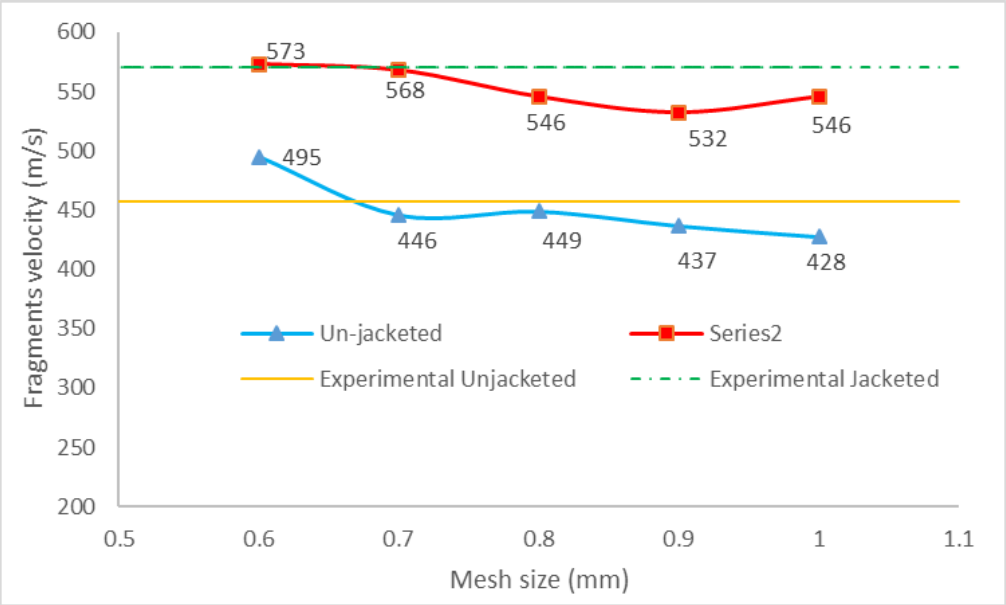

Figure 5.29 Average velocity of fragments in simulation compared to experimental results.

Different mesh sizes between 0.6 and 1.0 mm were applied in un-jacketed core simulations of impacts on to 9-mm targets. According to Figure 5.29, the fragment velocity of the projectile after leaving the target plate was consistently comparable that measured experimentally. Using the 1.0 mm mesh size in simulation resulted in a fragment velocity 428 m/s – just 22 m/s below the experimental value. Overall, mesh sizes of 0.9, 0.8 and 0.7 mm gave a stable fragment velocity magnitude – however the smallest mesh size of 0.6 mm, increased simulated fragment velocity to a more un-realistic 495 m/s.

Simulation of the behaviour of the jacketed projectile using the same mesh size variation generated higher fragment velocities compared to the un-jacketed case. This result was in good agreement with experimental results. A mesh size between 0.8 and 1.0 mm showed a relatively constant result, while decreasing mesh size to 0.7 increased the velocity close to the experimental value.

From the result above, it was observed that simulation work using mesh sizes between 0.7 and 1.0 mm produced good data which corresponded well to experimental results. However, the 0.7 mm mesh size give the best overall match to experimental data and was consequently adopted.

5.5.2 Numerical simulation result

In this study, the simulations were conducted in ANSYS Autodyn® using three-dimensional models with parts imported from Solidworks and settings performed in ANSYS Explicit Dynamics respectively. Model configurations were selected to reflect the fact that this study is designed to evaluate both the penetration mechanisms underpinning un-jacketed steel core penetration on high hardness armour steel as well as the influence of a ductile copper jacket on penetration. To this end, for each projectile (un-jacketed and jacketed), simulation results have been compared with corresponding experimental result as well as with each other.

A mesh-based Lagrangian formulation was employed for these simulations because it has a low computational cost and accommodates complex material model variety (53). However, it was observed that the Lagrangian method was very sensitive to mesh distortion which results in time step drop, an increase in simulation time and simulation error. This problem was solved by applying erosion criteria for all the materials. In this study, the point at which material erosion of the steel core and Armox Advance plate occurred was defined as that at which they reached their maximum principal stress. In concert, for the copper jacket, erosion was set to depend on geometrical strain with a maximal value of 1.5 (70).

The projectile core and copper jacket have complex geometries and are not sweep-able body. Consequently, tetrahedron elements were applied to these parts to prevent very small elements being generated which would have led to long simulation run times and simulation errors. Further, use of such elements presents a good three-dimensional geometry with an ogive shape and a lot of edges. The Armox Advance plate which dimension was 150 mm x 150 mm x 9 mm was modelled using hexahedron elements because its sweep-able body and it also undergoes large deformation during the penetration. All of the parts geometries were similar to those employed in the forward ballistics test but the models were sliced to be a half symmetry model to save computational time. The Armox Advance plate was divided to circular part, 47 mm in diameter, and

remaining part. A smaller hexahedron meshing was applied to the circular plate to accommodate more accurate modelling during penetration. Whereas, another part had a larger elements to reduce the number of elements and nodes.

The target was modelled as a plate clamped on both the top and bottom edges – consistent with the experimental setup (see Figure 3.2), while the impact velocity was set at 750 m/s. This value was the estimated velocity of 12.7 mm armour piercing projectiles at 500 m from the weapon muzzle; e.g. the models would therefore theoretically represent the penetration behaviour of the steel cores in question after leaving the barrel and hitting the target at a distance of 500 m.

Figure 5.30 shows the numerical simulation of projectiles impact into Armox Advance plate 9-mm thick. In 10 μs after the first contact between projectiles and target plates, it can be observed that both un-jacketed and jacketed projectile damage the target surface but in different mechanism. The unjacketed core which has a sharp tip penetrate the target with a very high loading. Because of its small surface area, it is observed to produce high pressure at / within the target. However, this tip tend to be eroded upon impact even though the projectile hardness was higher than that of the target hardness. The eroded elements of steel core were retained and had a contribution to subsequent plate damage. In Figure 5.30 (a), the eroded elements of the steel core and the intact remaining core material penetrated the target plate perfectly at 47 μs. By the following time step, the eroded elements of the steel core spread out behind of the target plate.

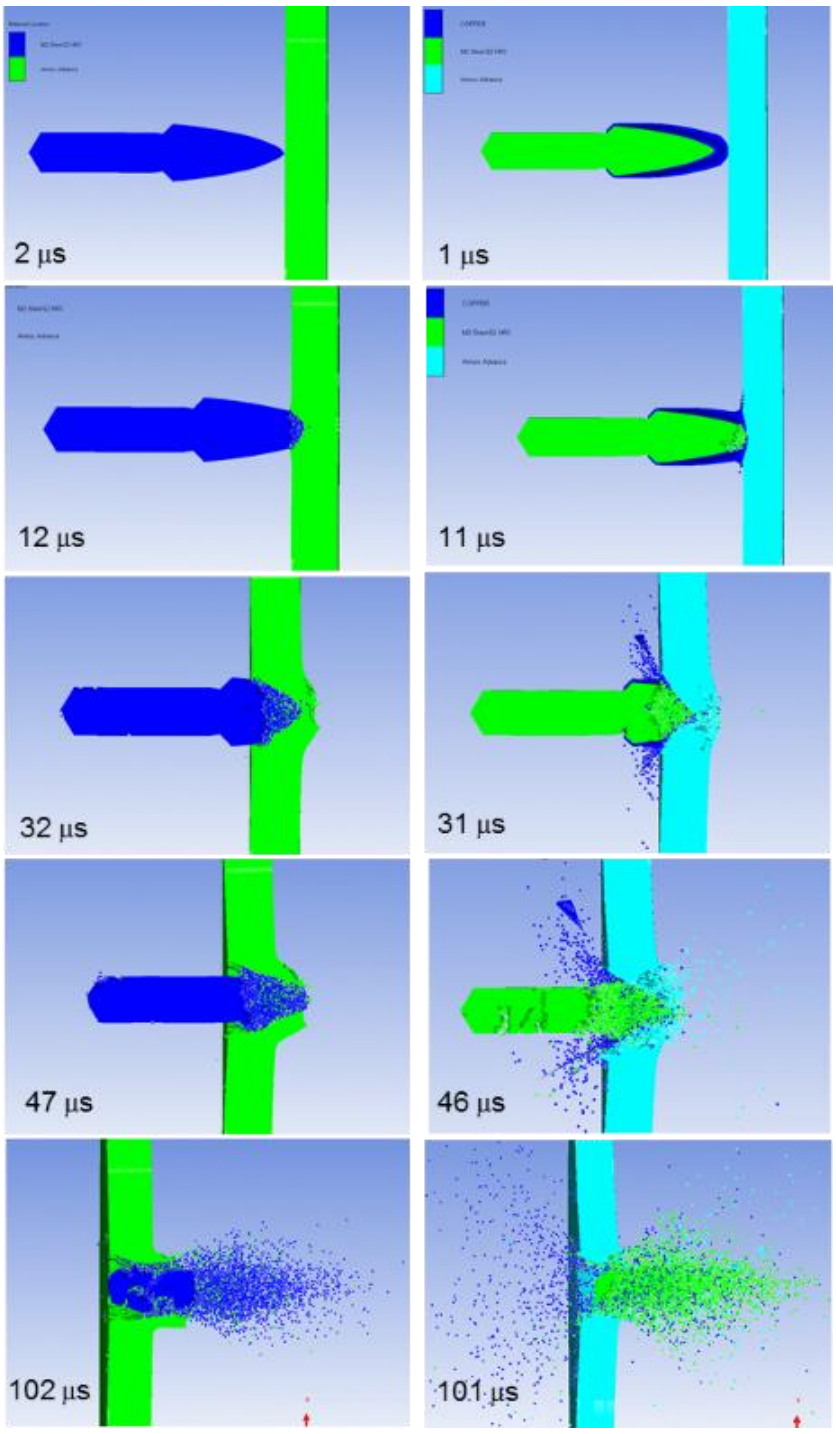

(a) Un-jacketed M2 steel core (b) Jacketed M2 steel core

Figure 5.30 Numerical simulation result of projectiles impact into Armox Advance plate 9-mm thick.

A different mechanism occurred in terms of the jacketed projectile penetration, however. Figure 5.30 (b) illustrates that at 11 μs the copper jacket experienced a

deformation which result in a wider contact area during the impact. This copper jacket plays a role in ensuring confinement of the steel core until it is able to penetrate into the target which point it will be confined by the surrounding target material. Interestingly, analysis of the degree of simulated penetration of the jacketed core at 31 and 46 μs showed that the copper jacket contributed to initial damage and generated a higher energy to damage the plate before fully penetrated. It can also be observed that the higher energy loaded to the target surface resulted in a higher amplitude of energy being reflected back into the steel compared to the un-jacketed case. This is reflected in the fact that at later stages in Figure 5.30 the jacketed core has been comminuted into smaller fragments compared to the un-jacketed projectile. Interestingly within the simulation eroded copper elements were found in front and rear side of the target. This is illustrated in Figure 5.31 – importantly as will be detailed later this response was in good agreement with experimental observations.

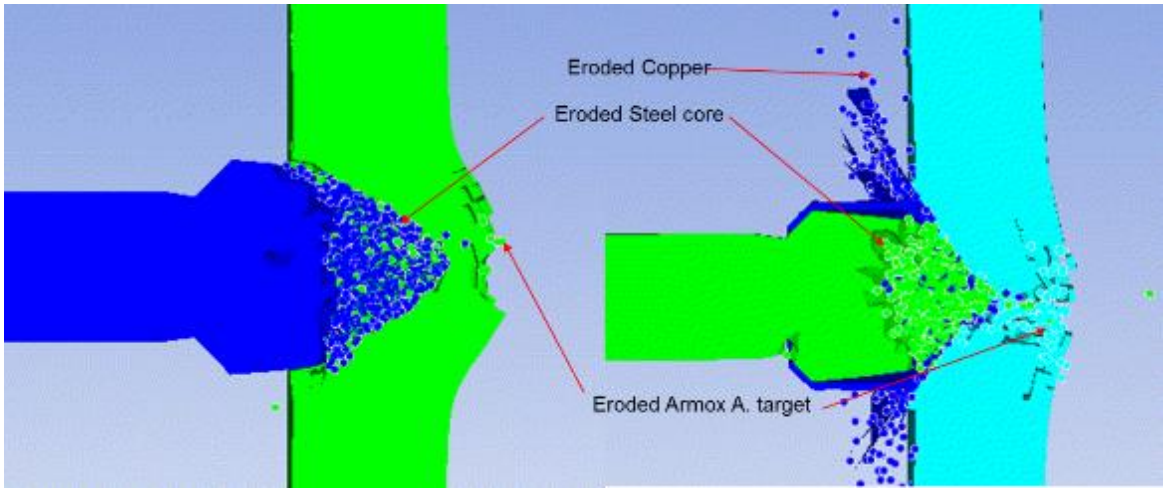

Figure 5.31 Eroded elements during simulations.

During the penetration, pressure generated due to the high velocity impact propagated within both the projectiles and the target. This 'shock' propagation was described in Figure 5.32. These images represent the simulation results with a contour view of pressure between 0.1 and 1.0 GPa. In line with the associated

key, the red area describes a region where the pressure is 1.0 GPa and above. In initial penetration, impact of both the un-jacketed and jacketed projectiles evolved a pressure of 1 GPa or above. Of particular note in Figure 5.32 (b) is the fact that the copper jacket, where present, delivered a high initial pressure to the target surface before the steel core impact occurs (at 4 μs). The following simulation cycle shows that the shock wave generated by this impact reflected back and propagated within the steel core body and target plate. This reflected shock wave would in the real world have led to dynamic tensile / spall failure when the reflected waves from the side or rear surface of the projectile overmatched the cores spall strength. Moreover, the higher pressure delivered by the jacketed projectile would have generated in greater damage to the target plate. It can also be observed in Figure 5.32 that the high-pressure (red) area in the target plate impacted by the jacketed projectile is physically bigger in extent compared to that for the un-jacketed projectile case. Importantly, these results are consistent with the observations from the pressure gauge experiments discussed in Section 5.4, providing enhanced confidence in their validity.

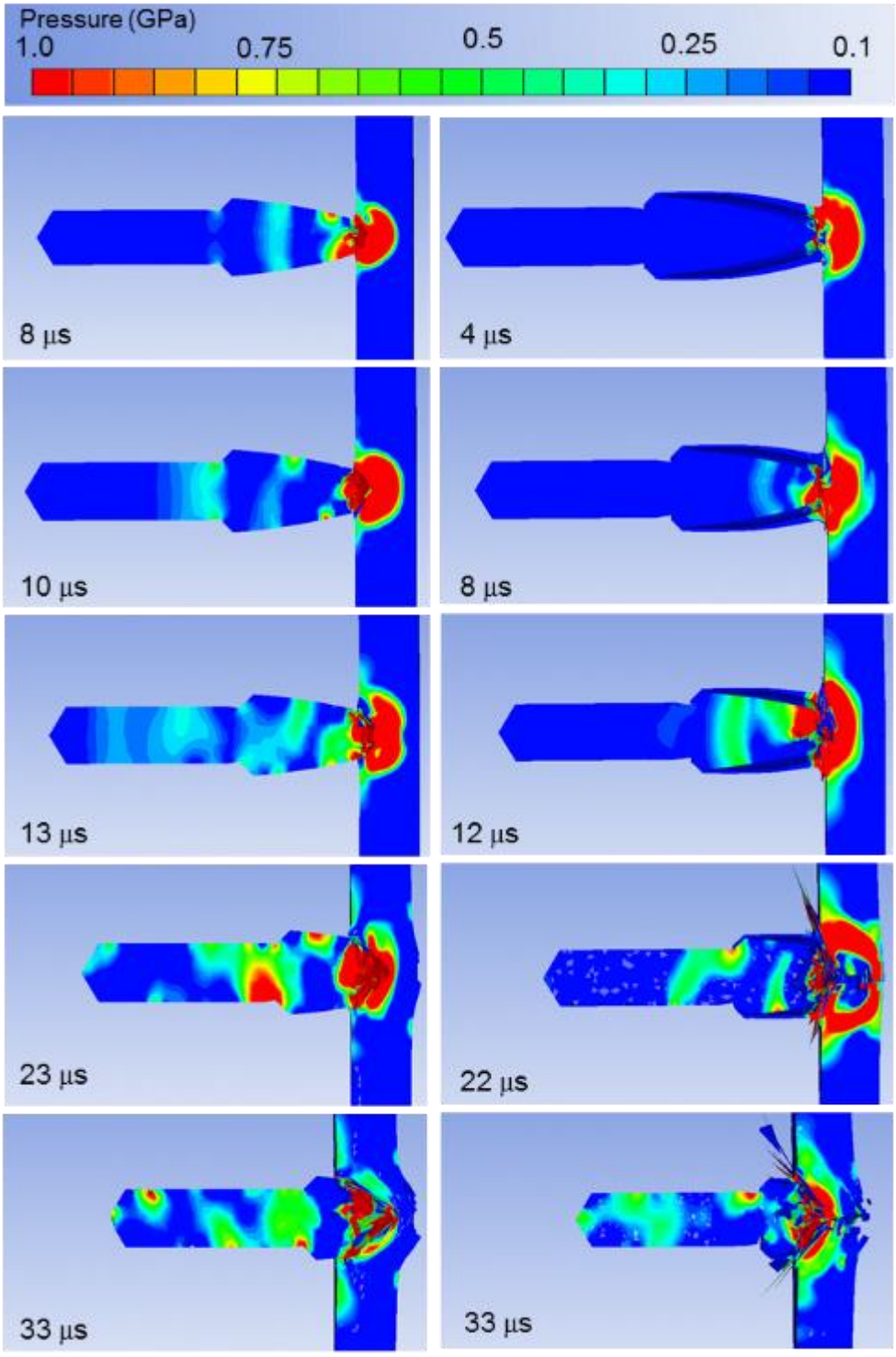

(a) Un-jacketed M2 steel core (b) Jacketed M2 steel core

Figure 5.32 Pressure dispersion within projectiles and target plates during impact.

During the penetration, pressure generated in high velocity impact propagated within both the projectiles and the target. This ‘shock’ propagation was described in Figure 5.32. These images were the simulation results with contour view of pressure between 0.1 and 1 GPa. The red area describes that the pressure is 1 GPa and above. In initial penetration both un-jacketed and jacketed projectile gave pressure 1 GPa or above. It is clearly described in Figure 5.32 (b) that the copper jacket of projectile delivered a high pressure on target surface before steel core hit the target (impact at 4 μs). The following simulation cycle shows that the shock wave reflected back and propagated within the steel core body and target plate. This reflected shock wave will lead to a spall failure when the reflected wave from the rear surface of projectile and target collide. Moreover, the higher pressure delivered by the jacketed projectile generated result in a greater damage to the target plate. It can be observed in Figure 5.32 that the high pressure (red) area in the target plated impacted by the jacketed projectile is bigger compared with the unjacketed projectile impact.

5.5.3 Comparison of numerical analysis with experiments

Numerical simulation and experimental results are compared in this section in order to assess the modelling accuracy in describing the observed penetration mechanisms for both the jacketed and the un-jacketed projectiles considered here. Flash X-ray images have been employed as the key point of comparison as they have provide clear and detailed pictures to describe the material failure.

Figures 5.33 (a) and (b) show the penetration mechanism for an M2 steel 62 HRC un-jacketed projectile. At 100 μs, the un-jacketed projectile’s tip is observed to initially impact and indent the target surface. Theoretically, because of their high hardness or brittle characteristic, both the projectile and the target would start to erode each other at this moment. At 10 μs intervals, it was observed in these flash X-rays that the projectile was able to penetrate, but that the tip of the core was gradually eroded. At a similar time interval, the simulations presented in Figure 5.33 (c) and (d) clearly the same penetration mechanism. At the moment

of projectile impact, the projectile's tip and the target are both eroded. In addition, the following penetration resulted in more eroded material in the target and the projectile.

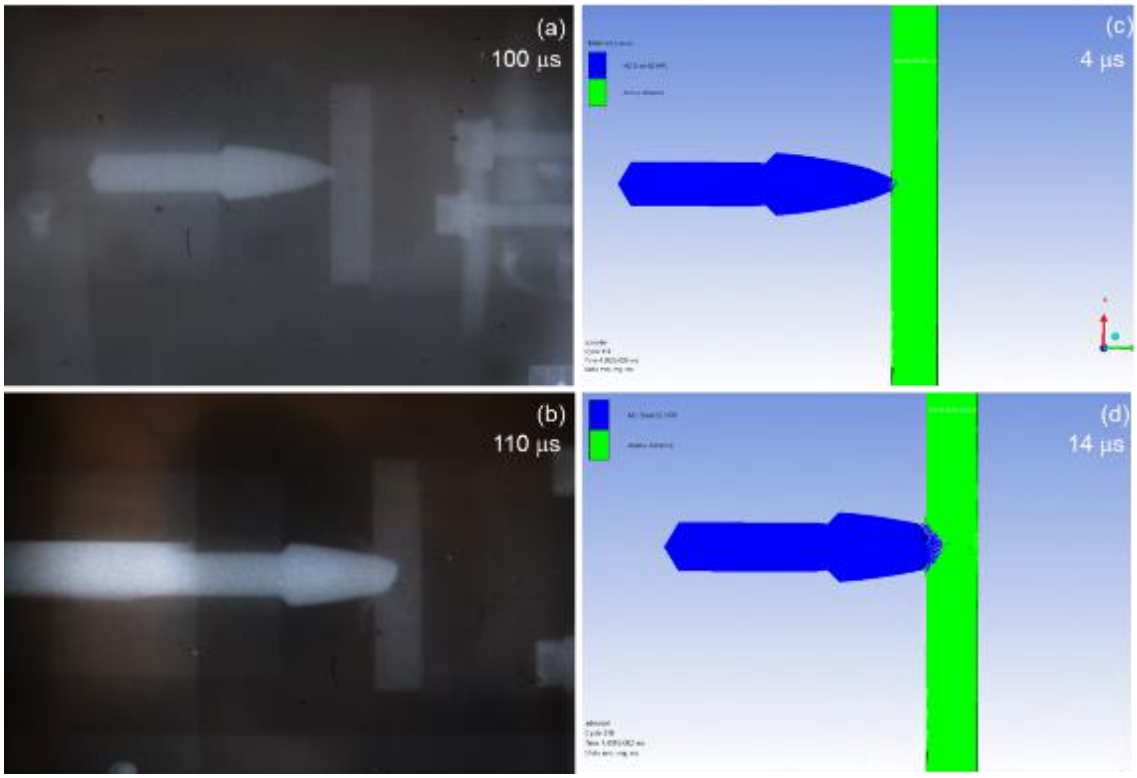

Figure 5.33 Un-jacketed steel core penetration into 9-mm Armox plate; (a) and (b) X-ray images; (c) and (d) numerical simulation results.

Figure 5.34 shows a penetration event where a copper jacket is included. Both captured flash X-rays and corresponding simulations both show the jacket clearly deforming during the impact event. During the penetration, the front part of the copper jacket was deformed while simultaneously confining the core to retain the eroded projectile material in-situ. This confining process allow projectile to retain its mass inertia to give more impact energy. The copper jacket deformation in experimental work can be observed in Figures 5.34 (a) and (b), highlighted via red arrows. The same behaviour also occurred in the numerical simulations, with the copper jacket flowing as the steel core was confined (see the yellow arrows in Figures 5.34 (c) and (d).

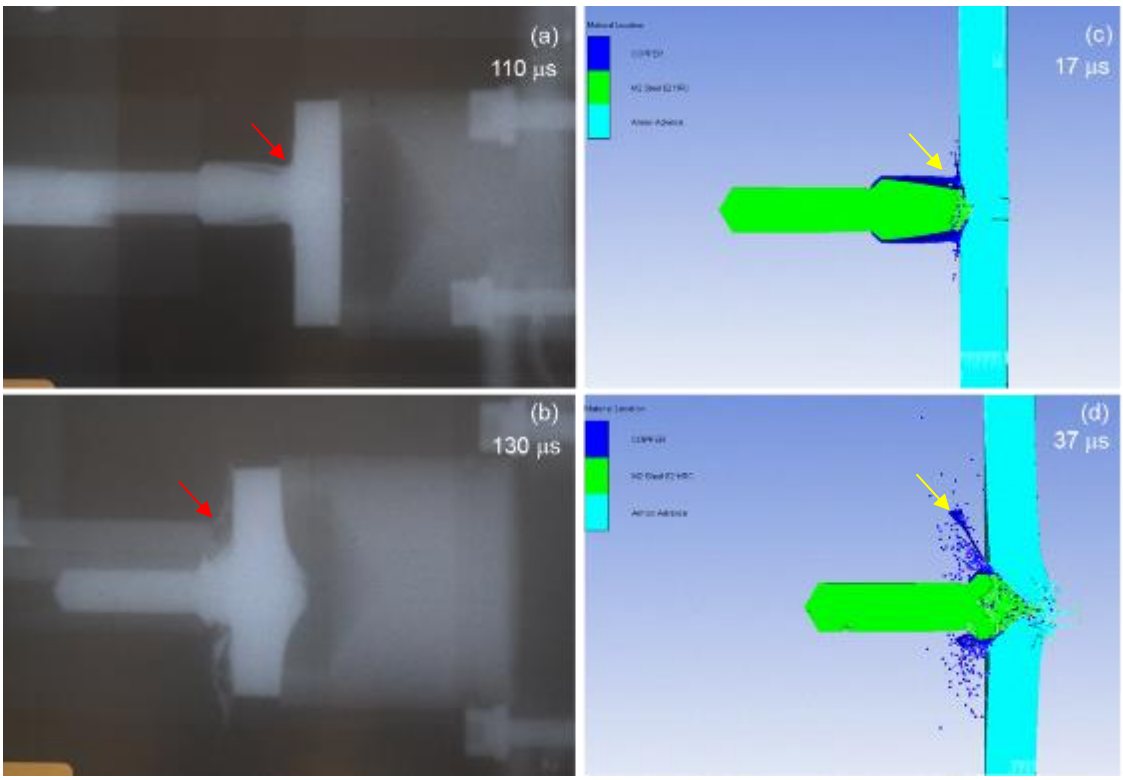

Figure 5.34 Jacketed steel core penetration into 9-mm Armox plate; (a) and (b) X-ray images; (c) and (d) numerical simulation results.

In addition to direct comparisons of failure geometries / architectures, average fragment velocity and spray angle can also be measured in both experimental and numerical simulation work. In the experimental results, fragment velocities were measured using the PCC 2.7 (Phantom high-speed camera) software for forward ballistic experiments. While in the corresponding numerical simulations, velocities were measured by using velocity contour range. Table 5.6 shows the effect of including a copper jacket in terms of fragment (residual) velocity after perforation for both an experimental shot and a corresponding numerical simulation. The average fragment velocities of the un-jacketed projectiles are 457 m/s for experimental result and 446 m/s for the simulation result; these are in-turn lower than the average velocities for the jacketed case of 571 (experimental) and 568 m/s (simulation). As explained above, the copper jacket confining the

steel core – as well as acting to prevent its premature disruption via a cushioning effect – resulted in a higher penetration energy and thus more efficient penetration. Fragments spray angle was also measured from fragments, which are indicated using a red arrow in Figures 5.35 and 5.36, as well as eroded material dispersion behind the target plate. The fragments spray angle of experimental and simulation results were measured in Solidworks software. An angle of two lines representing the eroded material dispersion was measured as fragment spray angle. The copper jacket deformation allowed the projectile to damage a wider target surface, so it produced a wider fragments spray angle. The fragments spray angle of the un-jacketed projectile for both experimental and numerical simulation were 51.68^{o} and 51.50^{o}. On the other hand, higher fragments spray angle were observed in experimental and numerical simulation results for the jacketed projectile at 72.95^{o} and 69.88^{o} respectively. Generally, the higher is the spray angle, the higher is probability of fragment to hit other targets behind the initial target.

Table 5.8 Fragments velocity and spray angle of projectile after perforation.

Result of	**Jacket presence**	**Initial projectile velocity (m/s)**	**Avg. fragments Velocity (m/s)**	**Fragments spray angle (^{o})**
Experimental	No	788	457	51.68
Simulation	No	750	446	51.50
Experimental	Yes	759	571	72.95
Simulation	Yes	750	568	69.88

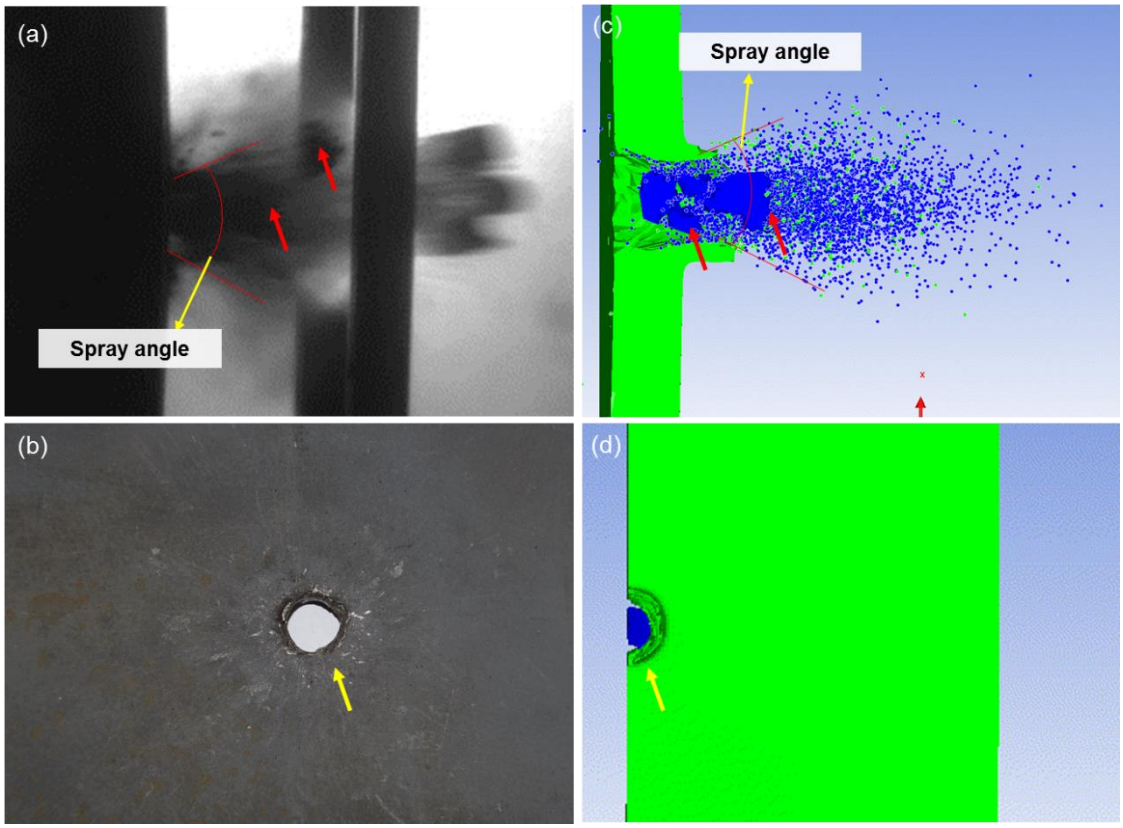

Figure 5.35 Unjacketed projectile and target damage after perforation (a) and (b) experimental work; (c) and (d) numerical simulation.

An important result was found from the perforation of high hardness Armox Advance armour plate. The jacketed projectile was observed to shatter the 9 mm target plate creating a large hole at the penetration point (see Figure 5.36 (b)). This event was also indicated by the simulation result as shown in Figure 5.36 (d). In addition, the cracking behaviour apparent on the experimentally impacted plate was also captured during the simulated penetration and, importantly, was not found in the un-jacketed perforation where a plugging mechanism appeared to dominate.

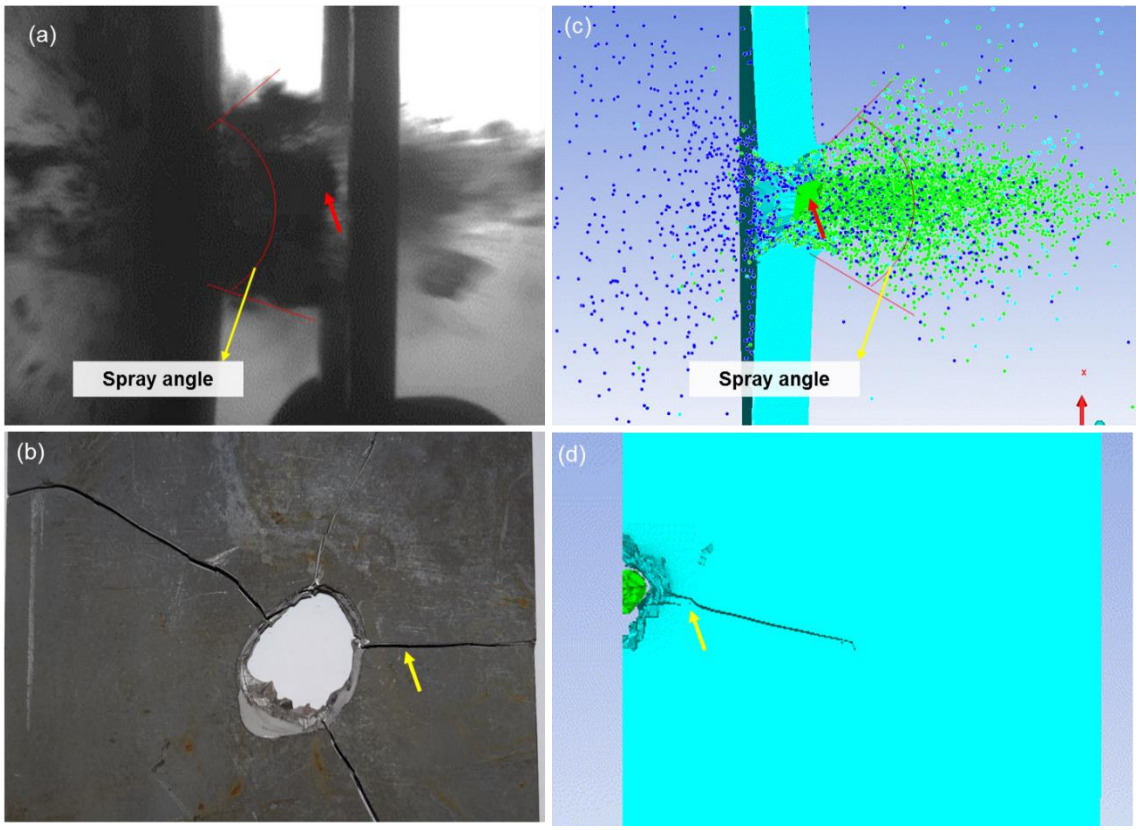

Figure 5.36 Jacketed projectile and target damage after perforation (a) and (b) experimental work; (c) and (d) numerical simulation.

Overall, the simulations agreed well with the corresponding experimental results with excellent agreement in terms of both (residual) fragment velocity, fragment dispersion angle and even failure mode. This gives enhanced confidence in the mechanisms put forwards to explain the importance of the jacket in penetration. Further, analysis of pressure dispersion within projectiles and target plates during impact provides an additional insight in this study. The pressure dispersion explains the initial damage caused by copper jacket as well as the projectile spall failure as a result of reflected waves collision.

6 Conclusions

The core aim of this study was to further investigate the theory and mechanisms underpinning the influence of a copper jacket in the subsequent penetration against a high hardness armour steel (in this case Armox Advance). In addition, the project was designed to investigate the influence of factors such as projectile geometry and hardness. Experiments were conducted using a 12.7 mm armour piercing projectile. Both the steel core design and copper jacket had a relatively unique and complex geometry when compared to other systems reported in recent studies. This design was originally produced to increase the mass of the steel core as well as the associated penetration performance. The projectiles were prepared both with and without a crimped copper jacket. Both forward and reverse ballistic experiments were undertaken to investigate projectile performance by measuring residual velocity and capturing X-Ray images showing details of the penetration events. Further, a pressure gauge experiment was also undertaken with the aim of highlighting the influence of pressure generated by the jacketed and the un-jacketed projectiles upon impact. Overall, these experiments were designed to provide complementary data to aid in the aims of the project. To support these studies ANSYS Autodyn® numerical simulations were also employed to complement the main experiments.

Overall, this research has been successful – with experimental and numerical simulation validating the performance of jacketed and unjacketed rounds. The experiments also provided significant insight into the mechanisms (via X-Ray images and complementary numerical simulations) governing projectile penetration. Practically, increasing the hardness condition of the steel cores enhanced the penetration performance of the projectiles. From the experimental and simulation results, a number of conclusions can be drawn, namely:

- Increasing steel core hardness extend the penetration performance. A linear increment of residual velocity was observed in forward ballistic tests as well as in terms of the length of recovered cores (with larger recovered lengths corresponding to enhanced penetration). However,

further hardness increase to 62 led the projectile to shatter because of the corresponding ductility decrease / enhanced loading on impact.

- A clear link between target thickness and performance for Armox advance plates was observed. In the 5-mm thick target plates, for penetration by both the jacketed and the un-jacketed projectiles, an increase in projectile hardness and / or the presence of the copper jacket had minimal effect for hardness values of 42 and 52 HRC. Whilst, in the 62 HRC projectile experiments, a relatively small difference in performance was observed.
- For thicker, 9-mm target penetration experiments, when the projectiles hardness was higher than the target hardness, the presence of copper jacket on projectiles caused extra damage to the target. However, when the target was harder than the projectiles, the un-jacketed projectiles at a lower hardness were observed to be more penetrative compared with the jacketed cores.
- This result, namely enhanced effect of a jacket as well as core hardness for thicker plates, suggests that confinement of the core is also important. Essentially, with thicker plates the core interacts with the plate for longer during penetration that will increase core confinement time. Pressure gauge experiments strengthened the main experiment results. From these experiments, it was apparent that the jacketed projectiles generated a higher pressure in the target than the un-jacketed projectiles.
- In numerical simulations, a mesh size of 0.7 mm gave a very good match to experimental results. Importantly, the simulation images showed a penetration mechanism which was in good agreement with forward and reverse ballistic results.
- It is clear from the observations detailed in this thesis that the copper jacket plays an important role in the penetration of Armox Advance targets. The copper jacket appears to pre-damage the target and, protects / cushions the cores from direct contact with the target surface.

- The protective role played by the jacket was observed to have two key components; a cushioning effect on impact (reducing core loading) and a confinement effect.

In line with the points outlined above, in this project the influence of both the presence of a jacket and core hardness on 12.7 mm armour piercing projectile performance have been assessed. It is clear that harder projectiles are more efficient; however, this needs to be coupled with the presence of a ductile jacket to cushion and confine the core if penetration is to be optimised. For the experiments undertaken here, this meant that the jacketed 62 HRC projectiles were the most efficient in terms of ability to penetrate the target. Further, basic Autodyn® numerical simulations appear to hold significant promise in validation of projectile behaviour (e.g. in-line with the agreement between experiment and simulation here).

7 Recommendation for further work

While this study has been very successful in its core aim of enhancing understanding of the penetration mechanisms underpinning jacketed bullet behaviour, there are a number of areas where additional time and resources would allow for potentially worthwhile expansion of this work. Investigation of these areas would help to enhance knowledge and the development of the mechanisms underpinning both projectile penetration and protection against the same.

- Evaluation of un-jacketed and jacketed projectiles performance using V50 ballistic test.
- Investigation of copper or other ductile material jacketing on a long rod penetrator (APFSDS) to enhance the penetration performance.
- Investigation understand the effect of lead filler on ammunition performance
- An investigation to evaluate the use of composite armour systems that comprises steel plate as the main armour and other backing or cover plates against the jacketed and unjacketed hard core round

REFERENCES

1. Walker RE. Cartridges and firearm identification. Boca Raton: CRC Press; 2013.
2. Carlucci DE., Jacobson SS. BALLISTICS: Theory and design of guns and ammunition. 2nd editio. New York: CRC Press; 2008.
3. Hazell PJ. Armour: materials, theory, and design. Boca Raton: CRC Press; 2016.
4. Hazell PJ., Appleby-Thomas GJ., Philbey D., Tolman W. The effect of gilding jacket material on the penetration mechanics of a 7.62 mm armour-piercing projectile. International Journal of Impact Engineering. Elsevier Ltd; 2013; 54: 11–18. Available at: DOI:10.1016/j.ijimpeng.2012.10.013.
5. Roberts A. Optimisation of small arms defeat via dynamic jacket removal. MSc by Research thesis. Cranfield University; 2016.
6. Kiliç N., Ekici B. Ballistic resistance of high hardness armor steels against 7.62 mm armor piercing ammunition. Materials and Design. 2013; 44: 35–48. Available at: DOI:10.1016/j.matdes.2012.07.045.
7. Ryan S., Li H., Edgerton M., Gallardy D., Cimpoeru SJ. The ballistic performance of an ultra-high hardness armour steel: An experimental investigation. International Journal of Impact Engineering. 2016; 94: 60–73. Available at: DOI:10.1016/j.ijimpeng.2016.03.011.
8. Savio SG., Madhu V. Effect of Tile Thickness and Projectile Velocity on the Ballistic Performance of Boron Carbide Against 12.7 mm AP. Procedia Engineering. 2017; 173: 286–292. Available at: DOI:10.1016/j.proeng.2016.12.015.
9. PT Pindad (Persero) website. 2017. Available at: https://www.pindad.com/special-vehicles (Accessed: 3 December 2017).
10. Crouch IG. (ed.), The Science of Armour Materials. Oxford: Elsevier; 2017.
11. Defence Procurement Agency. Ministry of Defence DEF STAN 95-24/3. Armour Plate, Steel (3-160 mm). Glasgow: Defence Procurement Agency, Directorate of Standardization; 2004.

12. Showalter DD, Gooch AW, Burkins MS, Montgomery JS, Squillacioti RJ. Development and ballistic testing of a new class of high hardness steel armour. AMMTIAC Quarterly Journal. 2010; 4(4): 3-6.
13. Kiliç N., Bedir S., Erdik A., Ekici B., Taşdemirci A., Güden M. Ballistic behavior of high hardness perforated armor plates against 7.62mm armor piercing projectile. Materials and Design. 2014; 63: 427–438. Available at: DOI:10.1016/j.matdes.2014.06.030.
14. Fras T., Murzyn A., Pawlowski P. Defeat mechanisms provided by slotted add-on bainitic plates against small-calibre 7.62 mm ?? 51 AP projectiles. International Journal of Impact Engineering. Elsevier Ltd; 2017; 103: 241–253. Available at: DOI:10.1016/j.ijimpeng.2017.01.015.
15. Jena PK., Savio SG., Kumar KS., Madhu V., Mandal RK., Singh AK. An Experimental Study on the Deformation Behavior of Aluminium Armour Plates Impacted by Two Different Non-deformable Projectiles. Procedia Engineering. Elsevier B.V.; 2017; 173: 222–229. Available at: DOI:10.1016/j.proeng.2016.12.001.
16. Rahman NA., Abdullah S., Zamri WFH., Abdullah MF., Omar MZ., Sajuri Z. Ballistic limit of high-strength steel and Al7075-T6 multi-layered plates under 7.62-mm armour piercing projectile impact. Latin American Journal of Solids and Structures. 2016; 13(9): 1658–1676. Available at: DOI:10.1590/1679-78252657.
17. Manes A., Serpellini F., Pagani M., Saponara M., Giglio M. Perforation and penetration of aluminium target plates by armour piercing bullets. International Journal of Impact Engineering. Elsevier Ltd; 2014; 69: 39–54. Available at: DOI:10.1016/j.ijimpeng.2014.02.010.
18. Hazell PJ., Appleby-Thomas GJ., Wielewski E., Stennett C., Siviour C. The influence of microstructure on the shock and spall behaviour of the magnesium alloy, Elektron 675. Acta Materialia. 2012; 60(17): 6042–6050. Available at: DOI:10.1016/j.actamat.2012.07.041.
19. Sukumar G., Bhav Singh B., Bhattacharjee A., Siva Kumar K., Gogia AK. Ballistic impact behaviour of β-CEZ Ti alloy against 7.62 mm armour

piercing projectiles. International Journal of Impact Engineering. 2013; 54: 149–160. Available at: DOI:10.1016/j.ijimpeng.2012.11.002

20. Diederen a M., Broos JPF., Trigt SN Van. Ballistic Protection Against Armour Piercing Projectiles Using Titanium Base Armour. Cost Effective Application of Titanium Alloys in Military Platforms. 2001; 99(May): 7–11.
21. Horsfall I., Ehsan N., Bishop W. A Comparison of the Performance of Various Light Armour Piercing Ammunition. Journal of Battlefield Technology. 2000; 3(3): 5–9.
22. Pettersson A., Magnusson P., Lundberg P., Nygren M. Titanium-titanium diboride composites as part of a gradient armour material. International Journal of Impact Engineering. 2006; 32(1–4): 387–399. Available at: DOI:10.1016/j.ijimpeng.2005.04.003.
23. Appleby-thomas AG., Hameed A., Wood D., Rowley J., Jaansalu K. On the ballistic response of rapidly-prototyped alumina. 2016; Uploaded paper at: http://www.ballistics.org.
24. Crouch IG., Appleby-Thomas G., Hazell PJ. A study of the penetration behaviour of mild-steel-cored ammunition against boron carbide ceramic armours. International Journal of Impact Engineering. Elsevier Ltd; 2015; 80: 203–211. Available at: DOI:10.1016/j.ijimpeng.2015.03.002.
25. Mines RAW. A one-dimensional stress wave analysis of a lightweight composite armour. Composite Structures. 2004; 64(1): 55–62. Available at: DOI:10.1016/S0263-8223(03)00213-7
26. Akella K., Naik NK. Composite armour - A review. Journal of the Indian Institute of Science. 2015. pp. 297–312.
27. Grujicic M., Bell WC., Biggers SB., Koudela KL., Tarter JF., Cheeseman BA. The effect of a carbon-nanotube forest-mat strike face on the ballistic-protection performance of E-glass reinforced poly-vinyl-ester-epoxy composite armour. Proceedings of the Institution of Mechanical Engineers, Part L: Journal of Materials: Design and Applications. 2008. pp. 15–27. Available at: DOI:10.1243/14644207JMDA136.

28. Medvedovski E. Lightweight ceramic composite armour system. Advances in Applied Ceramics. 2006; 105(5): 241–245. Available at: DOI:10.1179/174367606X113537.
29. Deniz T. Ballistic penetration of hardened steel plates. MSc thesis. Middle Easy Technical University. 2010. Available at: http://citeseerx.ist.psu.edu/viewdoc/download?doi=10.1.1.633.393&rep=rep1&type=pdf (Accessed: 28 December 2017).
30. Tarantola A. How Armor Is Evolving to Beat Tank-Smashing RPGs. Gizmodo. 4 August 2014. Available at: https://gizmodo.com/how-armor-is-evolving-to-beat-tank-smashing-rpgs-1555422743 (Accessed: 8 January 2018).
31. Defense World. Israeli Rafael Offers Trophy Countermeasures, Spike Missiles to Australia. 2017. Available at: http://www.defenseworld.net/news/21190/Israeli_Rafael_Offers_Trophy_Countermeasures__Spike_Missiles_to_Australia#.WpgnXWrFKpo (Accessed: 1 March 2018)
32. Mayseless M. Effectiveness of Explosive Reactive Armor. Journal of Applied Mechanics. 2011; 78(5): 51006. Available at: DOI:10.1115/1.4004398.
33. Below The Turret Ring. Puma IFV armor and upgrade speculations. 2016. Available at: https://below-the-turret-ring.blogspot.co.uk/2016/10/puma-ifv-armor-and-upgrade-speculations.html (Accessed: 8 January 2018).
34. Shvetsov GA., Matrosov AD., Stankevich S V. Effect of electric current on shaped-charge operation. IEEE Transactions on Plasma Science. 2015; 43(5): 1167–1172. Available at: DOI:10.1109/TPS.2015.2406335.
35. Plyashkevich LN., Shuvalov AM., Spirov GM., Brodskii AY., Dimant EM., Luk'yanov NB., et al. Disruption of shaped-charge jets by a current. Combustion, Explosion and Shock Waves. 2002; 38(5): 602–605. Available at: DOI:10.1023/A:1020355021586.
36. Appelgren P., Larsson A., Lundberg P., Skoglund M., Westerling L. Studies of electrically-exploded conductors for electric armour

applications. Acta Physica Polonica A. 2009. pp. 1072–1074. Available at: DOI:10.12693/APhysPolA.115.1072

37. John V. Introduction to Engineering Material. 4th edn. New York: Palgrave Macmillan; 2003.
38. Ashby MF, Jones DRH. Engineering Material 1: an introduction to properties, applications, and design. 4th edn. Oxford: Elsevier; 2012.
39. Kelly PA. Kelly's online books. Department of Engineering Science, University of Auckland. Available at: http://homepages.engineering.auckland.ac.nz/~pkel015/SolidMechanics Books/Part_II/index.html (Accessed: 29 March 2017).
40. Ritchie RO. The conflicts between strength and toughness. Nature Material. 2011; 10: 817-822. Available at: DOI: 10.1038/NMAT3115.
41. Callister WD,Jr. Materials science and engineering: an introduction. Utah: John Wiley and Sons, Inc. 2003.
42. Ashby M. 2 material and process selection charts. Cambridge University. Available at: http://www.grantadesign.com/download/pdf/teaching_resource_books/2-Materials-Charts-2010.pdf (Accessed: 18 April 2017).
43. Ramesh KT. 33. High strain rate and impact experiments. In Sharpe Jr. WN (ed.). Springer Handbook of Experimental Solid Mechanics. Springer; 2008.
44. Zukas, JA. (ed.) Introduction to Hydrocodes. Baltimore: Elsevier Science. 2004.
45. Murr LE. Chapter 1: Metallurgical effects of shock and high-strain-rate loading. In Blazynski TZ (ed.). Materials at high strain rates. London; Elsevier Applied Science; 1987.
46. Harding J. Chapter 4: The effect of high strain rate on material properties . In Blazynski TZ (ed.). Materials at high strain rates. London; Elsevier Applied Science; 1987.
47. Ashby MF, Jones DRH. Engineering Material 2: an introduction to microstructures, processing and design. 3rd edn. Oxford: Elsevier; 2006.

48. Johnson GR., Cook WH. Lagrangian epic code computations for oblique, yawned-rod impacts onto thin-plate and spaced-plate targets at various velocities. International Journal of Impact Engineering. 1993; 14: 373–383.
49. Iqbal MA., Chakrabarti A., Beniwal S., Gupta NK. 3D numerical simulations of sharp nosed projectile impact on ductile targets. International Journal of Impact Engineering. Elsevier Ltd; 2010; 37(2): 185–195. Available at: DOI:10.1016/j.ijimpeng.2009.09.008
50. Iqbal MA., Senthil K., Sharma P., Gupta NK. An investigation of the constitutive behavior of Armox 500T steel and armor piercing incendiary projectile material. International Journal of Impact Engineering. Elsevier Ltd; 2016; 96: 146–164. Available at: DOI:10.1016/j.ijimpeng.2016.05.017
51. O'Daniel JL., Koudela KL., Krauthammer T. Numerical simulation and validation of distributed impact events. International Journal of Impact Engineering. 2005; 31(8): 1013–1038. Available at: DOI:10.1016/j.ijimpeng.2004.06.002
52. Tria DE., Trębiński R. Methodology for experimental verification of steel armour impact modelling. International Journal of Impact Engineering. 2017; 100: 102–116. Available at: DOI:10.1016/j.ijimpeng.2016.10.011
53. Hu F., Wu H., Fang Q., Liu JC., Liang B., Kong XZ. Impact performance of explosively formed projectile (EFP) into concrete targets. International Journal of Impact Engineering. 2017; 109: 150–166. Available at: DOI:10.1016/j.ijimpeng.2017.06.010
54. Elnasri I., Zhao H. Impact perforation of sandwich panels with aluminum foam core: A numerical and analytical study. International Journal of Impact Engineering. Elsevier Ltd; 2016; 96: 50–60. Available at: DOI:10.1016/j.ijimpeng.2016.05.013.
55. Barret S., Christiansen RVLR., Othman A. Ballistic properties of projectile material. Student group report. Aalborg University. 2016. Available at: http://projekter.aau.dk/projekter/files/249530927/DMS3_2225a.pdf (Accessed: 31 December 2017).
56. eCourses. OU Engineering Media Lab. Workbench User's Guide . 2018. Available at:

http://ecourses.ou.edu/fem/manuals/Workbench_Users_Guide.pdf (Accessed: 28 January 2018).

57. Meyers MA. Dynamic behaviour of materials. New York: John Wiley and Sons, Inc.; 1994.
58. OTAI Special Steel. EN8 Carbon Steel, 080M40 BS 970 Specification. Available at http://www.astmsteel.com/product/en8-carbon-steel-080m40-bs-970/ (Accessed: 15 September 2017).
59. Bohler Uddeholm. Bohler-Uddeholm M2 (high speed steel for cold work applications). Available at: www.bucorp.com/media/M2_data_sheet_09032013.pdf (Accessed: 18 April 2017).
60. Smith Metal. C101 Technical Data Sheet, Copper. Available at https://www.smithmetal.com/pdf/copper-brass-bronze/copper/c101.pdf (Accessed: 11 October 2017).
61. Bourne NK. A 50 mm bore gas gun for dynamic. Measurement Science and Technology. 2003; 14 (3): 273–27. Available at: DOI:10.1088/0957-0233/14/3/304.
62. Wielewski E., Appleby-Thomas GJ., Hazell PJ., Hameed A. An experimental investigation into the micro-mechanics of spall initiation and propagation in Ti-6Al-4V during shock loading. Materials Science and Engineering A. 2013; 578: 331–339. Available at: DOI:10.1016/j.msea.2013.04.055
63. Appleby-Thomas GJ., Hazell PJ. A study on the strength of an armour-grade aluminum under high strain-rate loading. Journal of Applied Physics. 2010; 107(12). Available at: DOI:10.1063/1.3431346.
64. Appleby-Thomas GJ., Wood DC., Hameed A., Painter J., Le-Seelleur V., Fitzmaurice BC. Investigation of the high-strain rate (shock and ballistic) response of the elastomeric tissue simulant Perma-Gel® International Journal of Impact Engineering. Elsevier Ltd; 2016; 94: 74–82. Available at: DOI:10.1016/j.ijimpeng.2016.04.003.

65. Rosenberg Z., Yaziv D., Partom Y. Calibration of foil-like manganin gauges in planar shock wave experiments. Journal of Applied Physics. 1980; 51(7): 3702–3705. Available at: DOI:10.1063/1.328155
66. Proteq. Determination of Poisson's Ration and the Modulus of Elasticity by measuring with P- and S-wave transducers. 2017. Available at https://www.proceq.com/uploads/tx_proceqproductcms/import_data/files/Determining%20Poissons%20ratio%20and%20Elastic%20modulus.pdf (Accessed: 19 October 2017).
67. Ozen M. Meshing workshop [PowerPoint presentation]. Ozen Engineerin, Inc. 2014. Available at: https://www.ozeninc.com/wp-content/uploads/2014/11/MESHING_WORKSHOP_2014.pdf (Accessed: 28 December 2017).
68. Madej M. 2012. Tungsten Carbide as an Addition to High Speed Steel Based Composites. In: Liu K (ed.) Tungsten Carbide - Processing and Applications. InTech. 2012. pp. 57-80. Availabe at: https://cdn.intechopen.com/pdfs-wm/41529.pdf (Accessed: 24 January 2018).
69. SSAB. Armox Advance. Available at: http://www.ssab.co.uk/products/brands/armox/armox-advance (Accessed: 11 May 2017).
70. Brown LB., Hazell PJ., Crouch IG., Escobedo JP., Brown AD. Computational and Split-Hopkinson Pressure-Bar studies on the effect of the jacket during penetration of an AK47 bullet into ceramic armour. Materials and Design. Elsevier Ltd; 2017; 119: 47–53. Available at: DOI:10.1016/j.matdes.2017.01.062

APPENDICES

Appendix A

A.1 Ethics

Lesmana, Denny

From: donotreply@infonetica.net
Sent: 04 May 2017 10:58
To: Lesmana, Denny
Cc: Hameed, Amer
Subject: CURES Submission: Approved

Dear Denny

Reference: CURES/2595/2017
Title: An investigation into the effect of the gilding jacket on 12.7 mm armour-piercing projectile penetration of armour materials

Thank you for your application to the Cranfield University Research Ethics System (CURES).

Your proposed research activity has been confirmed as Level 1 risk in terms of research ethics. You may now proceed with the research activities you have sought approval for.

Please remember that CURES occasionally conducts audits of projects. We may therefore contact you during or following execution of your fieldwork. Guidance on good practice is available on the research ethics intranet pages.

If you have any queries, please contact cures-support@cranfield.ac.uk

We wish you every success with your project.

Regards

CURES Team

May we remind you of the importance of addressing health and safety issues in your research. Templates and further guidance are available here.

A.2 Risk Assessment

Risk Assessment Form
CU-SHE-FORM-3.01
V3.0

Risk Assessment Number:		Task/Activity assessed:	Research work in Building 18				
Name/job role of people consulted during assessment:		Denny Lesmana – Research Student		Date of Assessment:	May 2017	Review Date:[4]	May 2018

Acknowledgements, Sign off and Authorisation

	Acknowledgement	Name	Signature	Date
Risk Assessor:	By signing this risk assessment I acknowledge my responsibility as the Risk Assessor for conducting this risk assessment in accordance with CU-HAS-PROC-3.01, Risk Assessment Procedure.	Dr David Wood	David	25/5/17
Checked by: (where required)	By signing this risk assessment I acknowledge my responsibility as the checker for this risk assessment in accordance with CU-HAS-PROC-3.01, Risk Assessment Procedure.	Dr Gareth Appleby-Thomas	GAT	25/5/17
Authorising Person:	By signing the risk assessment, I acknowledge my responsibility as the Line manager/Supervisor for reviewing and approving this risk assessment and communicating controls and any additional controls to staff/students (as appropriate).	Prof. Amer Hameed	Amer Hameed	25.May.17

	Tasks/Operational steps/Sub tasks/Events:	Significant hazards – • What could happen and why?	Who is affected and how – • Who might be hurt? • How bad could it reasonably be?	What are your existing controls? (Reference all Safe Systems Of Work (SSOW), Standard Operating Procedures (SOP) and Emergency Procedures)	Existing Risk Rating (Consequence x Likelihood = Total) C	L	TOTAL	Are additional controls needed? Y/N (If Yes, RAMP required)
1	Work in Laboratory (target preparation)	Risk of Harm	Staff and student in Building 18	Following instructions of accompanying SOP, training and, good housekeeping.	3	1	3	N
2	Use gas gun for experiments	Gas gun damaged and experiment cannot be done. Risk of Harm	Staff and student in Building 18	Always cleaning, checking and doing maintenance after using the gas gun. Following instructions of accompanying SOP, training and, good housekeeping.	5	1	5	N

3	Travel to and from sites	Road accident	Student	Use licensed and reliable public transport, private car or a reputable taxi firm. Plan the route in advance and always take a map. Ensure appropriate budgeting for use of taxis if needed. Study a map of the area for clues as to its character. Look for schools, post offices, railway stations and other hubs of activity. Think about escape routes from dense housing areas. Avoid walking alone at night. Don't use personal stereos so that it can hamper sound happening around.	5	1	5	N
4	Use special design projectile for experiment	University is not able to provide it	Student	Provide the projectile's drawing details and give them to workshops for production process. Contact PT.Pindad (Persero) to send some projectiles.	2	3	6	N
5	Use Tungsten Carbide-Cobalt material for projectile	Workshops is not able to produce that material in projectile shape	Student	Provide tungsten carbide-cobalt raw material in annealed rod (less hardness) Or, order the material in projectile shape to special metal manufacturer.	2	3	6	N
6	Use Armox-550 as target material	University is not able to provide it	Student	Use other armour plate which has a similar properties, such as Armox Advance, Armox-500, Armox-600 and Compass B555	2	3	6	N
6	Analyse experiment data and write a thesis	corrupt or deleted data caused by virus or damaged hardware	Student	Back all of data periodically to other hard-disk as spare. Update computer's operation system and anti-virus software periodically.	3	1	3	N

Emergency Planning Arrangements relating to operations/event[16]

Risk Rating Matrix

RISK MATRIX					
Consequence **Likelihood**	Negligible (1)	Minor (2)	Medium (3)	Major (4)	Severe (5)
Almost Certain (5)	5	10	15	20	25
Likely (4)	4	8	12	16	20
Possible (3)	3	6	9	12	15
Unlikely (2)	2	4	6	8	10
Very Unlikely (1)	1	2	3	4	5

Rating	Interpretation	Authorisation
≤ 6 = Low Risk	Acceptable but ensure that controls are maintained	Line Manager or equivalent
9 -12 = Medium Risk	Adequate but look to improve if reasonably practicable	Line Manager or equivalent
15 – 25 = Unacceptable Risk	STOP activity and make immediate improvements	PVC School/Director of PSU

CONSEQUENCE (considered WITH controls in place)		
5	Severe	• Fatality (ies) • Severe or chronic illnesses or permanent life changing impact
4	Major	• Injury such as fracture of bones, dislocation, or acute ill health e.g. occupational asthma, occupational dermatitis
3	Medium	• An injury that requires first aid treatment and subsequent treatment by health care professional • No lost time illnesses and no chronic/acute health effects
2	Minor	• An injury that requires basic first aid treatment such as administering a plaster, individual able to continue at work e.g. minor cuts, bruising, abrasions, strains or sprains
1	Negligible	• Superficial or no physical injury or health effects

LIKELIHOOD (considered WITH controls in place)		
5	Almost Certain	• Will occur/greater than a likelihood of 1 in 1(yr)
4	Likely	• Known to occur/probably occurs most circumstances/No greater than a likelihood of 1 in every 10
3	Possible	• Might occur /no greater than a likelihood of 1 in 1000
2	Unlikely	• Not likely/could occur at some time/no greater than a likelihood of 1 in 10,000
1	Very Unlikely	• May only occur in exceptional circumstances/no greater than a likelihood of 1 in 100,000

A.3 Project Plan

For reference, the key stages of the project plan adopted are highlighted below.

No	Activities	2016										2017		
		3	4	5	6	7	8	9	10	11	12	1	2	3
1	Literature review													
2	Material characterisation													
	Sample preparation (workshops)													
	Sample heat treatment													
3	Design overview													
4	Test and modelling													
	Forward-ballistic experiment													
	Reverse-ballistic experiment													
	Final ballistic test													
5	Results analysis and paper writing													

A.4 Initial velocity of forward ballistic experiments

M2 steel Core Hardness (HRC)	Initial velocity (m/s)			
	Unjacketed projectile		Jacketed Projectile	
	Armox 5 mm	Armox 9 mm	Armox 5 mm	Armox 9 mm
42	761	773	762	762
	773	759	769	767
52	756	794	777	786
	777	782	757	761
62	773	753	744	741
	755	754	745	766
		766		741